

# FABRICATION AND TRIBOLOGY OF FRICTION STIR PROCESSED Al ALLOY SURFACE COMPOSITES

Ph.D. THESIS

*by*

VIPIN SHARMA



DEPARTMENT OF METALLURGICAL AND MATERIALS ENGINEERING  
INDIAN INSTITUTE OF TECHNOLOGY ROORKEE  
ROORKEE – 247667, INDIA  
JULY, 2015

# **FABRICATION AND TRIBOLOGY OF FRICTION STIR PROCESSED Al ALLOY SURFACE COMPOSITES**

**A THESIS**

*Submitted in partial fulfilment of the  
requirements for the award of the degree*

*of*

**DOCTOR OF PHILOSOPHY**

*in*

**METALLURGICAL AND MATERIALS ENGINEERING**

*by*

**VIPIN SHARMA**



**DEPARTMENT OF METALLURGICAL AND MATERIALS ENGINEERING  
INDIAN INSTITUTE OF TECHNOLOGY ROORKEE  
ROORKEE – 247667, INDIA  
JULY, 2015**

**©INDIAN INSTITUTE OF TECHNOLOGY ROORKEE, ROORKEE- 2015  
ALL RIGHTS RESERVED**



# INDIAN INSTITUTE OF TECHNOLOGY ROORKEE ROORKEE

## CANDIDATE'S DECLARATION

I hereby certify that the work which is being presented in the thesis, entitled “**Fabrication and Tribology of Friction Stir Processed Al Alloy Surface Composites**” in partial fulfilment of the requirements for the award of the degree of Doctor of Philosophy and submitted in the Department of Metallurgical and Materials Engineering, Indian Institute of Technology Roorkee, Roorkee is an authentic record of my own work carried out during the period from July, 2011 to July, 2015 under the supervision of **Dr. Ujjwal Prakash**, Associate Professor and **Dr. B.V. Manoj Kumar**, Assistant Professor, Department of Metallurgical and Materials Engineering, Indian Institute of Technology Roorkee, Roorkee.

The matter presented in this thesis has not been submitted by me for the award of any other degree of this or any other institute.

(VIPIN SHARMA)

This is to certify that the above statement made by the candidate is correct to the best of our knowledge.

(Ujjwal Prakash)  
Supervisor

(B.V. Manoj Kumar)  
Supervisor

Date:

Friction stir processing (FSP) is recently identified as a potential technique in fabrication of surface composites. It needs to be recognized that microstructural characteristics and mechanical behavior of aluminum alloy bulk composites prepared by conventional technique are well reported, whereas systematic study on the effect of FSP parameters on microstructure and tribological performance of surface composites of aluminium alloys is not available. In the present work, surface composites of SiC, TiC, Al<sub>2</sub>O<sub>3</sub>, graphite or Sn particles reinforced AA2014, LM24 or AA5083 alloys were fabricated by FSP. The influence of FSP parameters was studied on microstructure, hardness and tensile behavior of surface composites. The tribological performance of the FSPed surface composites against steel ball was studied using a ball-on-disc tribometer in unlubricated sliding conditions.

First, the effect of multi-pass on microstructure and mechanical characteristics of AA2014 alloy was studied. Further, critical analysis of the addition of SiC or TiC particles in multi-pass FSPed AA2014 surface was done to study the influence on microstructure and mechanical behavior. In the second set of experiments, processing strategies like multi-pass, change in rotational speed or traverse speed, tool offset and dual tool probe were examined in fabricating defect free SiC/AA5083 surface composites with uniform distribution of reinforcement particles. The microstructure, hardness and tensile behavior were related for the surface composites prepared with each strategy. The influence of the addition of low melting point metal tin in graphite/LM24 alloy surface composite was investigated in third set of experiments. The heat input conditions in FSP were changed by manipulating rotational speed. The synergetic effect of rotational speed, tin addition and sliding load on the friction and wear characteristics of graphite/LM24 alloy surface composites was investigated. In the last set, the tribological performance of FSPed Al<sub>2</sub>O<sub>3</sub>/AA5083 surface composites was estimated as function of hardness of the counterbody steel ball and sliding load. Further, the dominant mechanisms of material removal in third and fourth sets of experiments were studied and correlated with FSP parameters, reinforcement or sliding test conditions.



## Acknowledgement

---

First and foremost, I would like to express my gratitude and acknowledgement to almighty God who has given me enthusiasm and passion towards research work. My sincere thanks go to Dr. Ujjwal Prakash and Dr. B. V. Manoj kumar, Department of Metallurgical and Materials Engineering, Indian Institute of Technology Roorkee, my thesis supervisor for giving me the wonderful opportunity of doing research under them. Their enthusiasm on the problem and encouragement throughout the course of this work is very much appreciable. They have always been available for discussion and guided me to accomplish the objective of this study; they have been an inspiring and driving force during the course of this work. Without their timely help, intellectual input, constructive criticism and painstaking efforts, it would not have been possible for me to complete this thesis in the present form. I would like to acknowledge the other members of my Ph.D. committee, Dr. S.K. Nath, Dr. Anjan Sil, Dr. G.P. Chaudhari and Dr. P. K. Jha, who monitor my work and took effort in reading and providing me with valuable comments on earlier versions of this thesis.

I am deeply indebted to Prof. S.K. Nath, Head, Department of Metallurgical and Materials Engineering, Indian Institute of Technology Roorkee, for his help and providing the facilities in the department for the research work. Sincere thanks to the Head, Institute Instrumentation Centre, for their co-operation in providing excellent facilities during the entire course of my experiment work.

I wish to place my sincere thanks to the technical and the administrative staff of the Department of Metallurgical and Materials Engineering specially to Mr. R.K. Sharma, Mr. Rajendra Sharma, Mr. Naresh Sharma, Mr. Narendra, Mr. Ramveer Singh and Mr. S. Giri who have helped me in many ways during the course of my Ph.D. Thanks are also due to Mr. S.D. Sharma, Mr. Anil Saini, Mr. Shiv Kumar of IIC, for providing all the necessary help.

I would also like to thank my senior colleagues for creating an interesting and enthusiastic research atmosphere. I am especially grateful to Yashpal Gupta and Mr. Sandan Sharma. They gave me valuable comments and suggestions in completing this thesis work. My friends Yogesh Singla, Brij Kishore, Ravi Kant, Ashish Selokar, Ranjeet Yadav, PawanTripathi and

Yashwant Mehta were like my family member in Roorkee. We shared lot of happy experience like travelling outing, party, dining... I will always remember those happy days when we were together.

During my stay at IIT Roorkee I was associated with several friends and colleague. I appreciate each one of them for their moral support and cooperation which helped to keep things in perspective. Thanks to Paritosh Dubey, Himanshu Panjiar, Kaushal Chauhan, Ravi Kant, Sanjay Singh Rathore, Rajiv Sherawat and Tilak Joshi.

I would like to acknowledge the financial support from Department of Science and Technology (DST) Govt. of India through inspired fellowship for carrying out this research work.

The author expresses his deepest esteem to his parents and sister (RenuRichariya) for keeping their blessing over me. You're waited for many years to see this moment. Thank you for all sacrifices that you are made. I know it was not easy. You will be always with me in memories. Without you I would never be where I am now. Thank for giving me strength and the spark of hope when everything looked hopeless.

I also like to thank everyone who supported me for completing this work successfully and I express my apology that I could not mention everyone individually.

**(VIPIN SHARMA)**



---

<b>Abstract</b>		i
<b>Acknowledgement</b>		iii
<b>Contents</b>		v
<b>List of Figures</b>		ix
<b>List of Tables</b>		xvii
<b>List of Publications</b>		xix
Chapter 1	Introduction	1
	1.1 Objectives of the thesis	11
	1.2 Structure of the thesis	11
Chapter 2	Literature review	15
	2.1 Effect of process variables	15
	2.1.1 Effect of tool speeds	17
	2.1.2 Effect of multiple passes	20
	2.1.3 Direction of tool rotation	22
	2.1.4 Tool geometry	23
	2.1.5 Tool material and wear	24
	2.2 Effect of cooling	28
	2.3 Microstructural modification	29
	2.4 Effect of reinforcement particle on grain refinement	30
	2.5 Strengthening mechanisms	33
	2.5.1 Strengthening models	35
	2.6 Classification of FSPed surface composites	36
	2.6.1 Surface nano-composites	37
	2.6.2 Surface in-situ composites	41
	2.6.3 Surface hybrid composites	43
	2.7 Defects in FSPed composite surfaces	45
	2.8 Summary	47
Chapter 3	Experimental techniques	49

3.1	Aluminium alloys	49
3.2	Reinforcement particles	49
3.3	Friction stir processing setup	50
3.4	Tools	51
3.5	Processing	52
3.6	Volume percentage of reinforcement	53
3.7	Microscopic analysis	53
3.8	Hardness measurement	54
3.9	Tensile tests	54
3.10	Heat treatment	54
3.11	Sliding wear test	55
3.12	Profilometry	55
3.13	Wear mechanisms study	56
Chapter 4	Experimental procedure	57
4.1	Background	57
4.2	Effect of multi-pass FSP on microstructure and mechanical properties of AA2014-T651 alloy	57
4.2.1	Microstructural characterization	57
4.2.2	Hardness	61
4.2.3	Tensile behavior	62
4.2.4	Fracture surfaces	62
4.3	Microstructural and mechanical characterization of multi pass friction stir processed SiC/AA2014 and TiC/AA2014 surface composites	64
4.3.1	Microstructural study	64
4.3.2	Mechanical behavior	65
4.3.2.1	Hardness	65
4.3.2.2	Tensile strength	66
4.3.2.3	Fracture surface	67
4.4	Summary	69

Chapter 5	Friction stir processing strategies to achieve uniform distribution of reinforcement particles in surface composites	71
5.1	Background	71
5.2	FSP with variation in rotational and traverse speeds	73
5.3	Tool offset overlapping	77
5.4	Dual tool processing	78
5.5	Hardness of surface composites	80
5.6	Summary	81
Chapter 6	Fabrication and sliding wear behavior of ceramic and metallic particles reinforcement in friction stir processed surface composites	83
6.1	Background	83
6.2	Results and Discussion	85
6.2.1	Macrographs	85
6.2.2	Microstructures	86
6.2.2.1	Surface composite-A	87
6.2.2.2	Surface composite-B	88
6.2.2.3	Surface composite-C	89
6.2.2.4	Surface composite-D	91
6.2.3	Hardness	92
6.2.4	Friction characteristics	92
6.2.5	Wear volume	92
6.2.6	SEM-EDS analysis of surfaces worn at low load	95
6.2.7	SEM-EDS analysis of surfaces worn at high load	98
6.3	Summary	101
Chapter 7	Effect of counterbody hardness on sliding wear properties of friction stir processed surface composites	103
7.1	Background	103
7.2	Microstructure	105
7.3	Hardness	106
7.4	Friction characteristics	106

7.5	Wear results	108
7.6	Worn surface analysis	110
7.6.1	Surface analysis of materials worn against low hardness counter body	110
7.6.2	Surface analysis of materials worn against medium hardness counter body	114
7.6.3	Surface analysis of materials worn against high hardness counter body	117
7.7	Wear debris analysis	119
7.8	Summary	121
Chapter 8	Conclusions and future scope	123
8.1	Conclusions	123
8.2	Scope for future work	126
	References	127

<b>Figure No.</b>	<b>Title</b>	<b>Page No.</b>
Fig. 1.1	Schematic illustration of FSP	2
Fig. 1.2	Tool geometry of FSP tool	2
Fig. 1.3	Schematic of transverse section of processed zone	3
Fig. 1.4	Various microstructural zones in the friction stir processed material	4
Fig. 1.5	Schematic of dynamic recrystallization mechanisms operative in microstructural evolution (a) CDRX (b) GDRX (c) DDRX	5
Fig. 1.6	Common methods for placing reinforced particles in the fabrication of surface composites (a) by groove (b) by drilled holes (c) by using cover plate	7
Fig. 1.7	Schematic of wear mechanisms (a) abrasive wear (b) adhesive wear	9
Fig. 1.8	Schematic of wear mechanism encountered in AMCs (a) extrusion or flow wear (b) loose wear particles acting as a third body (c) tribofilm formation on the track	10
Fig. 1.9	The schematic outline of the doctoral investigation	13
Fig. 2.1	Classification of FSP process Variables	16
Fig. 2.2	Effect of passes on refinement of grains as indicated by EBSD images of the Al-TiC in-situ composite subjected to (a) single and (b) double pass FSP (Bauri et al., 2011)	21
Fig. 2.3	The tool probe geometry of commonly used tools in FSP (a) conical round bottom probe (b) columnar probe (c) threaded columnar probe (d) threaded columnar probe with flutes (e) triangular probe (f) square probe	23
Fig. 2.4	Schematic of pinning of the grain growth by reinforcement particles	31
Fig. 2.5	The improvement in micro-hardness of surface composites fabricated via FSP	34
Fig. 2.6	The ultimate tensile strength of surface composites fabricated via FSP	34

Fig. 2.7	Micrograph of SiC/A206 surface composite fabricated by FSP (a) strong bonding between the composite layer and matrix (b) uniform distribution of reinforced particles in the matrix (Sun and Apelian, 2011)	37
Fig. 2.8	SEM micrograph of uniformly distribution nano-size TiC reinforced in steel by FSP	37
Fig. 2.9	Carbon nano-structures reinforcement in surface composites (a) TEM image of MWCNT reinforced in AA5059 alloy after two passes of FSP (Izadi and Gerlich, 2012) (b) good bonding as showed in the interface between MWCNT and AA1016 alloy (Q. Liu et al., 2013). Arrows in (a) indicate survived CNTs after two passes	39
Fig. 2.10	Schematic of in-situ particles formation and dispersion in Al matrix during FSP	42
Fig. 3.1	SEM images of reinforcement (a) SiC particles (b) TiC particles	50
Fig. 3.2	Vertical milling machine used for FSP experiments	50
Fig. 3.3	Processed AA2014 after four passes of FSP	51
Fig. 3.4	Schematic design and fabricated tool of round bottom probe tool	51
Fig. 3.5	Sketch of square probe tool geometry utilized for fabrication of surface composites	52
Fig. 3.6	Dimensions of tensile test specimen	54
Fig. 3.7	Schematic of ball-on-disc wear testing	55
Fig.4.1	Macrographs of (a) one pass FSPed specimen (b) four pass FSPed specimen exhibiting various microstructural zones	58
Fig.4.2	Optical micrographs of (a) base alloy (b) one pass FSPed alloy (c) four pass FSPed alloy	59
Fig.4.3	SEM image of base alloy and corresponding EDS analysis of precipitates	59
Fig.4.4	Cross polarized optical micrographs of (a) base alloy exhibiting coarse precipitates (b) base alloy at higher magnification showing second phase continuous grain boundary network (c) one pass FSPed alloy (d) four pass FSPed alloy	60

Fig.4.5	TEM image of four pass FSPed SZ. The SAED pattern is shown in inset	60
Fig.4.6	Microhardness of SZ in base alloy, one pass and four pass FSPed specimens	61
Fig.4.7	Typical stress-strain curves for base alloy, one pass and four pass FSPed specimens	62
Fig.4.8	Fractographs of (a) base alloy (b) one pass FSPed specimen (c) four pass FSPed specimen	63
Fig.4.9	Optical images of SiC particles reinforced AA2014 surface composite (a) macrograph of transverse section (b) clustering of SiC particles in material flow lines (c) uniform distribution of SiC particles (d) clustering of SiC particles in shoulder affected region	64
Fig.4.10	Optical images of TiC particles reinforced AA2014 surface composite (a) macrograph of transverse section (b) TiC particles enriched band (c) uniform distribution of TiC particles	65
Fig.4.11	Comparison of microhardness of base alloy, FSPed alloy, SiC/AA2014 and TiC/AA2014	66
Fig.4.12	Stress-Strain curve of base alloy, FSPed alloy, SiC/AA2014 and TiC/AA2014	67
Fig.4.13	Representative SEM images of fractured surfaces: (a) base alloy (b) magnified view of a region in (a) (c) FSPed alloy (d) SiC/AA2014 surface composite exhibiting particles cracking (e) clustering of SiC creates large microvoid in SiC/AA2104(f) TiC/AA2014 surface composite	68
Fig.5.1	Schematic top view of reinforcement particles distribution in FSP	72
Fig.5.2	Stitched optical micrographs of surface composites fabricated by four passes of FSP at (a) 1000 rpm-25 mm/min (b) 1000 rpm-40 mm/min (c) 1400 rpm-25 mm/min (d) 1400 rpm-40 mm/min (e) top surface of 1400 rpm-40 mm/min (f) 2000 rpm-40 mm/min	74
Fig.5.3	Schematic cross sectional view of reinforcement particle distribution in FSP using high rotational speed	77

Fig.5.4	Stitched optical micrographs of surface composites fabricated by tool offset overlapping passes at a rotational speed of 1400 rpm and a traverse speed of 40 mm/min. (a) one additional pass on previous four passes of FSP (b) two additional passes on previous four passes of FSP	78
Fig.5.5	(a) stitched optical micrographs of surface composites fabricated by two additional passes with the bigger diameter probe (b) EDS mapping of SZ processed by 6 mm probe diameter tool (c) void in SZ processed by 6 mm probe diameter tool	79
Fig.5.6	Hardness variation of surface composites	80
Fig. 6.1	The stitched optical micrographs of surface composite (a) A (b) B (c) C (d) D. Refer Table 6.1 for designation of surface composites	86
Fig. 6.2	Optical and SEM images of (a) surface composite A (b) base alloy (c) SZ-TMAZ interface (d) SZ (e) onion ring in SZ sliced section along processing direction (f) SEM image of SZ	88
Fig. 6.3	Optical and SEM images of surface composite B: (a) SZ-TMAZ interface (b) magnified view of bands in SZ-TMAZ interface (c) SZ (d) SEM micrograph of SZ-TMAZ interface (e) SEM image of SZ	89
Fig. 6.4	Optical images of surface composite C (a) SZ-TMAZ interface (b) SZ (c) onion ring pattern (d) bands on the RS of SZ (e) bands in material flow lines (f) magnified view of particle-free band region	90
Fig. 6.5	Optical and SEM images of surface composite D (a) SZ-TMAZ interface (b) SZ (c) onion ring pattern (d) bands on the RS of SZ (e) bands in material flow lines (f) magnified view of particle-free band region	91
Fig. 6.6	Hardness of base alloy and surface composites	92
Fig. 6.7	Coefficient of friction of base alloy and surface composites at 5 N and 20 N load	93
Fig. 6.8	The wear volume of base alloy and surface composites of LM24 after sliding against steel ball at (a) 5 N load and (b) 20 N load	94



Fig. 6.9	SEM micrographs of worn surface of base and surface composites slid against 5N load (a) base alloy exhibiting flow wear (b) microcrack formation in base alloy (c) surface composite A (d) surface composite B (e) surface composite C (f) surface composite D	96
Fig. 6.10	EDS analysis of worn surface (a) surface composite A (b) surface composite B (c) surface composite C (d) surface composite D	98
Fig. 6.11	SEM micrograph of worn surface of base alloy and surface composites at 20 N load (a) base alloy (b) surface composite A (c) surface composite B (d) surface composite C (e) surface composite D	99
Fig. 6.12	EDS analysis of worn surface of (a) base alloy (b) surface composite A (c) surface composite B (d) surface composite C	100
Fig.7.1	Optical micrographs (a) base alloy (b) FSPed alloy at SZ-TMAZ interface (c) Al <sub>2</sub> O <sub>3</sub> /AA5083 surface composite	105
Fig.7.2	Microhardness across the transverse sections of FSPed base alloy and surface composite	106
Fig.7.3	Coefficient of friction for the investigated surface composites of alumina/AA5083 surface composites. BLH: base alloy against low hardness ball; CLH: surface composite against low hardness ball; BMH: base alloy against medium hardness ball; CMH: surface composite against medium hardness ball; BHH: base alloy against high hardness ball; CLH: surface composite against high hardness ball	107
Fig.7.4	Representative COF curves for base alloy and surface composites slid against (a) low hardness steel ball (b) medium hardness steel ball and (c) high hardness steel ball. BLH: base alloy against low hardness ball; CLH: surface composite against low hardness ball; BMH: base alloy against medium hardness ball; CMH: surface composite against medium hardness ball; BHH: base alloy against high hardness ball; CLH: surface composite against high hardness ball	108
Fig.7.5	Typical worn surface profiles of surface composites slid against	109

	counterbody steel balls with difference in hardness. LH: low hardness; MH: medium hardness; HH: high hardness	
Fig.7.6	Wear volume of surface composites at 5 N and 20 N loads as function of hardness of counterbody steel ball. LHC: low hardness counterbody; MHC: medium hardness counterbody; HHC: high hardness counterbody	109
Fig.7.7	SEM images of worn surfaces after sliding against low hardness steel ball: (a) base alloy at 5 N load (b) FSPed alloy at 5 N (c) surface composite at 5 N load (d) base alloy at 20 N load (e) FSPed alloy at 20 N load (f) surface composite at 20 N load (g) higher magnification view of Fig. (f)	111
Fig.7.8	EDS analysis of worn surfaces after sliding against low hardness steel ball: (a) surface composite at 20 N load (b) layer formed on surface composite at 20 N load (c) FSPed alloy at 20 N load (d) surface composite at 5 N load (e) ball surface slid against surface composite at 20 N load	113
Fig.7.9	3-D optical profilometer images of low hardness steel ball after sliding against surface composites at (a) 5 N load (b) 20 N load	114
Fig.7.10	SEM images of worn surfaces after sliding against medium hardness steel ball: (a) base alloy at 5 N load (b) FSPed alloy at 5 N (c) surface composite at 5 N load (d) base alloy at 20 N load (e) higher magnification view of Fig. (d) (f) FSPed alloy at 20 N load (g) surface composite at 20 N load	115
Fig.7.11	EDS analysis of worn surfaces after sliding against medium hardness steel ball: (a) surface composite at 5 N load (b) surface composite at 20 N load (c) ball surface slid against surface composite at 20 N load	116
Fig.7.12	SEM images of worn surfaces after sliding against high hardness steel ball: (a) base alloy at 5 N load (b) FSPed alloy at 5 N (c) surface composite at 5 N load (d) base alloy at 20 N load (e) FSPed alloy at 20 N (f) surface composite at 20 N load.	118
Fig.7.13	EDS analysis of worn surfaces after sliding against high hardness steel ball: (a) surface composite at 5 N load (b) surface composite at 20 N load (c) counterbody at 20 N load.	119
Fig.7.14	Wear debris of worn surfaces after sliding against high hardness steel ball:	120

(a) base alloy at 20 N load (b) FSPed alloy at 20 N load (c) surface composite at 5 N load (d) surface composite at 20 N load (e) EDS analysis of wear debris generated at 20 N load.



## **List of Tables**

---

<b>Table No.</b>	<b>Title</b>	<b>Page No.</b>
Table 2.1	Successful combination of rotational and traverse speeds for surface composite fabrication	19
Table 2.2	Tool materials utilized for surface composite fabrication and processing of various alloys	25
Table 2.3	Grain refinement obtained in surface composites and alloys by FSP	29
Table 2.4	Grain refinement of matrix by the pinning effect of reinforcement particles	31
Table 2.5	Common types of defects observed in FSW of alloys (Arbegast, 2008)	46
Table 3.1	Chemical composition of as received AA2014	49
Table 3.2	Chemical composition of as received AA5083	49
Table 3.3	Chemical composition of as received LM24 alloy	49
Table 6.1	Designation and details of reinforcement and tool speeds of LM24 surface composites	85



### In International Journals:

- Vipin Sharma, Ujjwal Prakash and B.V. Manoj Kumar. "Surface Composites by Friction Stir Processing: A Review." *Journal of Materials Processing Technology* 224, 117-134 (2015).
- Vipin Sharma, U. Prakash and B.V. Manoj Kumar. "Microstructural and mechanical characteristics of AA2014/SiC surface composite fabricated by friction stir processing" accepted for publication in *Materials Today: Proceedings* (in press, DOI: 10.1016/j.matpr.2015.07.229)
- Vipin Sharma, Yashpal, B.V. Manoj Kumar and Ujjwal Prakash. "Friction stir processing strategies for uniform distribution of reinforcement in a surface composite". Provisionally accepted in *Materials and Manufacturing Processes*.

### Book Chapter:

- Vipin Sharma, Ujjwal Prakash and B. V. Manoj Kumar, "Challenges in fabrication of surface composites by friction stir processing route, *Advanced Composites for Aerospace, Marine and Land Applications II* (Ed. T. Sano and T.S. Srivatsan), TMS (The Minerals, Metals & Materials Society), John Wiley & Sons 2015 pp 93-100 (ISBN 978-1-119-08226-2)

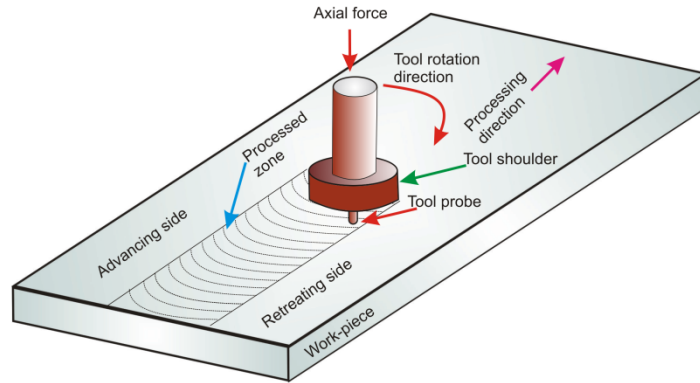
### In conferences:

- Vipin Sharma, U. Prakash and B. V. Manoj Kumar, "Effect of cooling on microstructure and mechanical properties of friction stir processed surface composites", in the proceedings of 23rd International Conference on Processing and Fabrication of Advanced Materials (PFAM 2014), December 2014, IIT Roorkee
- Vipin Sharma, R. Singh, P. Tripathi, B.V. Manoj Kumar and U. Prakash, "Microstructural and mechanical properties of aluminum-silicon alloy by multi-pass friction stir processing", International conference on emerging materials and applications (ICEMA 2014), 5-6 April, 2014 at IIT Roorkee Saharanpur campus.

Friction stir processing (FSP) is a relatively new technique of severe plastic deformation (SPD) for microstructural modification of advanced materials (Ni 2014) and is an adaption of friction stir welding (FSW) (Mishra 2003). Investigations carried out in past decade have shown a great potential for extraordinary improvement in physical and mechanical properties of many metals and alloys by grain refinement via severe plastic deformation (SPD) (Valiev 2000). While several SPD processing techniques like equal-channel angular pressing (Valiev and Langdon 2006), high-pressure torsion (Sakai 2005), multi-directional forging (Sakai 2008), accumulative roll-bonding (Saito 1999), FSP (Kwon 2002) etc. are developed, a simple and versatile technique and the ability to achieve superior properties in FSP attracted research community to a large extent. Further, most of the SPD techniques modify bulk properties, whereas FSP involves only surface modification.

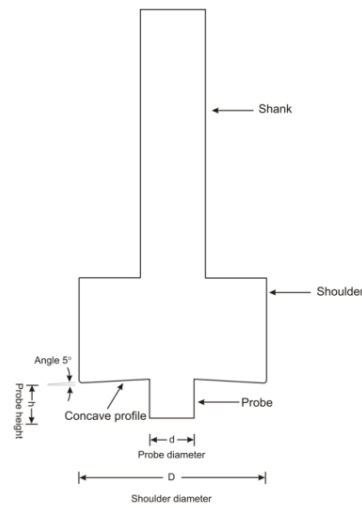
Earlier studies on FSP focused in producing aluminum alloys with very fine grain size and high grain boundary misorientations to achieve superplastic behavior (Mishra 1999). After successful refinement of microstructures of aluminum and magnesium alloys, FSP development has further led to the successful processing of alloys of copper (Barmouz 2011a), titanium (Shamsipur 2011) and steel (Ghasemi-Kahrizsangi and Kashani-Bozorg 2012). FSP also exhibited efficiency in homogenizing aluminum alloys (Berbon 2001) and microstructural modification of metal matrix composites prepared via powder metallurgy route (Gan 2010). As FSP is a solid state process, problems related to solidification and the presence of brittle inter-dendritic and eutectic phases are eliminated (Mishra and Ma 2005). FSP also dissolves or breaks up second phase particles and lead to the considerable improvement in properties in cast alloys (Sun and Apelian 2011; Argade 2012). FSP in its simplest form consists of a non-consumable rotating tool with a probe, which is plunged into a workpiece and then moved in the direction of interest. The schematic illustration of FSP is shown in Fig. 1.1.





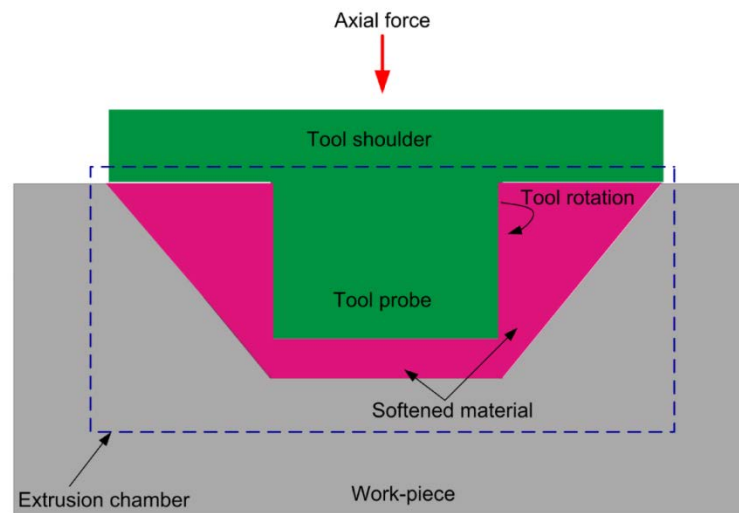
**Fig. 1.1:** Schematic illustration of FSP

Typical tool used for FSP mainly consists of pin or probe, shoulder and shank, as presented in Fig. 1.2. The geometry of the tool includes shoulder diameter, shoulder shape, probe shape and probe size. Tool geometry is an important aspect of FSP as it affects heat generation, material flow and resultant microstructures (Mishra and Ma 2005). A tool with concave shaped shoulder is usually preferred as it serves as an escape volume or reservoir for the displaced or plasticized material from the probe. Furthermore, tilt angle of the tool is necessary to maintain the material reservoir beneath the tool and to enable trailing edge of the shoulder in extruding the processed material. A tilt angle of  $1-3^\circ$  is recommended for effective processing of the material (Sharma 2015). A tool with a large diameter shoulder generates large amount of heat and enhances material flow, whereas that with small diameter shoulder forms defects in the composite (Elangovan and Balasubramanian 2008).



**Fig. 1.2:** Tool geometry of FSP tool

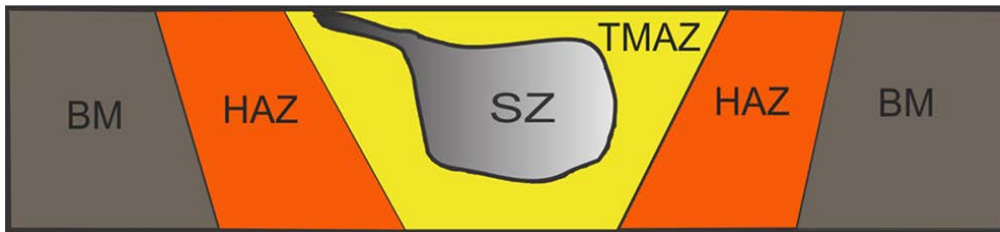
The FSP tool serves two primary functions: (a) heating and (b) deformation of workpiece material. The heat is generated mainly by the friction of the rotating shoulder with the workpiece, while rotating probe or pin stirs the heated material. The heated material softens and flows around the rotating pin. It then fills the cavity at the rear of the tool (Mironov 2008). Severe plastic deformation and thermal exposure occurs in the material that flows around the tool leading to a significant refinement of microstructure. Similar to FSW, FSP is also a combination of deformation, stirring, extrusion, forging and consolidation processes (Lorrain 2010). The probe stirs the softened material while tool axial force provides forging action. Processed zone is analogous to extrusion chamber surrounded by cold material (unprocessed material) and tool, as shown in Fig. 1.3. The softened material is stirred and extruded as tool traverses, and leads to consolidation to form a processed zone at trailing edge of the tool (Lorrain 2010; Guerra 2003).



**Fig. 1.3:** Schematic of transverse section of processed zone

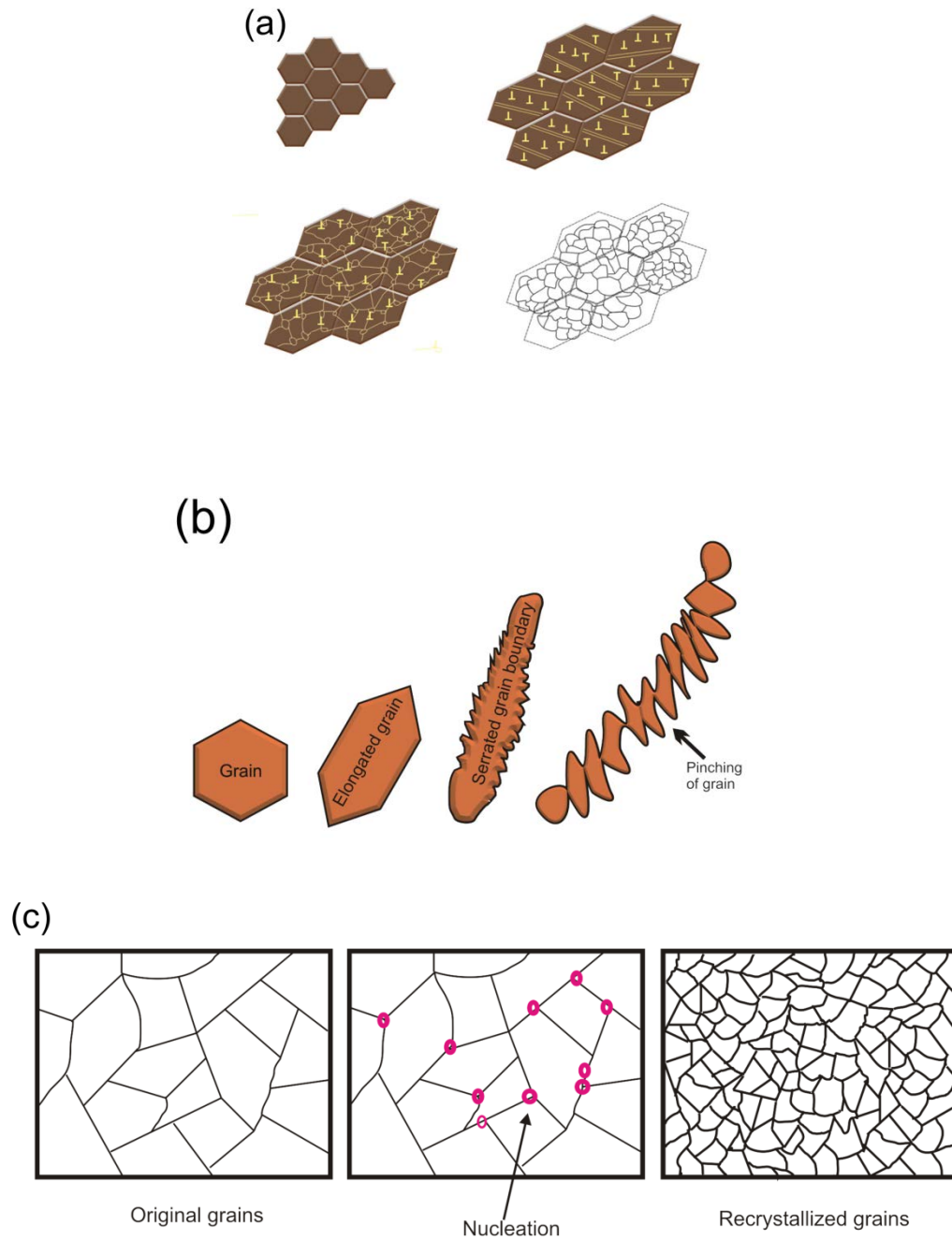
The translation of rotating tool creates a characteristic asymmetry between two sides of the processed zone i.e. advancing side (AS) and retreating side (RS). In the AS, tool rotation direction is the same as the tool traverse direction, whereas in the RS the tool rotation direction is opposite to the tool traverse direction (Ma 2008). Three distinct zones namely, stir zone (SZ), thermo mechanically affected zone (TMAZ) and heat affected zone (HAZ) commonly evolve in FSP (Mishra and Ma 2005). Fig. 1.4 shows various microstructural zones in the friction stir processed material. SZ refers to the zone stirred by the tool probe, TMAZ is the zone affected by plastic

deformation and heat generated nearby the SZ, whereas HAZ experiences heat generated by processing.



**Fig. 1.4:** Various microstructural zones in the friction stir processed material

With regards to the mechanism, dynamic recrystallization (DRX) is reported to be responsible for the generation of fine and equiaxed grains in the stir zone (SZ). However, dynamic recovery is observed to precede DRX in high stacking fault energy materials such as aluminum and its alloys (McNelly 2008). DRX mechanisms including continuous dynamic recrystallization (CDRX), discontinuous dynamic recrystallization (DDRX) and geometric dynamic recrystallization (GDRX) are generally reported. The evolution of these important mechanisms of DRX is schematically provided in Fig. 1.5 (Jata and Semiatin 2000; Robson and Campbell 2008; Giribaskar 2008). Various stages are shown sequentially in Fig. 1.5 for better understanding, but they are believed to occur simultaneously. In CDRX (as shown in Fig. 1.5a), grain boundary hindered dislocations are arranged to form subgrain structures with low-angle boundaries. As deformation progresses, the misorientation increases by rotation of subgrain structure and eventually grain formation occurs (Gourdet and Montheillet 2003). In GDRX mechanism, as presented in Fig. 1.5 (b), grains are elongated or flattened during deformation, leading to serrated grain boundaries. Further deformation causes contact of boundaries and formation of new grains (Prangnell and Heason 2005). On the other hand, DDRX mechanism involves nucleation of small grains, as similar to classical recrystallization mechanism (Fig. 1.5c). After nucleation, high angle grain boundaries are migrated to reduce stored energy to accommodate energy difference between the newly formed grains and previously deformed grains (Su 2005).



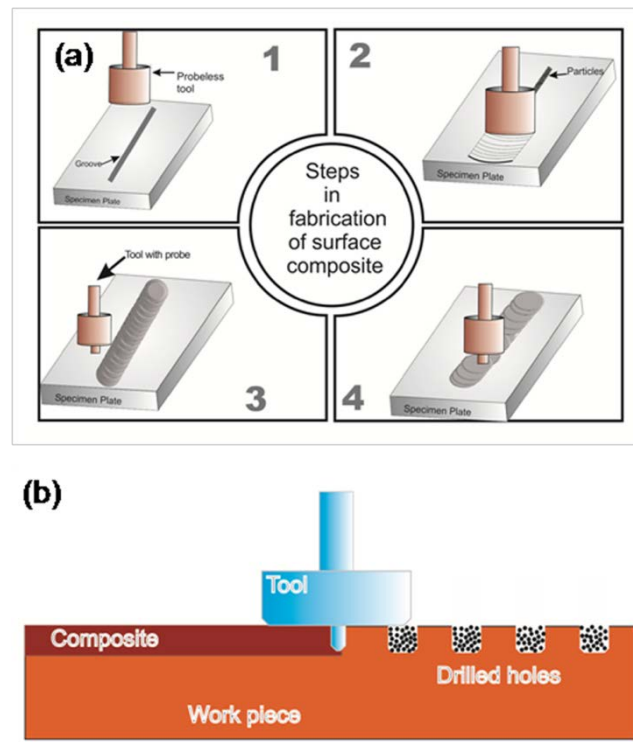
**Fig. 1.5:** Schematic of dynamic recrystallization mechanisms operative in microstructural evolution (a) CDRX (b) GDRX (c) DDRX.

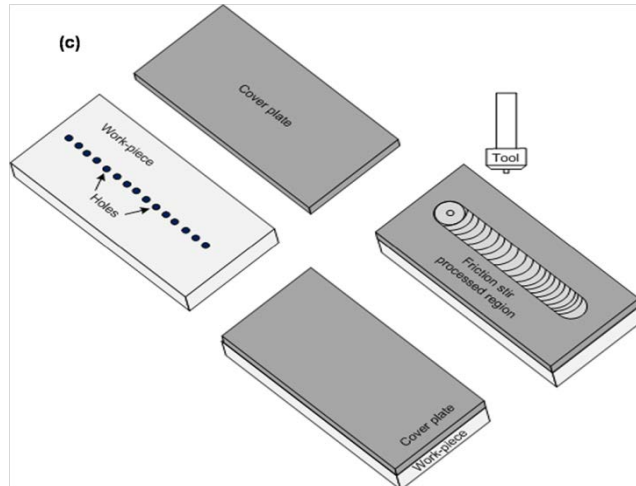
For engineering applications involving surface contacts, the useful function of component is mainly influenced by the surface properties such as hardness, yield strength and wear resistance. Therefore, it is highly desirable that surface of the component exhibits superior strength and hardness while material beneath the surface maintains the original structure with good ductility and

toughness (Arora 2011; Sharma 2015). Such specific requirement of material can be suitably achieved in surface composites. The attracting potential of FSP in modifying surface microstructures and preparation of surface composites is recently identified.

Conventional techniques for fabricating surface composites such as laser melt treatment and plasma spraying involve liquid phase processing at high temperatures that may lead to the interfacial reaction between reinforcement and the metal matrix and deteriorate composite properties (Pantelis 1995; Meng 2013; Kakitsuji 2002). Moreover, precise control of processing parameters is required to obtain desired microstructure in surface layer after solidification. Mishra et al. (2003) explored the potential of FSP technique in fabricating silicon carbide (SiC) reinforced surface composite layer on aluminum (Al) 5083 alloy. Since then, a variety of surface composites based on magnesium, copper, titanium and steel have been developed.

FSP has demonstrated its potential in fabrication of all variants of surface composites with little or no interfacial reaction with the reinforcement. In earlier studies, surface composites were fabricated by applying a layer of ceramic particles slurry in a volatile medium (Mishra 2003), while ceramic particles are reinforced through a machined groove in the specimen plate in recent studies (Arora 2011). The major approaches in surface composite fabrication via FSP are schematically presented in Fig. 1.6 (a-c).





**Fig. 1.6:** Common methods for placing reinforced particles in the fabrication of surface composites (a) by groove (b) by drilled holes (c) by using cover plate

Steps in groove method are explained in Fig. 1.6(a). In the first step, the groove is machined on the plate and reinforcement particles are filled in the groove. The second step consists of applying tool without probe (pin) on the groove. The groove is completely packed. In the last step, the tool with probe is applied on the packed groove. The dimension, shape and number of grooves can be varied to achieve required volume fraction of second phases. Surface composite fabrication by drilled-hole method is shown in Fig. 1.6(b). In this method, the intermediate step of packing the groove by probe-less tool is eliminated by incorporating reinforcement through drilled holes. The loss of reinforced particles during FSP is prevented by sealing of holes by the half portion of shoulder ahead the traveling pin (Li 2013). Instead of single array of drilled holes, two arrays were also used to achieve uniform distribution of particles (Akramifard 2014). In other studies, a thin sheet was covered over the groove or drilled holes to avoid the ejection of reinforcement particles, as shown in Fig. 1.6(c) (Lim 2009; Avettand-Fenoel 2014). Huang et al. (2014) used an approach of direct friction stir processing (DFSP) to fabricate surface composite layer on AZ31 matrix. They used hollow and probe-less tool pre-filled with SiC particles. The particles flowed out through the through-hole of 8 mm diameter in the centre of DFSP tool and entered the enclosed space between concave shoulder and AZ31 workpiece. SiC particles were then pressed into the workpiece as the rotating tool traversed in processing direction.

Several other approaches have also been applied to fabricate surface composites. Friction stir surfacing is also used by many researchers to fabricate surface composite coating over the

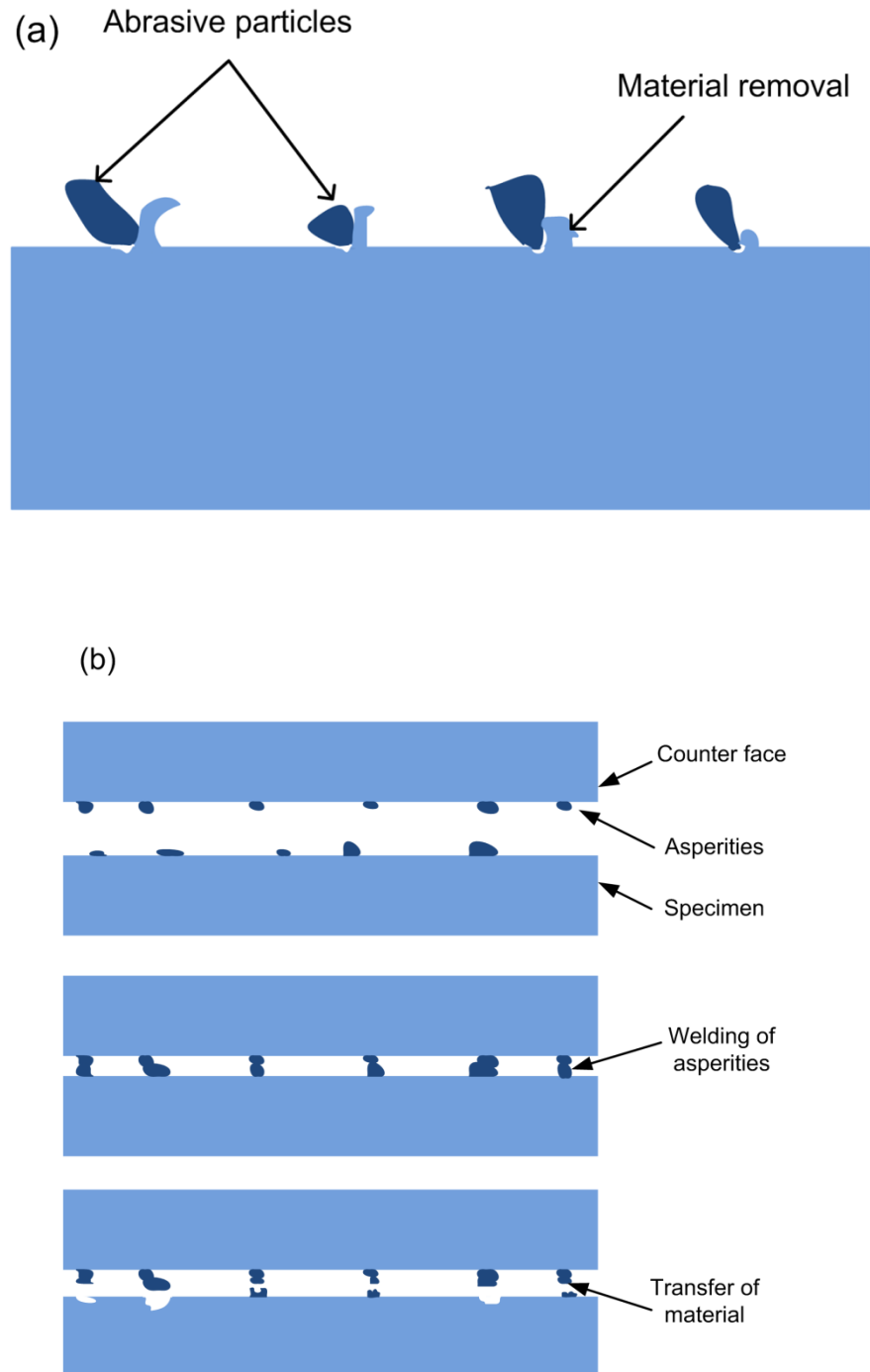
substrate. In this process, a tool is filled with reinforcement particles and consumed to form a layer of composite on the workpiece (Miranda 2013; Gandra 2014). Applying composite powder coating on the workpiece and subsequent FSP on the coating is also a new approach for surface composite fabrication. In groove method, the reinforced area is limited to SZ as the distribution of particles is governed by pin rather than shoulder. Additionally, there are possibilities of defects like worm holes or unfilled groove after FSP. The distribution of particles into a wider region can be achieved by application of composite coating on the alloy plate and subsequent FSP (Zahmatkesh and Enayati 2010; Mazaheri 2011; Hodder 2012).

In FSP of surface composites, tool rotation speed and tool traverse speed are very important parameters. The rotation speed of tool influences generation of heat and stirring or mixing of material, whereas the traverse speed causes movement of stirred material from front side to back side of the tool (Mishra and Ma 2005). Higher rotational speed generates higher temperature, whereas high traverse speed results in less heat accumulation in the processed zone. In multi-pass method, the processing is performed over the previously processed zone. Multi-passes in FSP are commonly used for homogeneous distribution of second phase particles (Zohoor 2012).

The combination of rotational speed and traverse speed determines the heat input in the processed zone. The amount of heat input significantly affect the resultant microstructure and thus mechanical or tribological properties. So, there is a need for the systematic investigation of the process parameters effect on the microstructure, mechanical and tribological properties of FSPed surface composites.

Aluminum alloys are suitable class of materials for engineering applications due to light weight, high specific strength and ease in fabrication but lacks in tribological performance (Kumar 2012). The advancement in composite materials provides a material with good combination of tribological and mechanical properties (Bijwe 1997; Gurunath 2007; Rajesh 20002). The inferiority of aluminum alloys in tribological performance can be overcome by the development of aluminum matrix composites (AMCs) by reinforcing hard ceramic particles (Basu and Kalin 2011; Borgonovo and Apelian 2011). Study of tribological characteristics of AMCs is of prime importance to understand wear mechanisms encountered in sliding system. The wear mechanisms and parameters affecting tribological characteristics provide a better understanding for developing composites with superior wear resistance (Kumar 2013; Ramkumar 2003; Sankar 2009). In sliding wear of AMCs, abrasive and adhesive wear are reported as dominating wear mechanisms (Roy 2005).

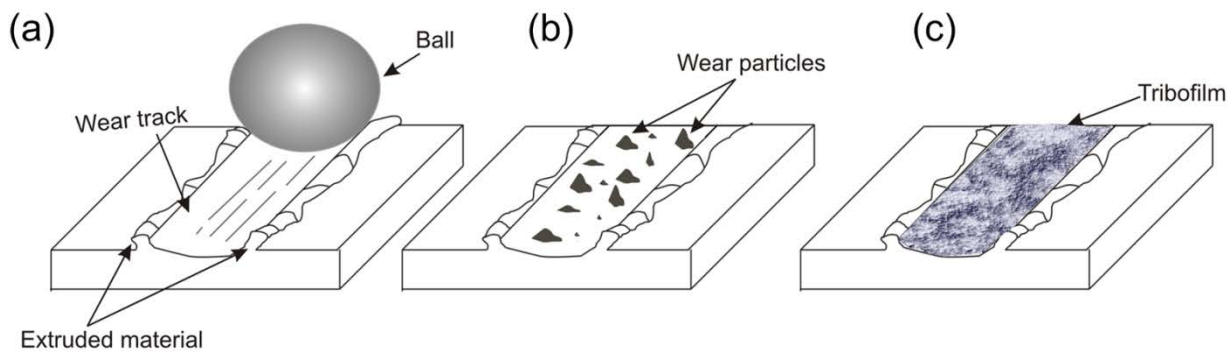
Abrasive wear is defined as ‘wear due to hard particles or hard protuberances forced against and moving along a solid surface (ASTM, 2013)’. Adhesive wear is a ‘wear due to localized bonding between contacting solid surfaces leading to material transfer between the two surfaces or loss from either surface (ASTM, 2013)’. The abrasive and adhesive wear mechanisms are schematically shown in Fig. 1.7 (a, b).



**Fig.1.7:** Schematic of wear mechanisms (a) abrasive wear (b) adhesive wear



Material transfer characteristics in a tribosystem also alter friction and wear mechanism. In dry sliding wear of aluminum alloy composites, material transfer is dominant and known to increase or decrease the wear (Rigney, 1984). The transferred material disintegrates into wear debris act as a third body or consolidates to form a tribolayer (Fig. 1.8). Tribolayer formation and its stability reduce the wear rate, whereas the presence of third body owing to abrasion of loose debris increases the wear rate (Li and Tandon 2000; Sundarajan 1996; Venkataraman 1996). The formation and stability of tribolayer mainly depends on many factors including characteristics of transferred material and tribochemical reactions. The chemistry and size of reinforcement particles play dominant role in material transfer and tribochemical reactions (Alpas and Zhang, 1994; Kim 2007; Venkataraman 2000).



**Fig. 1.8:** Schematic of wear mechanism encountered in AMCs (a) extrusion or flow wear (b) loose wear particles acting as a third body (c) tribofilm formation on the track.

While microstructural characteristics and mechanical or wear behavior of aluminium alloy composites prepared by conventional techniques are well reported, effects of FSP parameters on microstructure and tribological performance of aluminium alloy surface composites are not systematically studied. In particular, the effect of rotational speed, traverse speed, external cooling, tool geometry, multi-pass on uniform distribution of reinforcement particles and resultant mechanical and wear properties are not considerably understood. The present investigation deals with the development of particles reinforced surface composites of aluminum alloys by varying parameters. The friction and wear characteristics of FSPed surface composites in sliding wear conditions are also investigated.

## **1.1.Objectives of the thesis:**

The major aim of the present study is to understand the effect of FSP parameters in achieving uniform distribution of reinforcement particles in aluminium alloy surface composites. A relationship between FSP parameters-microstructure-mechanical property-tribological behaviour is also an important objective. The other important aim of the present study is to elucidate mechanisms of material removal as function of FSP parameters and sliding test conditions. The following are major objectives of the present investigation:

- To develop strategies of FSP to achieve uniform distribution of reinforcement particles in the aluminium alloy surface composites.
- To study friction and wear characteristics of ceramic or metallic particles reinforced surface composites in sliding conditions against steel ball
- To study the effect of sliding test parameters like load and counterbody hardness on tribological performance of FSPed aluminium alloy surface composites
- To correlate the microstructural or compositional features of FSPed surface composites with the dormant mechanisms of material removal.

## **1.2.Structure of the thesis:**

An outline of the present doctoral investigation is presented as Fig. 1.9. In order to envisage the above listed objectives, the thesis is structured as per the following:

### **Chapter-2 Literature review**

A comprehensive review on development, microstructures and mechanical or wear behavior of surface composites prepared by FSP is provided in this chapter.

### **Chapter-3 Experimental techniques**

This chapter includes the materials, experimental techniques involved in the present study for fabricating surface composites and evaluating tribological properties.

### **Chapter-4 Fabrication of multi pass FSPed aluminum alloy surface composites**

In this chapter, the effect of multiple passes of FSP on the microstructure and mechanical properties of AA2014-T651 alloy is first studied to understand the mechanism of precipitate overaging. This is followed by the study of microstructural and mechanical properties of reinforcement of SiC or TiC particles in AA2014 surface composites.

### **Chapter -5 Friction stir processing strategies to achieve uniform distribution of reinforcement particles in aluminum alloy surface composites**

Strategies like varying rotational and traverse speeds, two-step FSP utilizing bigger probe diameter, overlapping passes are investigated for fabricating SiC particles reinforced AA5083 alloy surface composites. The microstructure and mechanical behaviour are presented.

#### **Chapter-6 Tribological characterization of ceramic and metallic particles reinforced aluminum alloy surface composites**

This chapter deals with the study of microstructural, mechanical and tribological properties of surface composites reinforced with graphite and tin in LM24 alloy. The surface composites are fabricated with different heat input conditions varied by manipulating the rotational speed.

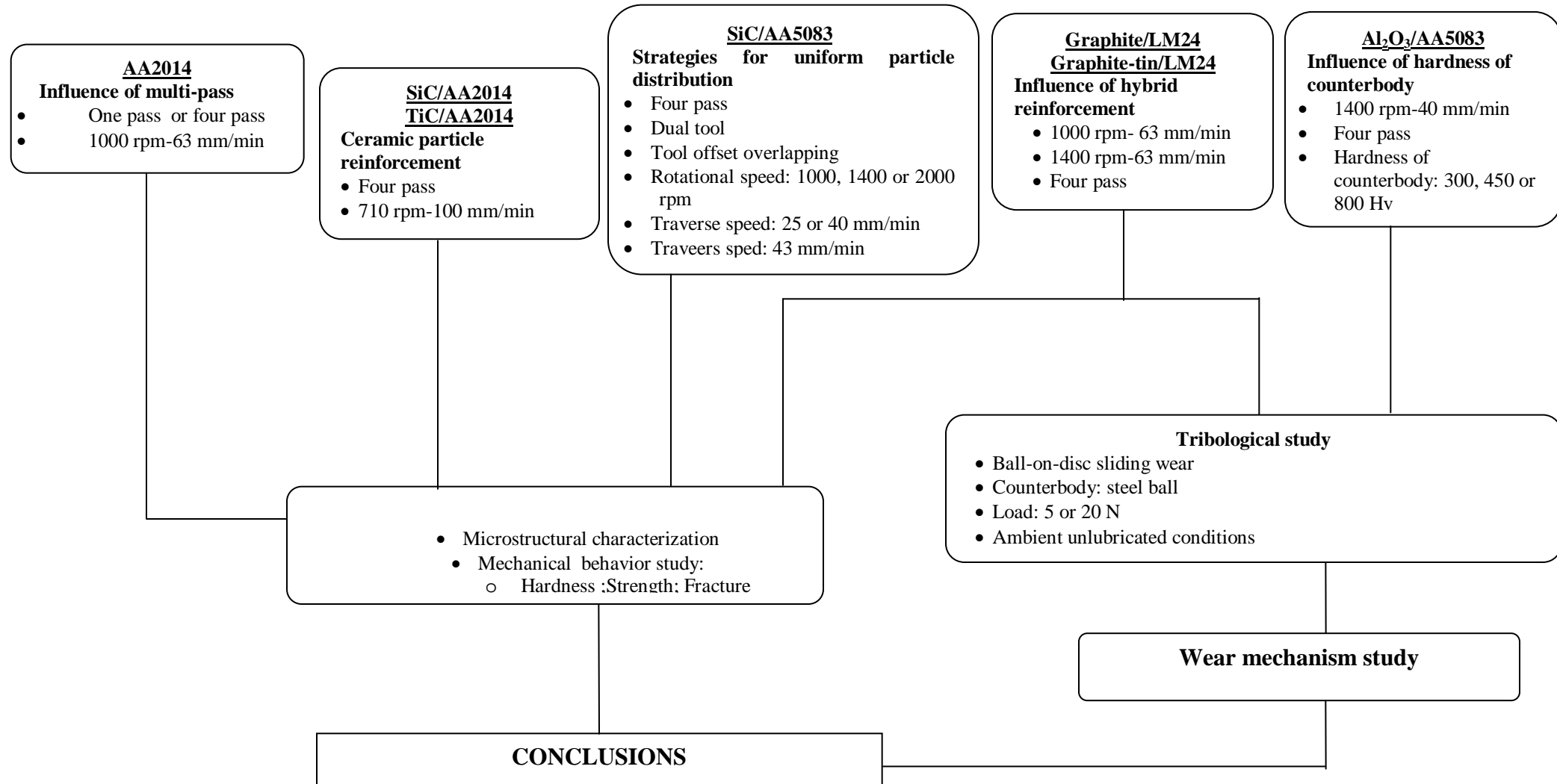
#### **Chapter-7 Effect of counterbody hardness on tribological performance of aluminium alloy surface composites**

This chapter includes results obtained from the study of counterbody hardness effect on the tribological properties of alumina reinforced AA5083 surface composites. A steel ball with different hardness was used as counterbody for studying the sliding wear characteristics of surface composites.

#### **Chapter-8 Conclusions and future scope**

Major conclusions on the effect of process parameters on microstructural and mechanical characteristics of FSPed aluminium alloy surface composites are provided. This is followed by the list of salient observations from tribological study of FSPed surfaces. Finally, directions for further work on understanding the relation between process parameters, microstructure and tribological properties of FSPed aluminium alloy surface composites are listed.

## Friction stir processing and tribology of Al alloy surface composites



**Fig. 1.9:** The schematic outline of the doctoral investigation



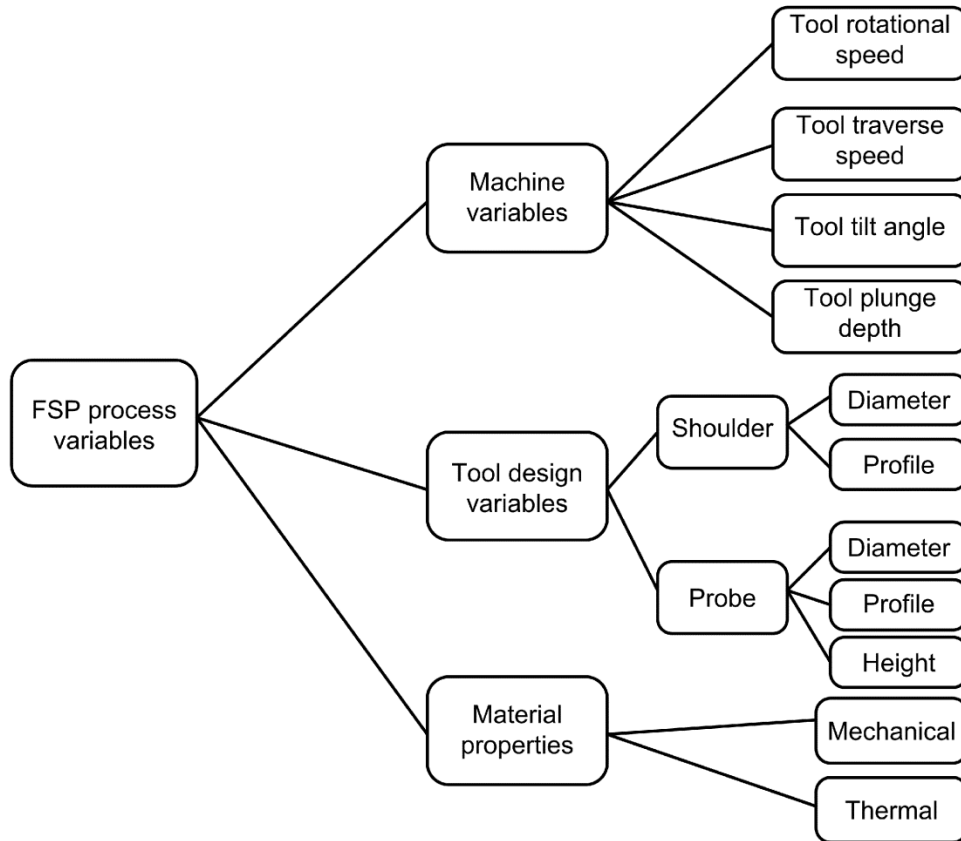
---

*In this chapter, a comprehensive understanding on the available literature on friction stir processed surface composites is provided. The available literature is classified to present details about effect of process parameters, reinforcement particles, active cooling and multiple passes on microstructure evolution during fabrication of surface composites. The microstructure and mechanical characteristics of friction stir processed surface micro-composites, nano-composites, in-situ composites and hybrid composites are discussed. Considering the importance of tool wear in FSP of high melting point and hard surface composites, a brief note on tool materials and the limitation in their usage is also provided. Also, the dominant wear mechanisms in aluminium alloy surface composites prepared by friction stir processing are discussed.*

### **2.1 Effect of process variables**

These fall into three categories of machine variables, tool design variables and material properties (Fig. 2.1). The mechanical properties of base materials are decisive in selecting process variables. High heat input is required for high melting point materials like steel, titanium alloys, copper alloys etc. (Heidarzadeh 2014). Balasubramanian (2008) stated that yield strength (YS), ductility and hardness of base material are important mechanical properties that control plastic deformation during FSW. In aluminium alloys with different mechanical properties, it was found that the material with lower YS, lower hardness and higher ductility can be processed easier than those with higher YS, higher hardness and lower ductility.

Thermal properties of material govern the peak temperature during processing. In high thermal conductivity materials, more heat input is required to obtain defect free processing (Xu 2014). The high thermal conductivity of material would allow more heat loss by conduction (Khandkar 2003). To manipulate thermal properties a backing plate beneath the work-piece was used in FSW (Upadhyay and Reynolds 2012; Rosales 2010).



**Fig. 2.1:** Classification of FSP process Variables

Major machine variables are tool rotating rate and tool traverse speed. Tool rotational and transverse speeds determine amount of heat generated in the work piece (Dolatkhah 2012). Tool tilt angle and penetration depth also effect the formation of SZ, but generally these are kept constant (Redyy 2011). Interaction of rotating tool with work-piece generates heat due to friction and plastic deformation. The heat input in SZ influences material flow and microstructure evolution which directly affects mechanical and tribological properties. Tool rotational speed and traverse speed determine amount of heat input in the processed zone (Khayyamin 2013). The maximum temperature observed for various aluminum alloys has been reported to be in a range of 0.6-0.9  $T_m$ . Sufficient amount of heat generation in SZ is necessary for the formation of defect-free processing zone (Mishra and Ma 2005). Similarly, in FSP of other alloys like magnesium, copper and titanium alloys heat generation in the processed zone is dependent on rotational and traverse speeds (Azizieh 2011; Barmouz 2011a; Li 2013).

Based on experimental observations for Friction Stir Welding (FSW) of aluminum alloys, the following empirical relationship between the maximum temperature ( $T_{max}$ ) in SZ and the

processing parameters of rotational speed ( $\omega$ ) and traverse speed ( $v$ ) has been proposed (Arbegast and Hartley 1998):

$$\frac{T_{\max}}{T_m} = K \left( \frac{\omega^2}{v \times 10^4} \right)^\alpha \dots\dots\dots (2.1)$$

where the constant  $K$  is reported between 0.65 and 0.75, the exponent  $\alpha$  ranges from 0.04 to 0.06 and  $T_m$  ( $^\circ$  C) is the melting point of alloy. The ratio between  $\omega^2$  and  $v$  is considered as pseudo heat index. In FSW of thin AA2024 sheet, Fu et al. (2013) demonstrated that the relationship between peak temperature ( $T_{\max}$ ) and heat index value is in accordance with the Eq. 2.1, i.e. the peak temperature is proportional to the heat index value. The average heat input per unit length is estimated as per the following according to the model by Frigaard et al. (2001).

$$Q = \frac{4}{3} \pi^2 \frac{\alpha \mu P \omega R^3}{v} \dots\dots\dots (2.2)$$

where,  $\alpha$  is the heat input efficiency,  $\mu$  denotes friction coefficient,  $P$  is the pressure (Pa) and  $R$  is the tool radius (m). According to the Eq. 2.2, the heat input directly relates with the rotational speed and inversely relates to traverse speed. For the given  $\alpha$ ,  $\mu$ ,  $R$  and  $P$  values, Eq. 2 can be modified as Eq. 2.3.

$$Q \propto \frac{\omega}{v} \dots\dots\dots (2.3)$$

Chen and Kovacevic (2003) considered both shoulder as well as probe radius and proposed that rate of heat generation over the entire interface is given by Eq. 2.4

$$Q = \frac{2\pi\omega\mu P(R_o^3 - r_o^3)}{3} \dots\dots\dots (2.4)$$

where  $\mu$  is coefficient of friction,  $\omega$  is angular velocity,  $P$  is axial pressure,  $R_o$  is the tool shoulder radius and  $r_o$  is the tool pin radius.

**2.1.1 Effect of tool speeds**

Rotational speed and traverse speed ( $\omega$  and  $v$ ) determine the amount of heat input in the SZ, which in turn affects the microstructure and resultant properties. Lower the heat input, more is the grain refinement and vice-versa, but there must be sufficient heat input to plasticize or soften the material (Moghaddas and Kashani-Bozorg 2013). In surface composite fabrication, higher rotational speed is required for distribution and breaking up of clusters of reinforcement particles. However, high rotational speed affects grain refinement due to high heat input



(Azizieh 2011; Barmouz 2011b). Thus, rotational and traverse speed must be optimized to achieve a defect-free SZ and reduced grain size.

In fabrication of SiC/AZ91 composite, it was reported that an increase in rotational speed leads to an increase in grain size while increase in traverse speeds leads to a decrease in grain size. This was explained by noting that increasing traverse speed leads to a decrease in the time of exposure to the process heat (Asadi 2010). Material flow in SZ enhances with increase in rotational speed. As the rotational speed increases, the alumina particle cluster size in the Al<sub>2</sub>O<sub>3</sub>/AZ31 surface composite also decreased (Asadi 2011). Increased heat input due to high rotational speed increases the grain size but nano-particles of alumina are homogeneously distributed due to shattering effect of rotation. The successful combinations of rotational and traverse speeds reported for surface composites are listed in Table 2.1.

Kurt et al. (2011) showed that increasing rotating tool speed and traverse speed caused a more uniform distribution of SiC particles in AA1050 alloy surface composite. However, at very high transverse speeds, the surface composite layer was weakly bonded with the aluminum alloy substrate. Khayyamin et al. (2013) used traverses speeds of 20, 40 and 63 mm min<sup>-1</sup> in fabrication of SiO<sub>2</sub>/AZ91 nano-composite. They observed that the increase in traverse speed refined the grain size in the SZ and resulted in an increase in hardness.

Morisada et al. (2006a) investigated the role of traverse speed in fabrication of MWCNTs reinforced AZ31 alloy surface composites. The tool rotating speed was kept constant at 1500 rpm and the travel speed was varied from 25 to 100 mm/min. At traverse speed of 100mm/min, the MWCNTs were not dispersed uniformly and remained entangled. As traverse speed decreased to 25 mm/min, an improved dispersion of the MWCNTs was achieved without aggregated MWCNTs. This was attributed to a more suitable viscosity in the AZ31 matrix at a lower traverse speed. Shahraki et al. (2013) observed that the distribution of ZrO<sub>2</sub> nano-particles in the SZ of AA5083 alloy was not uniform at low rotational speeds or high traverse speeds. A combination of low rotational speed and high traverse speed results in poor plastic flow of the material, poor distribution of particles, and formation of porosities. Further, at low rotational speeds, the amount of heat produced is not sufficient for the material to become soft enough to attain high traverse speeds.

**Table 2.1:** Successful combination of rotational and traverse speeds for surface composite fabrication

Surface composite	Rotational speed (rpm)	Traverse speed (mm/min.)	Ref.
(SiC+MoS <sub>2</sub> )/A356	1600	50	Alidokht et al.(2011)
SiC/AZ91	900	63	Asadi et al.(2010)
Al <sub>2</sub> O <sub>3</sub> /AZ31	800	45	Azizieh et al.(2011)
SiC/Cu	900	40	Barmouz et al.(2011a)
Nano-clay/Polymer	900	160	Barmouz et al.(2011c)
TiC/Al	1000	60	Bauri et al.(2011)
SiC/AA5052	1120	80	Dolatkhah et al.(2012)
(SiC + Al <sub>2</sub> O <sub>3</sub> )/AA1050	1500	100	Mahmoud et al.(2009b)
Al <sub>2</sub> O <sub>3</sub> /AZ91	1600	31.5	Faraji et al.(2011)
HA/Ti-6Al-4V	250	16	Farnoush et al.(2013)
TiC/Steel	1120	31.5	Ghasemi-Kahrizsangi and Kashani-Bozorg (2012)
SiO <sub>2</sub> /AZ91	1250	63	Khayyamin et al.(2013)
SiC/AA1050	1000	15	Kurt et al.(2011)
MWCNT/AA1016	950	30	Q. Liu et al.(2013)
Ni/AA1100	1180	60	Qian et al.(2012)
(TiC + B <sub>4</sub> C)/AA6360	1600	60	Rejil et al.(2012)
SiC/AA6061	1600	40	Salehi et al.(2012)
B <sub>4</sub> C/Cu	1000	40	Sathiskumar et al.(2013)
SiC/Ti	800	45	Shamsipur et al.(2011)
(SiC+MoS <sub>2</sub> )/AA5083	1250	50	Soleymani et al.(2012)
Al <sub>2</sub> O <sub>3</sub> /AA2024	800	25	Zahmatkesh and Enayati (2010)
Al <sub>2</sub> O <sub>3</sub> /AA6082	1000	135	Shafiei-Zarghani et al.(2009)
Cu/AA5083	750	25	Zohoor et al.(2012)

In fabrication of in-situ surface composites, the temperature and duration of high temperature exposure are decisive parameters for the chemical reactions which are dependent on rotational and traverse speed. Lower rotational speed provides less amount of heat and high traverse speed reduces the duration of high temperature exposure. Chen et al. (2009) opted for lower rotational speed of 500 rpm in the fabrication of in-situ composites from Al-CeO<sub>2</sub> system due to exothermic reaction. A lower traversing speed resulted in a finer and uniform size of in-situ formed particles due to increase in the stirring period. High traverse speed provides less strength which can be related to the relatively larger size and lower amount of in-situ formed

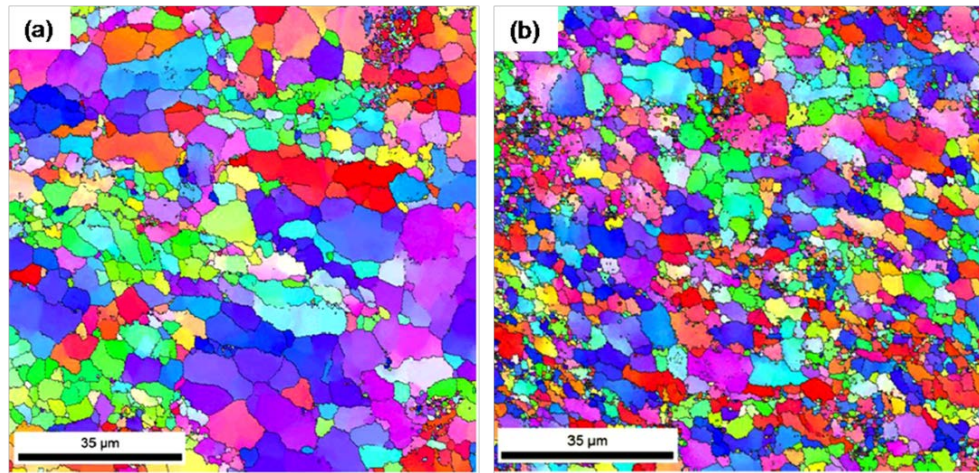
particles. This was attributed to the shorter reaction time and lower reaction temperature associated with a higher tool traversing speed. Zhang et al. (2014) demonstrated that the effect of traverse speed is more significant than rotational speed in the fabrication of in-situ surface composites in Al-TiO<sub>2</sub> system. At a relatively high traverse speed, only partial Al-TiO<sub>2</sub> reaction took place due to lower temperatures and smaller strains in the SZ. The number of Al<sub>3</sub>Ti and Al<sub>2</sub>O<sub>3</sub> particles increased with decreasing traverse speed. On the other hand, rotational speed caused little influence on the size and number of particles. The lower traverse speed resulted in increased temperature which aided diffusion and also increased the stirring time. Similarly, You et al. (2013a) reported that chemical reaction in Al-SiO<sub>2</sub> system was enhanced by reducing the tool traverse speed as it provides longer processing time.

Barmouz et al. (2011a) showed that effect of traverse speed on grain size was reversed in the fabrication of Cu/SiC surface composites as compared to FSP of the material. The SiC particles tend to agglomerate in the SZ on increasing traverse speed. As traverse speed decreased, the grain size decreased in composite, whereas in FSP of Cu without SiC particles grain size increased with the decrease in traverse speed because of increase in heat input. This may be attributed to the uniform dispersion of SiC particles in lower traverse speeds which enhance the pinning effect of SiC particles in the SZ. Salehi et al. (2012) applied Taguchi design approach to determine the factors which influenced ultimate tensile strength (UTS) of AA6061/SiC nano-composites produced by FSP. It was found that rotational speed is the most influential process parameter with 43.70% contribution followed by transverse speed 33.79%, pin profile 11.22% and tool penetration depth 4.21% respectively.

### **2.1.2 Effect of multiple passes**

Clustering of reinforcement particles is a major issue in composite fabrication as it adversely affects the strength of composites. Clustering is more pronounced in nano-sized reinforcements (Sharifitabar 2011). Multi-pass FSP leads to a reduction in size of cluster and uniform distribution of reinforcement particles and thus decreases the grain size of matrix. In FSPed surface composite, the reinforcement particle distribution mainly depends on number of FSP passes (Zohoor 2012). The electron backscattered (EBSD) images of TiC/aluminum in-situ composite, (Fig. 2.2 a, b) necessarily indicate the influence of number of FSP passes on grain refinement. This can be attributed to the higher grain boundary area available after each FSP pass as grain boundaries and interfaces between the particles and the matrix are sources of dislocations. The deformation during subsequent FSP pass generates more dislocations from

these sources, while high stacking fault energy (SFE) of aluminum leads to dynamic recovery and formation of low angle sub-grain boundaries (Bauri 2011).



**Fig. 2.2:** Effect of passes on refinement of grains as indicated by EBSD images of the Al-TiC in-situ composite subjected to (a) single and (b) double pass FSP (Bauri 2011)

In  $\text{SiO}_2/\text{AZ61}$  nano-composites fabrication, Lee et al. (2006) observed that the particles cluster size ranged from 0.1 to 3  $\mu\text{m}$  after one pass of FSP. After four passes of FSP, the cluster size reduced to 150 nm and grain size decreased to 0.8  $\mu\text{m}$ . The YS increased to 225 MPa in nano-composite layer, as compared to 140 MPa in as-received AZ61. In  $\text{Al}_2\text{O}_3/\text{AZ91}$  surface nano-composite fabrication, Asadi et al. (2011) stated that the  $\text{Al}_2\text{O}_3$  cluster size in surface composite decreased to about 500 nm after six passes of FSP as compared to cluster size of 7  $\mu\text{m}$  after one pass of FSP. The UTS of the composite after eight passes increased to 244 MPa, as compared to 128 MPa of as received alloy. Similarly, Sharifitabar et al. (2011) observed the particle clusters of mean size of 650 nm in  $\text{Al}_2\text{O}_3/\text{AA5052}$  surface nano-composite after one pass FSP. After four passes of FSP, the mean cluster size reduced to 70 nm, and showed improvement in YS and UTS of the composite. Barmouz and Givi (2011b) showed that after one pass of FSP the bonding between SiC particles and Cu matrix was weak and the SiC particles were surrounded by pores. Formation of pores increased the porosity of composite to 19% as compared to 2.9% as that of matrix. The porosity content decreased on increasing the number of passes. After eight passes of FSP, the porosity of the composite reduced to 5% due to better interfacial bonding.

The in-situ reactions in the fabrication of surface composite by FSP are highly dependent on heat generated and duration of process (Qian 2012). In fabrication of nickel powder reinforced AA1100 alloy surface composite, Qian et al. (2012) observed that formation of  $\text{Al}_3\text{Ni}$  in-situ particles increased with increase in the number of passes. The increased number of passes enhanced the in-situ reaction owing to increase in processing time. By multiple-passes, the contact area of Al-Ni interface increased due to break-up of the original Ni particles. After six passes, the uniform dispersion of  $\text{Al}_3\text{Ni}$  particles in the composites resulted in 271% and 187% increase in the hardness and UTS of the composites, respectively. In surface composites fabrication, increasing the number of FSP passes leads to a better distribution of reinforcement particles in the matrix, finer grains, higher hardness, strength and elongation (Asadi 2011).

### **2.1.3 Direction of tool rotation**

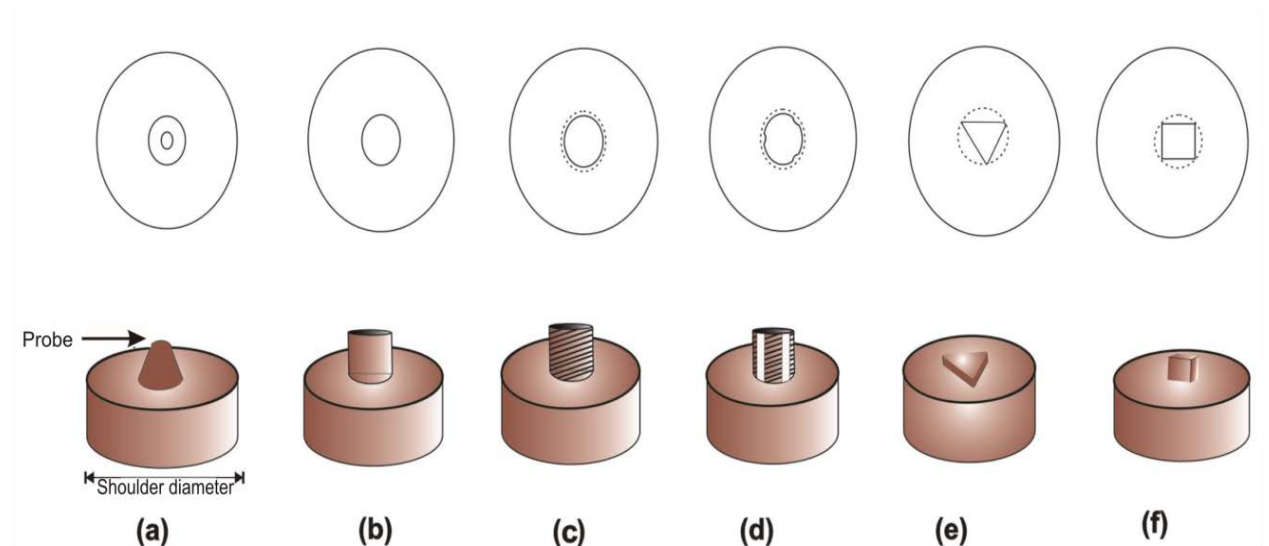
In surface composites, microstructural inhomogeneity has been observed as particle segregation with banded structure in the SZ region. Guo et al. (2014) showed that in nano-sized  $\text{Al}_2\text{O}_3$  reinforced in AA6061 alloy by FSP the particle distribution remained non-uniform after two passes of FSP. The nano  $\text{Al}_2\text{O}_3$  particles tend to form macro-bands, with the areas between those bands are free of particles. (Dolatkhan 2012) observed that nano SiC particles tend to migrate towards advancing side due to asymmetric material flow pattern in FSP of 5052 Al alloy. The microstructural inhomogeneity in FSP can be minimized by changing the direction of rotation of tool after each pass. Asadi et al. (2012) investigated the role of tool direction microstructure and mechanical properties of FSPed AZ91. Results showed that a more homogeneous microstructure can be obtained by changing rotational direction (RD) of tool. Reversing the RD decreases the difference between the advancing side (AS) and the retreating side (RS) hardness values as the microstructural homogeneity is increased. Similarly, Rejil et al. (2012) have applied two passes in opposite directions to achieve better distribution of ceramic particles in fabrication of  $(\text{TiC}+\text{B}_4\text{C})/\text{AA6360}$  hybrid surface composite layer.

Izadi and Gerlich (2012) found that a layer of unreinforced material (flow arm) transferred from the retreating to the advancing side after two passes in the fabrication of MWCNT/AA5059 alloy surface composites. A third pass was performed with the tool rotation reversed to suppress the formation of the flow arm and homogenize the distribution of reinforcing material. Mahmoud et al. (2009b) observed a difference in reinforcement density in the SZ of  $(\text{SiC} + \text{Al}_2\text{O}_3)/\text{AA1050}$  hybrid surface composites. After single pass, there was an increase in number of particles on the top portion of AS while RS and the central top portions

were observed with less amount of reinforcement particles. The reinforcement density on the advancing side became almost similar to that on the retreating side after three passes with opposite direction of tool rotation in the second pass.

#### 2.1.4 Tool geometry

The tool geometry is an important aspect as it affects the processed zone formation (Kumar 2011). Various tool probe geometries like square, triangular, cylindrical, threaded, conical etc. have been adopted for surface composite fabrication (Fig. 2.3). Threaded cylindrical, square and triangular probe profiles have been used more extensively. The probe outer surfaces can also have different shapes and features including threads, flats or flutes. Thread-less probes are suitable for processing of harder alloys or metal matrix composites as the threaded features can be easily worn away.



**Fig. 2.3:** The tool probe geometry of commonly used tools in FSP (a) conical round bottom probe (b) columnar probe (c) threaded columnar probe (d) threaded columnar probe with flutes (e) triangular probe (f) square probe

Elangovan et al. (2007) observed in FSW of AA6061 alloy that a square pin profile produces more pulse/sec as compared to triangular pin profile and no such pulsating action was observed in cylindrical, tapered and threaded pin profiles. The square pin profile produces 80 pulses per second ( $\text{pulses/s} = \text{rotational speed in seconds} \times \text{number of flat faces}$ ) and triangular pin profile produces 60 pulses per second at the tool rotational speed of 1200 rpm. More pulsating action generated by square pin profile can produce smaller grains with uniformly distributed fine

precipitates which in turn yield higher strength and hardness. However, Faraji et al. (2011) observed that the grain size and particle size in the specimen produced by the triangular tool is smaller than that of square tool in the fabrication  $\text{Al}_2\text{O}_3$  reinforced as-cast magnesium alloy AZ91 composite. They attributed this to the sharp edges of triangular pin which results in better stirring of the material. Mahmoud et al. (2009a) showed that in surface composite fabrication of SiC reinforced aluminum alloy, the square probe resulted in more homogeneous distribution of SiC particles than the cylindrical and triangular shape tools. The tool wear rate of flat faces (square and triangular) probes was higher than that of circular probe. It was also observed that sharp corners of the probe were deteriorated rapidly and the tool worn material reacted with the aluminum to form fine iron aluminides.

Padmanaban and Balasubramanian (2009) found that a pin with a screw thread generates more heat than the pin without a screw thread in FSW of AZ31 alloy. More heat input can improve the material flow in the SZ. Moreover, the screw threaded probe exerts an extra downward force that will be useful to accelerate the flow of the plasticized material. The effect of tool shoulder (D) to probe diameter (d) ratio i.e. D/d was also studied, and a D/d ratio of 3 was found to be better in producing defect-free SZ. Similarly, Azizieh et al. (2011) in fabrication of  $\text{Al}_2\text{O}_3$ /AZ31 nano-composite found that threaded columnar probe tool produced composite without defects as compared to non-threaded and three-fluted columnar probe tools due to better material flow. Yu et al. (2012) developed a three-dimensional transient computational fluid dynamics (CFD) model to investigate the material flow and heat transfer during FSP with the threaded/non-threaded pin in AZ31B magnesium alloy. A comparison of the threaded and non-threaded models showed that the thread strongly influenced the temperature distribution, material flow velocity and strain rate near the tool pin within the SZ.

### **2.1.5 Tool material and wear**

In FSP, high temperature and load experienced by tool results in significant material damage of tool. Tool wear is the most critical issue in fabrication of surface composites due to hard reinforcement particles. Tool materials generally used for light alloys are various hard steels like H13 steel, whereas tungsten based alloys, cermets (WC-Co) and Poly cubic boron nitride (pcBN) are used for FSP of harder materials. Some other tool materials including iridium-rhenium (Ir-Re), tungsten-rhenium (W-Re), cobalt (Co) alloys and tungsten carbide (WC) are also successfully employed. pcBN is preferred friction stir tool material for hard alloys such as steels and titanium alloys due to its high mechanical and thermal performance. However, high cost and low fracture toughness of pcBN requires immediate attention to develop cost effective

and durable tools (Rai 2011). Some common materials used for surface composite fabrication and processing of various alloys are given in Table 2.2.

**Table 2.2:** Tool materials utilized for surface composite fabrication and processing of various alloys

Material	Tool material	Ref.
Nano-clay/HDPE polymer	H13 tool steel	Barmouz et al. (2011b)
Titanium alloy	(Al, Cr) N coating on W-Co	Batalha et al. (2012)
SiC/AA5052	H13 tool Steel	Dolatkah et al. (2012)
Al <sub>2</sub> O <sub>3</sub> /AZ91	H13 tool steel	Faraji et al. (2011)
TiC/steel	WC	Ghasemi-Kahrizsangi and Kashani-Bozorg (2012)
CA6NM steel	WC	Grewal et al. (2013)
SiO <sub>2</sub> /AZ91	H13 tool steel	Khayyamin et al. (2013)
SiC/AA1050	AISI 1050 steel	Kurt et al. (2011)
Austenitic stainless steel	B <sub>4</sub> N hard faced on Inconel 738 alloy	Lakshminarayanan et al. (2014)
TiC/Ti-6Al-4V	WC-13%Co	Li et al. (2013)
Nitinol	pcBN and W-Re	London et al. (2005)
Iron	pcBN	Mironov et al. (2008)
SUS304 stainless steel	Ir-Re	Miyazawa et al. (2011)
WC-CrC-Ni/steel	WC-Co	Morisada et al. (2010)
Steel and titanium	Co-based alloy	Sato et al. (2011)
Ti-6Al-4V	W-1%La <sub>2</sub> O <sub>3</sub>	Su et al.(2013)
NiAl bronze	Densimet(W-7%Ni, Fe)	Swaminathan et al.(2010)
Steel	W-20% Re-10%HfC	Thompson and Babu (2010)
Nickel	Tool steel	Xue et al. (2014)

Ghasemi-Kahrizsangi and Kashani-Bozorg (2012) observed that tungsten carbide (WC) tool utilized for fabricating TiC/steel surface composite showed significant tool wear (20% reduction in dimensions) just after 400 mm of processing. Farias et al. (2013) reported that the



severe tool wear caused loss of surface quality and inclusions of tool material (WC) inside the work-piece in FSW of Ti-6Al-4V. They found adhesion of the work-piece material on the tool pin and shoulder surface, and diffusion of tool and the work-piece materials constituents. Morisada et al. (2010) successfully FSPed thermally sprayed cemented carbide (WC-CrC-Ni) layer on SKD61 steel by using a sintered cemented carbide (WC-Co) tool. After processing the defects in the cemented carbide layer disappeared and the hardness of the cemented carbide layer increased to ~2000 H<sub>V</sub>, which was nearly 1.5 times higher than that of the as-sprayed cemented carbide layer. Swaminathan et al. (2009) utilized tungsten based alloy Densimet (W-7% Ni, Fe) tool for FSP of NiAl bronze without any significant wear of tool. Grewal et al. (2013) FSPed hydroturbine steel (13Cr-4Ni) by using a WC tool and no wear of tool material was observed. Feng et al. (2008) indicated that a deleterious phase of Cu<sub>2</sub>FeAl<sub>7</sub> was formed due to wear of steel tool in FSW of SiC/AA2009 bulk composite. Even slight wear of tool resulted in a decrease in strength of the friction stir welded composite after T4 condition due to formation of the Cu<sub>2</sub>FeAl<sub>7</sub>. London et al. (2005) used tools made of pcBN and tungsten-rhenium alloy (W-Re) for FSP of Nitinol (49.2 % Ti, 50.8 % Ni). No noticeable wear of the tools was observed.

**Xue et al. (2014)** successfully FSPed nickel (Ni) by utilizing the tool made of common tool steel (M42) using additional water cooling. The FSP of Ni exhibited defect-free processing surface and no obvious tool abrasion was observed. However, when the FSP process was performed without water cooling, the tool failed quickly after the shoulder touched the work-piece due to greatly increased temperature. The tool wear occurred more on the specific locations in FSW of Al-Si alloy matrix composite reinforced with 30 vol. % of SiC by the threaded tool of WC-Co hard alloy (**Liu 2005**). It was observed that at lower welding speed the wear rate of tool is more as compared to higher welding speed. The wear of the pin was different at different lengths of the pin, and the maximum wear was found at about one-third of pin length from the pin root. Prado et al. (2003) reported that in FSW of AA 6061-20%SiC metal matrix composite (MMC) the wear of tool steel threaded pin tool changed the tool into a smooth self-optimized shape (without threads). They observed that the worn tool or self-optimized shape with no threads resulted in homogenous and integral welds without further significant tool wear. These observations suggest that tool wear can be greatly reduced even for MMCs when using the optimized tool shape.

Rai et al. (2011) pointed out that the tungsten, molybdenum, and iridium are suitable options of tool materials as they possess high hardness, low reactivity with oxygen and high temperature

strength. These tool properties can be enhanced further by the addition of alloying elements or coating the tool with a hard and wear resistant material. Tool wear in the FSW of titanium and high strength steel was minimized by the use of tungsten-rhenium (W-25%Re) alloys, but high tool costs due to the rare rhenium component limits its applicability. Thompson and Babu (2010) studied the tool life of W-1% La<sub>2</sub>O<sub>3</sub>, W-25%Re and W-20%Re-10%HfC for joining high strength steel. Tool material with HfC was found to be more resistant to tool degradation as HfC particles effectively prevent softening of the tool material and supports the surrounding W-Re grains.

Miyazawa et al. (2011) investigated iridium alloy based tool material for FSW of SUS304 stainless steel with addition of various high melting point metals. A higher softening temperature (recrystallization temperature) for Ir-1 at% Re was observed than any other alloy. Additives such as Ta, W, Nb and Mo lower the melting points of the Ir alloys. Further, high temperature hardness and compressive strength increase with increasing Re concentration. The Ir-10 at% Re tool material exhibits less wear compared to other tool materials. Buffa et al. (2012) studied tungsten based alloys for FSW of Ti-6Al-4V alloy. They used tool material of WC-4.2%Co, WC-12%Co and a W-25%Re alloy in this study. The tool made from WC-4.2% Co exhibited high hardness, but the tool failed very early by fracture. In WC-12%Co tool, deformation was observed in the shoulder and at the pin, together with adhesive wear degradation. W-25%Re tool showed the lowest wear degradation and a longer life. Sato et al. (2011) developed a Co-based tool alloy for FSW of high strength materials such as steel and titanium. The Co-based tool was strengthened by precipitating intermetallic Co<sub>3</sub>(Al, W) at high temperatures. In FSW of Ti-6Al-4V alloy with this tool, the tool wear was low and the good quality weld was obtained.

The hard coatings processed by physical vapor deposition and chemical vapor deposition techniques are efficient means to increase the durability of tools made from cemented tungsten carbide. The hard material coated layer improves wear resistance, reduces adhesion between the tool material and work piece, and acts as a diffusion barrier (Batalha 2012). Batalha et al. (2012) evaluated the wear performance of a physical vapor deposition coating of (Al, Cr) N material on cemented carbide (WC-Co) tool for FSW of Ti alloy sheets. The coating was not found on the tool after FSW and also tool material exhibited wear. Lakshminarayanan et al. (2014) studied the effect of various refractory ceramic based composite coatings on the Inconel 738 alloy tool for FSW of AISI 304 grade austenitic stainless steel. The impact and wear resistance of 60% B<sub>4</sub>N hard faced tool by plasma transferred arc were superior compared to other hard faced tools, which resulted in debris free weld nugget.

## 2.2 Effect of cooling

Nano-sized grains can be achieved by proper cooling arrangements. Cooling during FSP also serves the additional function of reducing tool wear (Xue 2014). In a study of FSPed interstitial free (IF) steel, FSP followed by quenching resulted in formation of a nano-grain layer of 150  $\mu\text{m}$  thickness and 50-100 nm average grain size. The post-FSP cooling resulted in effective control of grain size by arresting grain growth (Chabok and Dehghani 2012). The grain size of AA6061-T6 reduced from 50  $\mu\text{m}$  to 100-200 nm by submerged friction stir processing (SFSP) (Hofmann and Vecchio 2005). SFSP was performed in a tank filled with water at a high traverse speed to refine grains to nano-regime. The faster cooling rate achieved through SFSP is believed to retard grain growth.

While few studies relating to use of coolant during FSP of various alloys are reported, investigations on coolant application in fabrication of surface composites are rarely available. Najafi et al. (2008) observed grain size of 800 nm in SiC/AZ31 surface composite fabricated by single FSP pass using a coolant mixture of methanol and dry ice. The grain size of 1  $\mu\text{m}$  was observed in FSPed AZ31 without SiC particles. AZ91 based hybrid composites with  $\text{Al}_2\text{O}_3$  and TiC as reinforcements showed increased hardness nearly by 100 %. Cooling was achieved by circulating coolant below the workpiece. While FSPed composite without cooling showed grain size of nearly 5.1  $\mu\text{m}$ , FSP using under surface cooling resulted in an average grain size of 2.4  $\mu\text{m}$  (Arora 2012). Zhang et al. (2011) applied two additional passes in flowing water on FSPed in-situ  $\text{Al}_3\text{Ti}$  and  $\text{Al}_2\text{O}_3$  nano-particles reinforced Al composites. Four passes were applied in air and then two passes were applied in flowing water. They found that the average grain size was decreased to 602 nm after additional passes by application of water. Initially, the average grain size after four passes of FSP in air was 1285 nm. Thus, the effect of coolant on grain refinement in composites is limited probably because of the fact that reinforcement also plays a major role in restricting grain growth.

Sharifitabar et al. (2011) did not cool the sample to room temperature after each FSP pass in the fabrication of  $\text{Al}_2\text{O}_3$ /AA5052 surface nano-composite. A uniform distribution of particles as well as reduction of cluster size was achieved, but grain growth also accompanied. The sample was heated in the first FSP pass and in the subsequent passes, sample was in preheated condition. Preheated sample was softer which allowed more stirring action that caused better distribution of particles and cluster size reduction. The average grain size of the matrix was 940 nm which was higher as compared to that reported in similar studies but cluster size reduced.

Asadi et al. (2012) showed that water coolant favored the formation of oxides on the surface of AZ91 during FSP and these oxides dispersed into SZ after subsequent passes.

### 2.3 Microstructural modification

Microstructural refinement is an important feature of FSP as the grain refinement can be achieved up to nano scale. However, most commonly grain size reported in literature is < 10 $\mu$ m. External or in process cooling was utilized in FSP to refine grain size up to nano size. The extent of grain refinement achieved in surface composites and various alloys by FSP is shown in Table 2.3. As shown in table the grain size was significantly reduced up to 500 times in submerged friction stir processing (SFSP) performed in water and 600 times in thin plate of Interstitial Free (IF) steel. However, most commonly grain size reduction ranges from 20 to 50 times.

Microstructural refinement via FSP not only limited to grain size reduction but it extends to refinement and homogeneous distribution of second phase particles and breakup of reinforcement particles clusters. Rao et al. (2009) modified the cast microstructure of hypereutectic Al-30 wt. % Si alloy by FSP. They found that stirring action of the tool during FSP reduces the size of undesirable coarse silicon particles, eliminates porosities and homogenizes the cast microstructure.

**Table 2.3:** Grain refinement obtained in surface composites and alloys by FSP

Material	Grain size ( $\mu$ m)		Size reduction	Ref.
	Base material	After FSP		
AA7075	-	100-400nm	-	Su et al. (2005)
AZ31/Al <sub>2</sub> O <sub>3</sub>	70	0.35	200	Azizieh et al. (2011)
AZ91	150	3	50	Faraji et al. (2011)
AZ91/SiC	150	7.17	21	Asadi et al. (2010)
AZ91	140	8.27	17	Khayyamin et al. (2013)
IF steel	60	50-100 nm	600	Chabok and Dehghani (2013)

AA 6061-T6	50	100-200 nm	500	Hofmann and Vecchio (2005)
AZ61	75	<300 nm	250	Xing-hao and Bao-lin (2008)
A206 alloy	210	3.5	60	Kapoor et al. (2013)
AA 5052/nano SiC	243	0.9	270	Dolatkhah et al. (2012)
AZ31/SiC	79.1	6.0	14	Morisada et al. (2006)
AA 5083/ (SiC+ MoS <sub>2</sub> )	45	16	3	Soleymani et al. (2012)

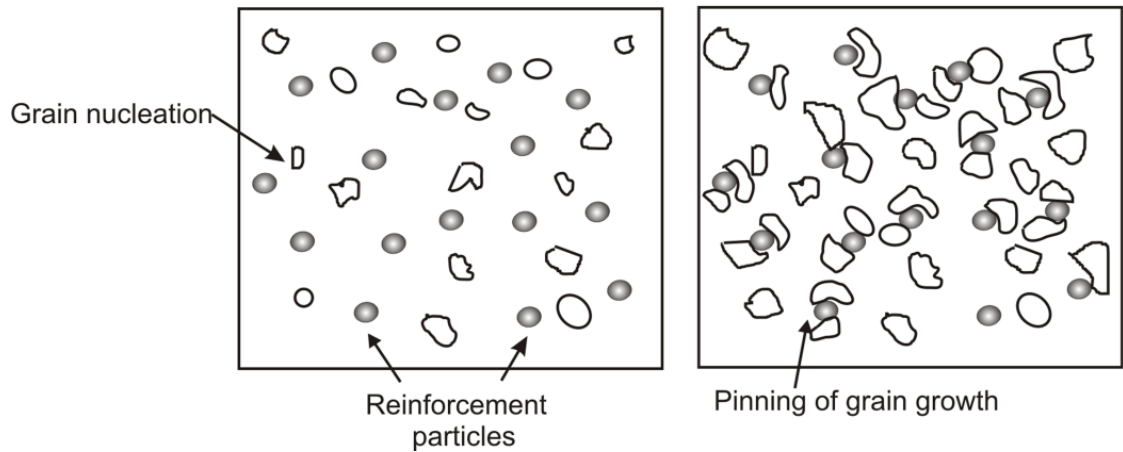
Moreover, FSP caused not only reduction in the average grain size but also a tighter distribution of the grain size. FSP of ECAP sheet also resulted into increase in HAGBs from 15% in ECAP condition to 71% in FSP condition. Mironov et al. (2008) conducted FSP on Iron and showed with the aid of EBSD and SEM that development of the grain structure is a complex process driven mainly by grain subdivision, but also involving the geometric effects of strain and local grain-boundary migration. Argade et al. (2012) studied the influence of microstructural scale on stress corrosion cracking (SCC) behavior of magnesium alloy AZ31. Higher SCC susceptibility is observed for refined microstructures as compared to base material. The finer grain size of FSPed samples showed higher susceptibility to SCC. For the FSP refined microstructures the combination of stress and corrosive medium is observed to accelerate the stress corrosion attack with lower time to failure as compared to the starting coarse grained microstructure.

**2.4 Effect of reinforcement particle on grain refinement**

Surface composites show the synergistic effect of grain refinement by FSP and reinforcement particles. Zener pinning dictates that in the presence of dispersed second phase particles, the movement of grain boundaries that are migrating due to recrystallization and grain growth may be pinned by the small second phase particles (Rohrer, 2010). The Zener limiting grain size ( $d_z$ ) expressed in Eq. 2.5 below:

$$d_z = 4r/3V_f \dots\dots\dots (2.5)$$

where,  $r$  and  $V_f$  are the radius and volume fraction of second phase particles, respectively. According to Eq. 5, the grain refinement by reinforcement particles increases with the decrease in particle size and increase in volume fraction of the particles. The schematic representation of pinning by reinforcement particles is shown in Fig. 2.4. Grain refinement by pinning of reinforcement particles is shown in Table 2.4.



**Fig. 2.4:** Schematic of pinning of the grain growth by reinforcement particles

Shamsipur et al. (2011) found that nano-sized SiC particle reinforcement in titanium refined grains up to average size of 400 nm, as compared to 4  $\mu\text{m}$  without SiC particles. Morisada et al. (2006b) also observed reduction of grain size in SZ of AZ31 alloy reinforced with SiC particles to 2  $\mu\text{m}$  size. Without SiC particles the grain refinement was limited to 5  $\mu\text{m}$  for the same processing conditions. The SiC particles also restrict abnormal grain growth. As depicted in this study, the FSPed sample without SiC particles shows abnormal grain growth (AGG) above 573 K whereas the FSPed sample with SiC particles resists AGG up to 673 K due to pinning effect of SiC particles. Sathiskumar et al. (2013) reported that in Cu/B<sub>4</sub>C surface composite, the SZ area with B<sub>4</sub>C particles was reduced as compared to the SZ area in FSP of copper without particles. The area of the SZ without particles was found to be 44 mm<sup>2</sup> and reduced to 24 mm<sup>2</sup> at 24 vol. % of B<sub>4</sub>C particles. SZ area reduction was due to resistance offered to the flow of plasticized copper by non-deformable B<sub>4</sub>C particles. Surface composites reinforced with different carbon nano-structures exhibited significant reduction in grain growth during FSP.

**Table 2.4:** Grain refinement of matrix by the pinning effect of reinforcement particles

Surface composite	Particle size (nm)	Grain Size ( $\mu\text{m}$ )			Ref.
		As received	FSP without particles	FSP with particles	
Copper	5000	40	10	3.2	Barmouz et al. (2011)
Copper	30	40	10	0.8	Barmouz et al. (2011)
AA5052	5000	243	16.3	2.2	Dolatkhah et al.(2012)
AA5052	50	243	16.3	0.9	Dolatkhah et al.(2012)

AZ31	1000	79.1	12.9	6	Morisada et al. (2006)
AZ91	30	150	7.27	5.94	Faraji et al. (2011)
Al <sub>2</sub> O <sub>3</sub> /AA6082	50	120	2	0.66	Shafiei-Zarghani et al. (2009)
TiC/Mild steel	70	15	5	0.60	Ghasemi-Kahrizsangi and Kashani-Bozorg (2012)
CNT/AA2009	10-30	-	4	0.8	Liu et al. (2012)
SiC/Ti	50	75	4	0.4	Shamsipur et al. (2011)
SiO <sub>2</sub> /AZ61	20	75	7	0.8	Lee et al.(2006)
SiC/AZ91	5000	150	-	7.1	Asadi et al. (2010)
Al <sub>2</sub> O <sub>3</sub> /AZ31	35	70	8.1	3.4	Azizieh et al. (2011)
(Al <sub>3</sub> Ti + Al <sub>2</sub> O <sub>3</sub> )/Al	150	-	8.3	1.2	Zhang et al. (2012)
TiO <sub>2</sub> /Al-Mg alloy	30	50	10	2	Khodabakhshi et al. (2014)
ZrO <sub>2</sub> /AZ31	20	70	6	2	Chang et al. (2006)
CNT/AA2009	10-30	-	4	0.8	Liu et al. (2012)

Morisada et al. (2006c) reported ~100 nm size grains for AZ31/C<sub>60</sub> surface composite fabricated by FSP. The C<sub>60</sub> molecule was uniformly dispersed in the matrix. The FSP and pinning effect refines grain size which improves hardness up to three times as compared to the base alloy. Increasing the volume fraction and employing multi-pass FSP enhanced the pinning effect (Liu 2012).

Shafiei-Zarghani et al. (2009) related the experimentally observed grain size with the Zener limiting grain size ( $d_z$ ) in AA6082/Al<sub>2</sub>O<sub>3</sub> nano-surface composites fabricated via FSP. The grain size in the composite was found to be higher than  $d_z$  as a certain level of local clustering is inevitable, and also not all nano-particles can effectively pin the grain boundary migration. Further, the difference in the composite grain size and  $d_z$  was much higher in single pass due to non-uniform distribution of nano-particles. However, Ghasemi-Kahrizsangi and Kashani-Bozorg (2012) found steel/TiC nano-composite grain size to be consistent with the  $d_z$ . In steel/TiC surface composite, the TiC nano-sized particle of 70 nm refined grains to 600 nm as compared to grain size of 5  $\mu$ m without particle addition. Asadi et al. (2011) showed the effect of different particles and their distribution behavior on the grain refinement of the AZ91 reinforced with nano-size SiC and Al<sub>2</sub>O<sub>3</sub> particles. The grain size after eight passes of FSP was 800 nm for SiC and 1.3  $\mu$ m for Al<sub>2</sub>O<sub>3</sub> reinforced surface composite. This was attributed to the better wetting behavior and distribution of particles without forming clusters in case of SiC particles.

## 2.5 Strengthening mechanisms

Strengthening mechanisms operative in surface composites are similar to those in bulk metal matrix composites. Lloyd (1994) pointed out the four major strengthening mechanisms in particle reinforced metal matrix composites: Orowan strengthening, grain and sub-grain boundary strengthening (Hall-Petch relationship), strengthening from difference in coefficient of thermal expansion (CTE) between the particles and the matrix, and work hardening resulted from the strain misfit between the particles and the matrix. Similarly, Kim et al. (2013) indicated three major mechanisms for strength enhancement in metal matrix nano-composites (MMNCs): Orowan strengthening, grain refinement, and CTE mismatch strengthening. Sanaty-Zadeh and Rohatgi (2012) experimentally validated the model for magnesium nano-composites reinforced with  $\text{Al}_2\text{O}_3$  and  $\text{Y}_2\text{O}_3$  particles. It was found that Hall-Petch strengthening is the most important factor for strength contribution. The CTE and Orowan strengthening effect contribution to strength increases with an increase in the volume fraction of reinforced ceramic particles.

The enhancement of mechanical properties exhibited by surface composites is shown in Figs. 2.5 and 2.6. Fig. 2.5 shows that the increase in micro-hardness of the surface composites fabricated via FSP. This is attributed to grain refinement and incorporation of reinforcement particles. The increase in strength of surface composites is shown in Fig. 2.6, which highlights the potential of FSP in enhancing the strength. The observed decrease in UTS for SiC/Cu composite was attributed to the non-uniform distribution and agglomeration of SiC particles (Barmouz 2011a).



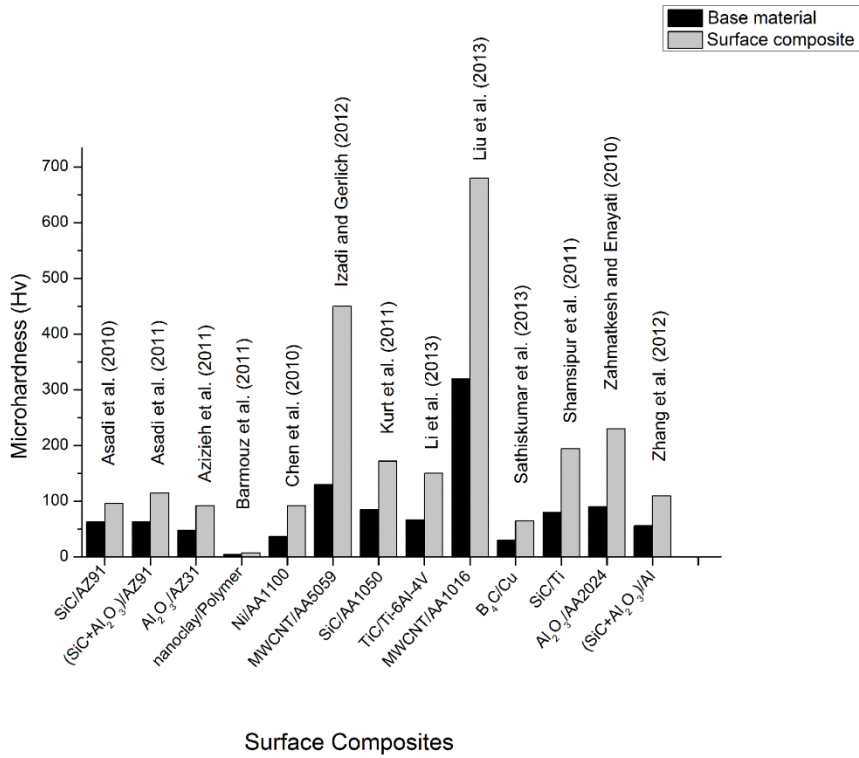


Fig. 2.5: The improvement in micro-hardness of surface composites fabricated via FSP

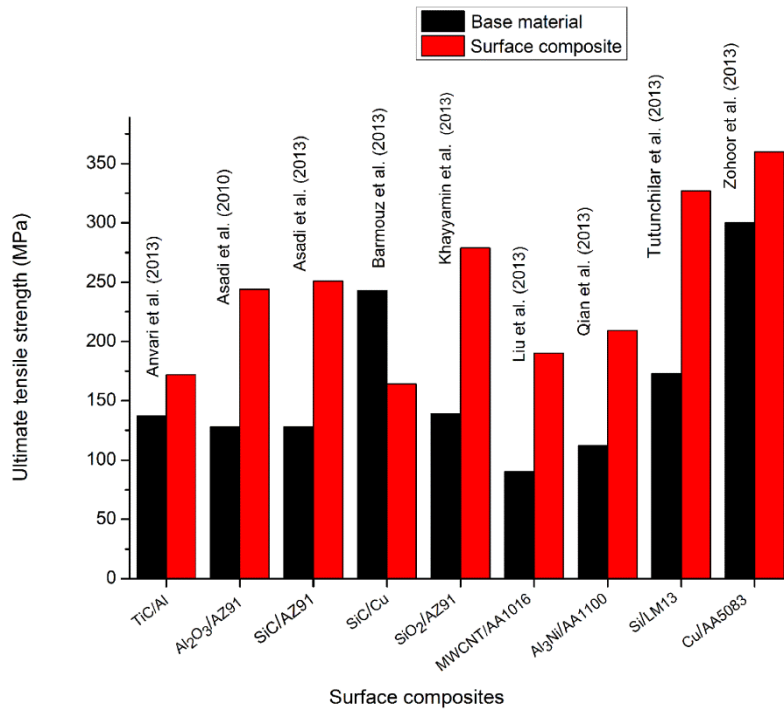


Fig. 2.6: The ultimate tensile strength of surface composites fabricated via FSP

**2.5.1 Strengthening models**

Liu et al. (2012) proposed a model for strengthening in CNT/AA2009 alloy surface composite by considering load bearing and grain refinement strengthening effect. The Orowan effect was not considered in this model due to CNTs dispersion along the grain boundaries. The YS ( $\sigma_c$ ) of the composites with individually dispersed CNTs can be expressed by their model is given in Eq. 2.6:

$$\sigma_c = (\sigma_0 + kd^{-1/2})[V_f(s+4)/4 + (1-V_f)] \dots\dots\dots (2.6)$$

where, k is a constant, d is the average grain size, s is the aspect ratio of the CNTs,  $V_f$  is the volume fraction of the CNTs.

They claimed that predicted results by the Eq.6 were in good agreement with the experimental results. The discrepancies between the experimental and calculated results were below 5% for the CNT/Al alloy composites. They later incorporated the effect of clustering of CNTs in their later model. The clustering reduces the effective volume fraction and also induces the porosity in the composites (Liu 2014a). They proposed a modified equation to estimate the tensile strength of CNT/AA2009 composites as given below in Eq. 2.7:

$$\sigma_L = (\sigma_0 + kd^{-1/2})[(V_f - V_{cluster})(s+4)/4 + (1-(V_f - V_{cluster}))] \exp(-\lambda\theta) \dots\dots\dots (2.7)$$

where,  $\sigma_L$  is the strength of composite with pores,  $V_{cluster}$  is the volume fraction of the CNT clusters,  $\theta$  is the volume fraction of porosity and  $\lambda$  is a constant for material with porosity.

Lee et al. (2011) used modified shear lag model to estimate the YS ( $\sigma_{cy}$ ) of silicon reinforced aluminum composites fabricated by FSP combined with powder metallurgy. They considered the Orowan, Hall Petch and CTE strengthening to estimate the YS according to Eqs. 2.8 and 2.9.

$$\sigma_{cy} = \sigma_{my} (1 + 0.5SV) \dots\dots\dots (2.8)$$

$$\sigma_{my} = \sigma_o + \sigma_{OR} + \sigma_g + \sigma_{CTE} \dots\dots\dots (2.9)$$

where,  $\sigma_{my}$  is the matrix YS, V is the volume fraction of the particles, S is related to aspect ratio, and S=1 for equiaxed particles,  $\sigma_o$  is the initial matrix strength,  $\sigma_{OR}$  is the strength contribution from Orowan strengthening,  $\sigma_g$  is the grain size strengthening and  $\sigma_{CTE}$  is the CTE mismatch strengthening. The estimated results at varying percentage of silicon were overestimated in the range of 10-15% as compared to experimental results.

Guo et al. (2014) demonstrated by using models and experimental results that grain refinement and Orowan strengthening contributed to the strengthening of Al<sub>2</sub>O<sub>3</sub>/AA6061 alloy surface

nano-composites. The estimated contribution of grain refinement and Orowan strengthening showed that Orowan strengthening contribution was nearly four times more as compared to the grain refinement contribution. They used grain refinement contribution to strength and modified Orowan equation, as given in Eqs. 2.10 and 2.11:

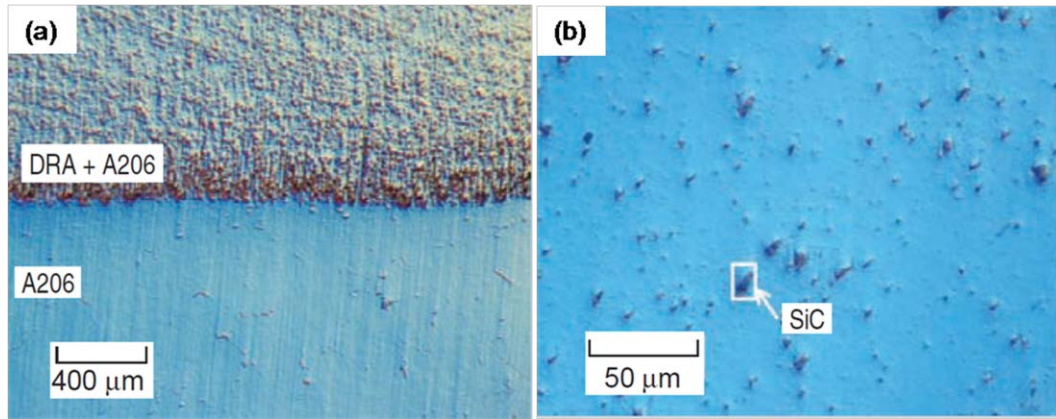
$$\sigma_o = M \frac{0.81 G_m b}{2\pi(1-\nu)^{1/2} \lambda} \ln\left(2\sqrt{2/3} r / r_0\right) \dots\dots\dots (2.10)$$

$$\lambda = \left[ \sqrt{\frac{\pi}{F_v}} - 2 \right] \left( \sqrt{\frac{2}{3}} \right) r \dots\dots\dots (2.11)$$

where M=3 is the Taylor factor for a face centered cubic polycrystal,  $G_m$  is the matrix shear modulus, b is the Burgers vector magnitude,  $\nu$  is Poisson's ratio, r is the radius of particles,  $r_0$  is the dislocation core radius, and  $F_v$  is the volume fraction of particles.

## 2.6 Classification of FSPed surface composites

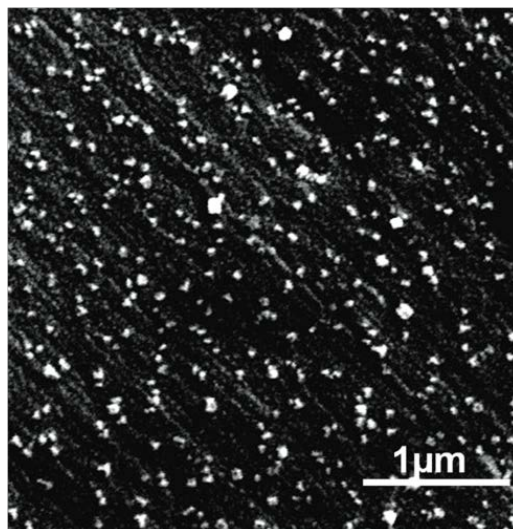
Commonly used reinforcement in fabrication of surface composites are micron or nano size SiC, Al<sub>2</sub>O<sub>3</sub>, B<sub>4</sub>C, TiC etc. and carbon nano-structures (Arora 2011). The surface composites fabricated by FSP route exhibit a good bonding and uniform distribution of reinforcement particles as shown in Fig. 2.7 (a, b). Li et al. (2013) observed reduction in the size of micron size TiC reinforcement particles by FSP in fabrication of TiC/Ti-6Al-4V surface composite. Some of the ~5.5  $\mu$ m size TiC reinforcement was reduced to nano-size after one pass of FSP. Al<sub>2</sub>O<sub>3</sub> reinforcement (30  $\mu$ m, 300 nm and 30 nm) were used in fabricating Al<sub>2</sub>O<sub>3</sub>/AZ91 surface composites by FSP by Faraji et al. (2011). They observed that the FSP with the nano-sized Al<sub>2</sub>O<sub>3</sub> particles was more effective in grain refinement of the AZ91 matrix. Dolatkhah et al. (2012) investigated the effect of micron and nano size SiC particles in fabrication of SiC/AA5052 surface composites. They found that 50 nm sized SiC particles reduced grain size more than two times as compared to 5  $\mu$ m size SiC particles. Incorporation of nano-particles reduced average grain size to 0.9  $\mu$ m, whereas grain size reduction in 5  $\mu$ m size particles limited to 2.2  $\mu$ m.



**Fig. 2.7:** Micrograph of SiC/A206 surface composite fabricated by FSP (a) strong bonding between the composite layer and matrix (b) uniform distribution of reinforced particles in the matrix (Sun and Apelian, 2011)

### 2.6.1 Surface nano-composites

Dispersion of the nano-sized reinforcements in a uniform manner in metal matrix is a major challenge. Nano-particles due to their high surface area tend to agglomerate to reduce their overall energy (Tjong, 2007). Agglomeration induces pores and also increases inter-particle spacing which in turn decreases the strengthening of nano-composites. FSP is a newer technique for fabrication of surface nano-composites and it is advantageous in ease of dispersion and elimination of clusters of nano-particles. The uniform distribution of nano-sized reinforcement particles in steel matrix is shown in Fig. 2.8.



**Fig. 2.8:** SEM micrograph of uniformly distribution nano-size TiC reinforced in steel by FSP (Ghasemi-Kahrizsangi and Kashani-Bozorg, 2012)

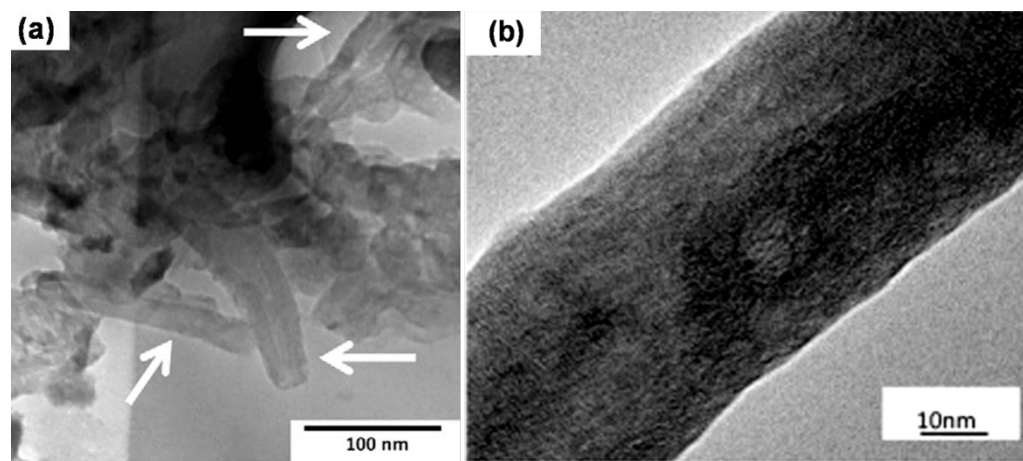
Several studies were reported on nano-surface composite by reinforcing nano-size ceramic particles and carbon nano-tubes (CNTs). Dispersion and distribution of nano-size particles in the surface composite can be successfully achieved after multi-pass FSP. One important feature of surface nano-composites fabricated by FSP is that they are defect free without voids. Also a homogeneous particle distribution is achieved (Liu 2013). This can provide exceptional combinations of strength and ductility in surface nano-composites. Shafiei-Zarghani et al. (2009) showed that  $\text{Al}_2\text{O}_3/\text{AA6082}$  nano-composites can achieve hardness values of  $295\text{H}_\text{V}$  after four pass FSP. The nano-sized  $\text{Al}_2\text{O}_3$  particles also reduced the grain size of the matrix in which some grains were less than 300 nm. The high micro-hardness obtained was attributed to the Orowan mechanism and ultrafine grain size of the aluminum alloy matrix. The surface composite exhibited improved wear resistance as compared to as-received alloy. The mechanism of wear observed was a combination of abrasion and adhesion.

Farnoush et al. (2013) deposited coating of nano-hydroxyapatite (HA) on the Ti-HA surface composite. Firstly, the surface composite layer of CaP-Ti was fabricated via FSP by reinforcing HA powder in Ti-6Al-4V alloy. After FSP, the coating of HA was applied on this surface layer by electrophoretic deposition. Bonding strength was more than twice as compared to HA coating on the as received alloy. Increase in bonding strength was attributed to the Ti-CaP inner layer which reduced the thermal expansion mismatch between Ti alloy and the HA coating. Ratna et al. (2014) observed enhanced corrosion resistance for nano-hydroxyapatite (nHA) reinforced AZ31 magnesium alloy surface composite fabricated by FSP. They found that the AZ31-nHA composite have better corrosion resistance compared to fine grained FSP AZ31 and AZ31 samples due to the combined effect of reduced grain size and incorporated nHA particles.

Barmouz et al. (2011c) fabricated polymer nano-composite by FSP and demonstrated a three-fold increase in hardness value as compared to that exhibited by composite fabricated using conventional mixing in the melt. High density polyethylene (HDPE) and nano-clay composite was fabricated by FSP by placing the nano-clay in the machined groove in the HDPE. The significant increase in the micro hardness values could be attributed to the good dispersion of nano-clay particles on the surface of polymer.

Carbon nanotubes (CNTs) are the ideal reinforcements for fabricating composites because of their extremely high elastic modulus and strength with good thermal and electrical properties (Popov, 2004). The exceptional properties of CNTs can be well harnessed by uniform dispersion in metal matrix with minimum damage to the structure. The good bonding between

carbon nano-structure and matrix alloy is shown in Fig. 2.9 (a, b). The survivability of single-walled carbon nanotubes during FSP in AA7075 alloy matrix was investigated by Johannes et al. (2006). Raman spectroscopy analysis indicated that CNTs survived the thermal and stress cycles involved in FSP with a tool rotation speed of 400 rpm and a traverse speed of 25.4 mm/min. Multiple passes of FSP are required for the uniform distribution of CNTs, but may lead to damage CNTs to a great extent (Izadi and Gerlich, 2012; Liu 2013). In fabrication of AA5059 alloy reinforced with MWCNT, Izadi and Gerlich (2012) showed that MWCNT survived after two passes of FSP. However, the uniform distribution of MWCNTs was achieved by three passes of FSP only. The high shear stresses along with the elevated temperatures in the SZ led to the damage of MWCNT structure. The average micro-hardness of the composite after three passes was increased to more than twice as compared to base alloy. Q. Liu et al. (2013) also observed breakage of MWCNTs due to intense stirring effect in FSP. However, a strong interface between the MWCNTs and matrix without intermediate compounds or nano-pores was observed. Regions of ultrafine grains (50-100 nm) were also detected in the composites, which were induced by severe deformation and the dynamic recrystallization during FSP. The average micro-hardness of composite incorporated with 6 vol. % MWCNTs was 2.2 times of that of the FSPed aluminum alloy without MWCNTs.



**Fig. 2.9:** Carbon nano-structures reinforcement in surface composites (a) TEM image of MWCNT reinforced in AA5059 alloy after two passes of FSP (Izadi and Gerlich 2012) (b) good bonding as showed in the interface between MWCNT and AA1016 alloy (Q. Liu 2013). Arrows in (a) indicate survived CNTs after two passes

Powder forging route comprising mixing of CNTs with aluminum alloy was employed prior to FSP to increase the stability of CNTs in AA2009 alloy by Liu et al. (2012). CNT clusters were observed in forged composites. After one pass FSP, the cluster size was decreased. Single dispersion of the CNTs was achieved after four pass FSP and damage to CNTs during FSP was not severe. However, the CNTs in the composites were shortened to some extent and  $Al_4C_3$  formed in the matrix. Liu et al. (2013) utilized rolling after overlapping multi-pass FSP to align the CNTs in 1.5-4.5 vol. % CNT reinforced AA2009 alloy composites. The FSP zone was hot rolled at 753 K up to a total reduction in thickness of about 80%. It was found that CNTs were individually dispersed and directionally aligned in the matrix. The tube structure of the CNTs was retained and the CNT-Al interface was bonded without pores.

Zinati et al. (2014) dispersed MWCNTs in Polyamide 6 (PA 6) by FSP and a numerical model based on Lagrangian incremental formulation was developed to investigate the thermo-mechanical behavior. Simulation results showed peak temperature at the interface of tool shoulder and work-piece. Study of effective plastic strain showed that material shearing is more on advancing side as compared to retreading side. The effective plastic strain on the top surface is highest as shoulder imparts more plastic deformation on the surface.

Recently, Liu et al. (2014a) reported that by increasing FSP passes, the strength reduced due to CNT length shortening. They fabricated the 4.5 vol. % CNTs /AA2009 composite by FSP and powder metallurgy route. The maximum strength was obtained with three-passes of FSP due to the elimination of CNTs clustering. Further, when the number of FSP passes increased from three to five, both the YS and the UTS of the composite decreased due to reduced length of CNTs. A CNT shortening model was proposed by Eq. 2.12 to describe the evolution of CNT length during mechanical processing.

$$\frac{1}{L_n} - \frac{1}{L_0} = \frac{n}{2} k D^2 \epsilon \dots\dots\dots (2.12)$$

where  $L_n$  is the length of CNTs after n number of cycles of similar processing,  $L_0$  is the CNTs length before processing, k is a constant related to ultimate strain of CNT, D is the diameter of CNT and  $\epsilon$  is the imposed strain on a CNT during processing. No significant reduction in CNTs diameter was observed even after five passes of FSP. According to Eq. 12, reciprocal of CNT length exhibits linear relationship with the number of FSP passes. This CNT shortening model can also predicts the CNT length shortening by other mechanical processes.

Liu et al. (2014b) examined the electric conductivity and tensile properties of CNTs reinforced aluminum and AA6061 alloy composites fabricated by powder metallurgy and subsequent multi-pass FSP. Artificial ageing was also done for CNT/AA6061 composite after FSP. After

FSP, almost no CNT clusters were found which results in increased tensile strength. The electrical conductivity of the CNT/Al composite decreased while the electrical conductivity of the CNT/AA6061 composite increased as compared to base alloy. Increase in electrical conductivity was attributed to the decrease in Mg and Si concentration as they are segregated at the CNT and matrix interface.

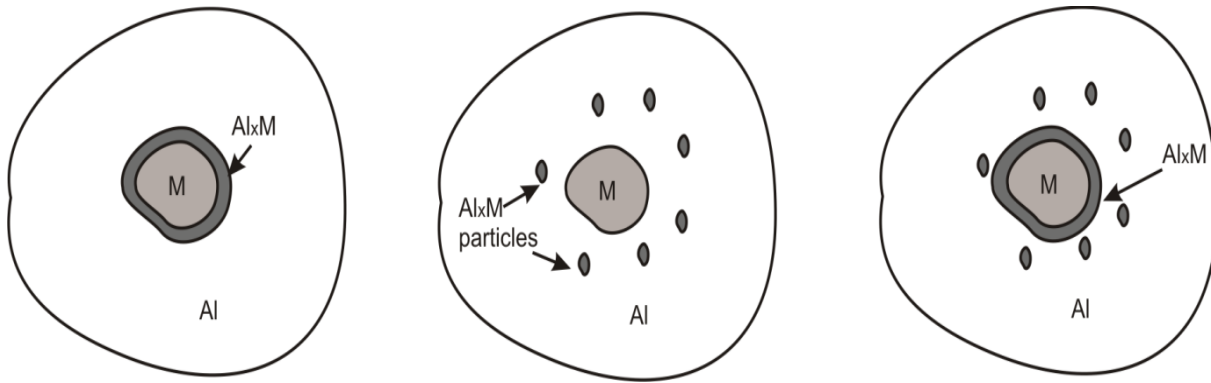
### **2.6.2 Surface in-situ composites**

In-situ composites offer many advantages such as a defect-free reinforcement-matrix interface, more thermodynamically stable reinforcements, improved compatibility, and higher bonding strength between the reinforcements and the matrix (Tjong and Ma 2000). The major problem in the fabrication of in-situ composites by conventional methods is the segregation of the in-situ formed reinforced particles (Bauri 2014). FSP is an effective route for fabricating in-situ composites as it provides synergistic effect of severe plastic deformation to promote mixing, elevated temperature to facilitate the in-situ reaction and hot consolidation to form a fully dense solid (Hsu 2006). FSP route is also attractive as in-situ formed reinforced particles are of nano-sized which contribute towards significant improvement in strength (Tjong 2007). Further, the large plastic strain imposed in FSP can effectively remove the in-situ formed particles at the interface. As the particles are removed rapidly from the interface, the growth of the particles is limited and results in nano-sized particles (Hsu 2006).

Intermetallic compounds are reported to form at the interface of aluminum matrix and reinforced element during FSP. The formation of in-situ particle  $Al_xM$  during FSP is schematically demonstrated in Fig. 2.10. The reaction during FSP occurs at interface of aluminum matrix and reinforced element (M: Ti, Ni, Fe etc.). Further processing results in increased plastic strain leading to dispersion of  $Al_xM$  particles in aluminum matrix. Again, the matrix and element M comes in direct contact to form intermetallic compound and the process is repeated. Studies are mainly reported on the fabrication of Al- $Al_3Ti$ , Al- $Al_3Ni$ , Al- $Al_3Fe$ , and Al- $Al_2Cu$  nano-composites via reactive FSP of Al-Ti, (Hsu 2006) Al-Ni, (Ke 2010) Al-Fe, (Lee 2008) and Al-Cu (Hsu 2005). Formation of additional in-situ nano-size  $Al_2O_3$  or MgO particles are also reported in oxide systems like Al- $CeO_2$  (Chen 2009), Al- $TiO_2$  (Zhang 2011), Al- $CuO$  (You 2013b) and Al-Mg- $TiO_2$  (Khodabakhshi 2014). Hsu et al. (2006) demonstrated that by FSP route, a large amount nearly up to 50 vol. % of nano-sized  $Al_3Ti$  particles can be reinforced in-situ using Al-Ti elemental powder mixtures. In this study, the pre-mixed Al-Ti alloy powders of 40  $\mu m$  size with 5 to 15 vol. % Ti were cold compacted and sintered. For Al-



15vol. % Ti, the volume fraction of  $\text{Al}_3\text{Ti}$  was near 0.5 after four FSP passes with the average size of 165 nm. The Young's modulus was 63% higher than that of Al.



**Fig. 2.10:** Schematic of in-situ particles formation and dispersion in Al matrix during FSP

Chen et al. (2009) reported the production of aluminum based in-situ composites from powder mixtures of aluminum and cerium oxide. The in-situ reinforcing phases were observed in composites even after sintering, but their distribution was homogenized after FSP. The reinforcing phases were identified as  $\text{Al}_{11}\text{Ce}_3$  with an average size of 1.4-3.5  $\mu\text{m}$ , and  $\delta\text{-Al}_2\text{O}_3$  with an average size of  $\sim 10$  nm. You et al. (2013b) also applied FSP to produce aluminum based in-situ composite using powder mixtures of aluminum and copper oxide ( $\text{CuO}$ ). The nano-sized particles of  $\text{Al}_2\text{O}_3$  and  $\text{Al}_2\text{Cu}$  were formed in-situ during FSP. Lee et al. (2013) investigated the formation of Al-Mo intermetallic particles from the mixture of aluminum and molybdenum powders via FSP. They found that FSP promotes the exothermic reaction between aluminum and molybdenum to produce fine Al-Mo intermetallic particles with an average size of 200 nm. FSP effectively removed the intermetallic particles formed at the Al/Mo interface by the shear deformation of rotating tool. Subsequently, intimate contact between Mo and Al could be maintained and the reaction proceeded without hindrance.

Due to short exposure of temperature and stirring in FSP, the reaction may not be completed and residue constituents remain un-reacted (Kee 2010, Zhang 2011, Khodabakhshi 2014). Thus, it becomes necessary to understand the heat exposure by sintering during FSP or heat treatment done prior or after FSP. Ke et al. (2010) demonstrated that nickel remain un-reacted after three passes of FSP. They reinforced nickel powder in drilled hole aluminum plate by FSP to fabricate Al-Ni intermetallic composite. After FSP heat treatment was performed at 550  $^\circ\text{C}$  for six hours. Heat treatment enhances the reaction and causes nickel to react fully to form

intermetallic composite. The UTS of composite showed 171% increase as compared to FSPed aluminum. The un-reacted constituents were also observed by Khodabakhshi et al. (2014) in TiO<sub>2</sub> reinforced AA5052 alloy in-situ nano-composites via FSP. The in-situ chemical reactions were not completed due to short processing time and more than 55% TiO<sub>2</sub> nano-particles remained un-reacted. It was observed that after annealing at 400 °C for three hours, the fraction of un-reacted TiO<sub>2</sub> nano particles significantly reduced. The annealing treatment led to a more than three times improvement in the ductility of the nano-composite without sacrificing their tensile strength and hardness.

The lower temperature and holding duration in hot pressing of Al and Ti powders may not be sufficient to initiate the in-situ reactions. At higher temperature and holding duration, Ti reacted with Al to form Al<sub>3</sub>Ti completely but a coarse particle size range of 0.5-3 μm with inhomogeneous distribution in the Al matrix was obtained. After four passes of FSP, the average size of the Al<sub>3</sub>Ti decreased and the distribution of the Al<sub>3</sub>Ti became homogeneous (Zhang 2011). The particle size influence on in-situ particle formation was studied by Zhang et al. (2012). They fabricated in-situ composites from powder mixtures of Al and TiO<sub>2</sub> using hot pressing, forging and subsequent four passes of FSP. Decreasing the size of TiO<sub>2</sub> from 450 to 150 nm resulted in the formation of more Al<sub>3</sub>Ti and Al<sub>2</sub>O<sub>3</sub> particles. In the in-situ surface composite fabricated from Al-Ti-Cu systems Zhang et al. (2013) reported liquid phase formation in Al-Ti-Cu system owing to eutectic reaction between Al and Al<sub>2</sub>Cu. The liquid phase formation accelerated the diffusion between Al and Ti resulted in the increased number of Al<sub>3</sub>Ti particles.

Anvari et al. (2013) studied the wear behavior of Al-Cr-O nano-composites fabricated in-situ by applying FSP on the plasma sprayed coating. In this study, the Cr<sub>2</sub>O<sub>3</sub> powder was applied on AA6061-T6 plate by plasma spray. After coating, six passes of FSP was conducted on the plate. During FSP, the Cr<sub>2</sub>O<sub>3</sub> was reduced with aluminum to produce pure Cr and Al<sub>2</sub>O<sub>3</sub>. Also as a result of reaction between Al and Cr, intermetallic compounds including Al<sub>13</sub>Cr<sub>2</sub> and Al<sub>11</sub>Cr<sub>2</sub> were formed. Reciprocating wear test results showed improved wear resistance in nano-composites.

### **2.6.3 Surface hybrid composites**

Surface composites with more than one type of reinforcement come in the category of hybrid composites. To achieve desired properties in composites, use of more than single reinforcement can provide satisfactory results. Hybrid composites show enhanced properties compared with single particles reinforced composites as it combines the advantages of its constituent

reinforcements. (Basavarajappa 2007). In hybrid composites, commonly a softer phase added with hard ceramic particles to achieve better tribological properties, but on the other hand the softer phase has deleterious effect on mechanical properties. So, an optimum ratio of both the constituents is required to achieve better properties in the hybrid composites (Suresha and Sridhara 2010).

The properties of hybrid composites depend on the ratio of reinforcement particles as demonstrated by Mostafapour Asl and Khandani (2013) in a study of (graphite+Al<sub>2</sub>O<sub>3</sub>)/AA5083 hybrid surface composite fabricated by FSP. They studied the effect of hybrid ratio (graphite/Al<sub>2</sub>O<sub>3</sub>) of reinforcement on mechanical and tribological properties of the surface hybrid nano-composite of aluminum alloy. The nano-composite with hybrid ratio of 3 exhibits the lowest wear rate while a hybrid ratio of 1 provides better combination of wear and tensile strength. Devaraju et al. (2013) studied the mechanical and tribological properties of (SiC+graphite)/AA6061 hybrid surface composites. They observed that increasing the graphite content up to certain limit decreases the hardness and wear rate. The graphite forms a mechanically mixed layer which avoids the direct metal to metal contact and act as a solid lubricant. The lower wear rate was observed at the optimum condition of rotational speed of 1120 rpm, 6 vol. % of SiC and 3 vol. % of graphite. Further increasing graphite content increased the wear rate due to low fracture toughness of composites.

Solid lubricant molybdenum disulphide (MoS<sub>2</sub>) reduced the wear rate by forming a stable mechanically mixed layer as indicated by Alidokht et al. (2011) in a tribological study of (SiC+MoS<sub>2</sub>)/A356 hybrid surface composites. They found that the wear resistance of hybrid composite was higher compared to SiC/A356 composite. The MoS<sub>2</sub> particles formed a mechanically mixed layer (MML) which reduces the wear rate of the composite. The unstable MML formed in the absence of the lubricant phase (MoS<sub>2</sub>), leads to lower wear resistance in SiC/A356 composite as compared to the hybrid composite though the hardness of hybrid composite was lower due to the presence of soft MoS<sub>2</sub> particles. Similarly, Soleymani et al. (2012) incorporated MoS<sub>2</sub> with SiC particles in the ratio of 1:2 in AA5083 alloy to fabricate hybrid surface composite. The hybrid composite exhibited higher wear resistance as compared to SiC/AA5083 or MoS<sub>2</sub>/AA5083 composites. The superior wear resistance of hybrid composite was attributed to presence of MoS<sub>2</sub> particles as they assisted in the formation and stability of a solid lubricating layer.

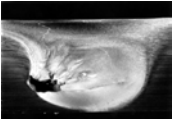

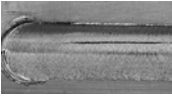
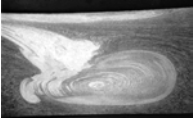

## 2.7 Defects in FSPed composite surfaces

Improper selection of process parameter results in defects in FSPed zone. FSP is susceptible to similar defects which are observed in FSW. Incorporation of second phase particles may hinder material flow during fabrication of surface composites. This may also increase chances of defect formation. Table 2.5 shows common types of defects observed in FSW. Defects include worm hole, scalloping, ribbon flash, cavity, surface lack of fill, nugget collapse and surface galling (Arbegast 2008).

During FSP of surface composites insufficient material flow may leaves a cavity or tunnel in the processing zone. The plunge depth and rotational and traverse speed are prominent parameters for defect free processing (Elangovan 2007; Padmanaban and Balasubramanian 2009). Commonly, the defects tend to occur on the advancing side where an abrupt microstructural transition occurs from the highly refined SZ to the TMAZ, while the transition is gradual on the retreating side (Nandan 2008). Kim et al. (2006) pointed out three common defects in FSW of aluminum cast ADC 12 alloy. They observed flash due to the excess heat input, a cavity like defect (hole) caused by an insufficient heat input and cavity produced by the abnormal stirring (Table 4). The tool probe is also responsible for defect formation in the SZ as indicated by Elangovan and Balasubramanian (2008) in FSW of AA2219 alloy. Gandra et al. (2011) observed triangular cavities near the SZ in SiC/AA5083 surface composites. Particle agglomeration was also observed. Further, they found that cavity on the advancing side was almost empty while the cavity on the retreating side was filled with compacted particles under the compressive forces exerted by the material flow. The defects formation was due to insufficient material flow influenced by the existence of SiC particles.

In fabrication of SiC/Ti nano-composites, it was reported by Shamsipur et al. (2011) that defect free surface composites can be fabricated by utilizing optimum range of rotational ( $\omega$ ) and traverse speed ( $v$ ). At relatively low ratio of  $\omega/v$  the tunneling defect was observed due to insufficient plastic deformation and flow of material because of less interaction time between tool and material. Sharifitabar et al. (2012) also observed large voids, and tunnels in the SZ of  $Al_2O_3/AA5052$  surface nano-composite FSPed at low  $\omega/v$  ratios. The low tilt angle of the tool caused the formation of void even if samples FSPed with high  $\omega/v$  ratio. This was attributed to low heat input at low  $\omega/v$  ratios which decreased materials flow in the SZ during stirring leading to the formation of large voids and tunneling defect.

**Table 2.5:** Common types of defects observed in FSW of alloys (Arbegast, 2008)

Defect	Description	Probable reasons
<p>Worm hole</p> 	<p>An advancing side tunnel of inadequately consolidated and forged material running in the longitudinal direction.</p>	<ul style="list-style-type: none"> <li>▪ Excessive travel speed for given rotational speed</li> <li>▪ Cold weld</li> <li>▪ Too low weld pitch</li> </ul>
<p>Ribbon flash</p> 	<p>Excessive expulsion of material on the top surface leaving a corrugated or ribbon like effect along the retreating side.</p>	<ul style="list-style-type: none"> <li>▪ Excessive forge load or plunge depth</li> <li>▪ Excessively hot weld</li> <li>▪ Too high weld pitch</li> </ul>
<p>Surface lack of fill</p> 	<p>A continuous or intermittent top surface void on the advancing side.</p>	<ul style="list-style-type: none"> <li>▪ Insufficient flow arm formation across top surface</li> <li>▪ Insufficient forge pressure</li> <li>▪ Improper backside support</li> <li>▪ Insufficient plunge depth</li> </ul>
<p>Nugget collapse</p> 	<p>Improper formation of dynamically recrystallized nugget shape.</p>	<ul style="list-style-type: none"> <li>▪ Excessive Flow Arm Formation and injection of material into Advancing Side</li> <li>▪ Excessively hot weld</li> <li>▪ Too high weld pitch</li> </ul>
<p>Surface galling</p> 	<p>Galling and tearing of the metal on the top surface of the weld beneath the pin tool.</p>	<ul style="list-style-type: none"> <li>▪ Sticking of metal to pin tool</li> <li>▪ Excessively hot weld</li> <li>▪ Too high weld pitch</li> </ul>

Insufficient tool penetration depth (PD) is a common cause for defects in SZ. The PD has to be optimized to supply enough heat to the material so that defects like longitudinal cracks and tunneling cavity are not formed in the processing zone (Asadi 2010). Tool geometry is also one of the factors in defect formation in SZ. In FSP of Al<sub>2</sub>O<sub>3</sub>/AZ31 surface nano-composites, Azizieh et al. (2011) reported that defect-free SZ was observed with threaded probe tool whereas non-threaded and three-fluted probes left cavities and micro-voids in the specimens due to the less material flow.

## 2.8 Summary

FSP is a versatile technique for fabricating surface composites. The grain refinement achieved by FSP and the solid state nature of processing are the unique advantages of this process. Nanocrystalline grains have been reported in several surface composites fabricated by FSP. The surface composites exhibit high hardness as well as increased wear and corrosion resistance. FSP is a relatively new technique for fabrication of surface nano-composites and offers ease of particle dispersion. A number of reinforcements including ceramic and metallic particles and carbon nano-tubes have been successfully incorporated in metallic matrix by FSP. Elimination of clustering of nano-particles can be achieved. Surface nano-composites fabricated by FSP are defect free without voids and have a homogeneous particle distribution. In fabricating in-situ composites, FSP route is advantageous due to rapid removal of reaction products from interface which enhances further reaction. Moreover, the in-situ formed particles are in nano-meter regime. Hybrid composites comprising a hard and a soft reinforcement have been successfully produced with promising properties. To harness the full potential of nano-composites various methodologies to achieve uniform distribution have been used in FSP. Initial studies pertaining to coating pointed out that application and stability of coating can be significantly improved by FSP. Micro alloying with low melting point metals like tin, lead etc. can be incorporated in the surface composite. FSP of polymers and polymeric composites was initiated recently and the initial results are encouraging, but further investigation is required due to low melting point and polymeric chain structure arrangement. The tool wear is important issue in FSP especially in preparing high temperature melting point materials such as steel, titanium or ceramic particle reinforced composites. Tools of polycrystalline cubic boron nitride, tungsten based alloys etc. are recommended for FSP of hard materials. However, the high cost and low fracture toughness of these tools limits their usage. These limitations restrict the use of FSP technique to prepare hard surface composites. Most of the surface composites fabricated so far is of aluminum based. Surface composites of harder alloys still await the development of cost effective and durable tools. Further, a concrete understanding on FSP approaches to obtain uniform distribution of reinforcement particles in aluminum alloy surface composites is still not available. Also, tribological performance of surface composites of aluminium alloys is not thoroughly understood as function of FSP parameters such as rotational speed, traverse speed, external cooling, tool geometry and multi-pass.



*In this chapter, experimental techniques used for the fabrication and tribological characterization of aluminum alloy surface composites are briefly mentioned. First, details about aluminum alloys, reinforcement particles are provided. This is followed by details of the friction stir processing with information about tool geometry. Major techniques to understand microstructure and mechanical properties are also given. Details about sliding wear test procedure and worn surface characterization are also provided.*

**3.1 Aluminum alloys**

Three different alloys of aluminum: Al-Cu AA2014, Al-Si alloy LM24 and Al-Mg alloy AA5083 alloys were used in the present study. The compositions of as received alloys were determined by optical emission spectrometry, and results are given in **Tables 3.1-3.3**. AA2014 and AA5083 flat sheets of 6.35 mm thickness were procured from M/s. Virat aluminum Pvt. Ltd. (Mumbai, India), while LM24 alloy were received in the form of ingots and sliced into plates of 6 mm.

**Table-3.1:** Chemical composition of as received AA2014

Cu	Si	Fe	Mn	Mg	Cr	Zn	Ti	Al
4.1	0.61	0.2	0.56	0.6	0.01	0.07	0.06	remainder

**Table-3.2:** Chemical composition of as received AA5083

Mg	Si	Fe	Mn	Zn	Ti	Cu	Al
4.2	0.4	0.4	0.5	0.25	0.15	0.1	remainder

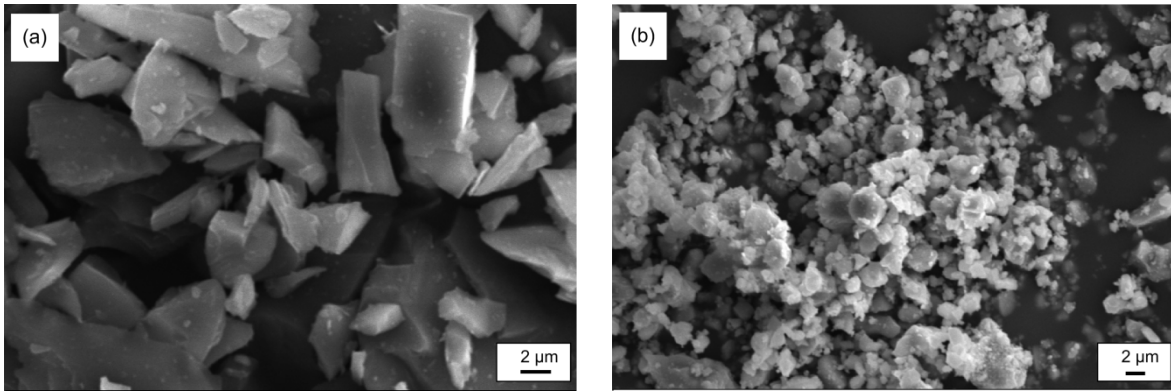
**Table-3.3:** Chemical composition of as received LM24 alloy

Si	Cu	Mg	Fe	Mn	Ni	Zn	Pb	Sn	Ti	Al
8.2	3.5	0.3	1.2	0.5	0.4	2.1	0.6	0.2	0.2	remainder

**3.2 Reinforcement particles:**

Silicon carbide (SiC) particles of average size of 30  $\mu\text{m}$ , titanium carbide (TiC) particles of average size of 4  $\mu\text{m}$ , graphite flakes of average size of 500  $\mu\text{m}$  and tin (Sn) powder particles of average size of 70  $\mu\text{m}$  were used as reinforcement in this study. SEM images of SiC and TiC particles are shown in **Fig. 3.1**.





**Fig. 3.1:** SEM images of reinforcement (a) SiC particles (b) TiC particles

### **3.3 Friction stir processing setup**

A conventional vertical milling machine with a fixture attachment to hold the aluminium plates was used for FSP in the present investigation. The FSP setup is presented in Fig. 3.2. The machine is capable of providing twelve combinations of rotational and traverse speeds ranging from 45-2000 rpm and 16-630 mm/min, respectively.

The aluminium alloy plates were cut into required size of (110 mm x 60 mm x 6.35 mm) for performing FSP. The plates were rubbed with a 1200 grit emery paper to remove oxide layer and cleaned with acetone. The plate was firmly clamped on fixture. The tool is tilted to 2.5° from the normal of the workpiece away from the direction of travel to facilitate the processing.



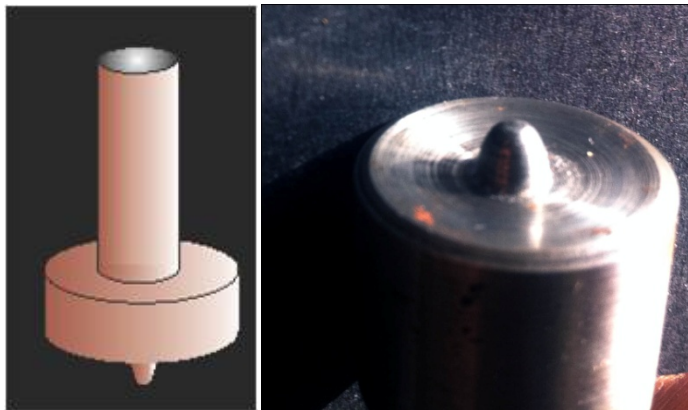
**Fig. 3.2:** Vertical milling machine used for FSP experiments



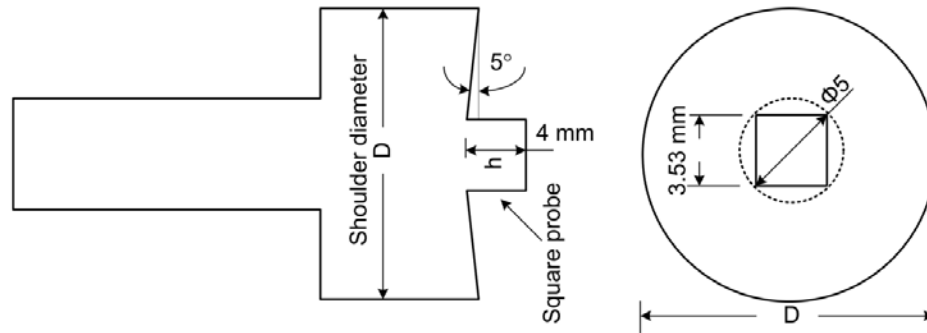
**Fig. 3.3:** Processed AA2014 after four passes of FSP

### 3.4. Tools

A square probe and round bottom conical tool was used for FSP in the present work. The multi-pass FSP and LM24 surface composites were fabricated by using round bottom conical probe. A H13 steel tool (55 HRC) with a round bottom conical pin of 3 mm length and 5 mm diameter at the top which reduced to 3 mm at the bottom, and concave shoulder of 21 mm diameter was used. A schematic design and image of round bottom conical probe tool is shown in **Fig. 3.4**. A square tool probe was used for fabricating  $\text{Al}_2\text{O}_3/\text{AA5083}$  (discussed in **Chapter-7**) surface composite and  $\text{SiC}/\text{AA5083}$  surface composite (discussed in **Chapter-5**). The dimensions and sketch of square tool probe is presented in **Fig. 3.5**. A H13 steel tool with a concave shoulder of 21 mm diameter and square probe of 4 mm height and 5 mm ex-circle diameter (circle drawn on the outer periphery of tool probe) was used in FSP. Each side of square probe is 3.53 mm. A second tool used was of the same dimension but with a probe diameter of 6 mm.



**Fig. 3.4:** Schematic design and fabricated tool of round bottom probe tool



**Fig. 3.5:** Sketch of square probe tool geometry utilized for fabrication of surface composites

### 3.5. Processing

The combinations of rotational speed and traverse speed were set as per the requirement. Then, rotating tool was plunged in to the work piece and moved into the direction of interest. In multi-pass FSP, the workpiece was cooled to room temperature after one pass before subjecting to subsequent pass. The FSPed workpiece was cut for metallographic and other investigation. The workpiece with four passes of FSP is shown below in the Fig. 3.3. For fabricating the surface composite layer, groove and blind hole methods were used. The groove was machined in the alloy plate with a dimension of 1.5 mm width and 2 mm depth by the horizontal milling machine. The particles were placed in the groove and tool without probe was used to pack the groove. After packing of the groove, FSP was performed on the plate. In blind hole method, holes of 2 mm diameter and 2 mm depth with a spacing of 1 mm were drilled on the plate. The reinforcement particles were filled in holes and compacted by 2 mm rod to closely pack the reinforcement particles. A 0.8 mm aluminium plate was placed on the top of the plate to prevent reinforcement particles ejecting out during the FSP.

The multi-pass FSP of AA2014 was done at rotational speed of 1000 rpm and traverse speed of 63 mm/min as discussed in chapter-4. The SiC/AA2014 and TiC/AA2014 surface composites are fabricated at rotational speed of 710 rpm and 100 mm/min. The LM24 alloy surface composites were fabricated at a rotational speed of 1000 rpm and 63 mm/min as discussed in chapter-6. The Al<sub>2</sub>O<sub>3</sub>/AA5083 surface composite was fabricated at a rotational speed of 1400 rpm and traverse speed of 40 mm/min.

### 3.6. Volume percentage of reinforcement:

The volume percentage of reinforcement particles in the surface composite fabricated by FSP was calculated using volume of drilled hole, particles packing fraction (~60%) and volume of processed zone from height and diameter of probe. A formula derived to calculate volume fraction of reinforcement particles ( $V_p\%$ ) is given below in **Eq 3.1**. Nearly 40 blind holes of 2 mm diameter and 2 mm depth with 1 mm spacing were drilled on the workpiece to accommodate reinforcement particles.

$$V_p \% = \frac{n \times \pi r^2 h \times 0.6}{a \times b \times l} \times 100 \quad \dots\dots\dots (3.1)$$

Where n is number of holes drilled, r and h are the radius and depth of the hole, a and b are the height and diameter of the probe. In the present study, nearly 12% volume fraction of reinforcement particles was used.

### 3.7. Microscopic analysis

Microscopy of the processed specimens was done using an optical microscope (LEICA DMI5000 M, Leica microsystems, Germany). Optical micrographs were stitched by the Leica application suite. Samples for metallographic analysis were sliced perpendicular to the direction of processing. Further, specimens were grinded and polished following standard grinding and polishing techniques. The specimens were grinded on belt grinder using emery paper of 100 grit size and then manually polished using emery paper of 320, 600, 800, 1200, 1500 and 2000 grit size. After polishing with emery paper, velvet cloth polishing was performed with magnesium oxide slurry in distilled water. Etching was done using the modified Poulton's reagent (30 ml HCl, 40 ml HNO<sub>3</sub>, 2.5 ml HF, 12 g CrO<sub>3</sub>, 42.5 ml H<sub>2</sub>O) for 15 seconds.

The electron microscopy of the specimens was conducted on scanning electron microscopy (SEM) (ZEISS EVO MA) equipped with energy dispersive spectroscopy (EDS), FE-SEM (QUANTA 200F, FEG LaB<sub>6</sub>, 30 kV) with EDS attachment and transmission electron microscope (TEM) (Techai G<sub>2</sub> 20 S-TWIN at 200 kV). For TEM specimen preparation, a thin slice of 1 mm from the specimen was cut by a precision diamond wheel cutter. The slice was thinned down by metallographic polishing with a 1500 grit emery paper to a thickness of 0.1 mm. Finally, a 3mm diameter disc was cut by a punch. The disc shaped specimen was

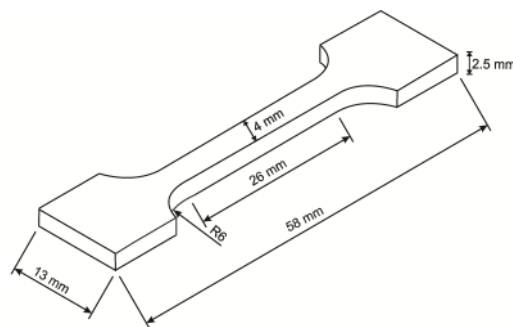
electropolished by a twin-jet electro polisher in a solution of 80% CH<sub>3</sub>OH and 20% picric acid at 12 V and -35 °C.

### 3.8. Hardness measurement

The hardness test was performed on Vicker's microhardness tester (Omnitech MV II, India) and Vicker's macrohardness (FIE VM50 PC, India). For microhardness measurement, a 200 gf load was employed for a dwell time of 15 seconds. The microhardness of the FSPed samples and surface composites was taken in transverse section of processed zone. In SZ hardness, total ten measurements were taken for each specimen and the average value with standard deviation was reported. The hardness of steel ball was estimated using a Vicker's macrohardness tester at 10 kgf load for a dwell time of 15 seconds.

### 3.9. Tensile tests

The tensile tests were conducted on an Instron universal testing machine (UTM) (25 KN, H25 K-S, UK). The flat shape tensile specimens were cut from the processed zone and tested with a cross head speed of 1 mm/min. The tensile specimen dimensions are shown in Fig. 3.6.



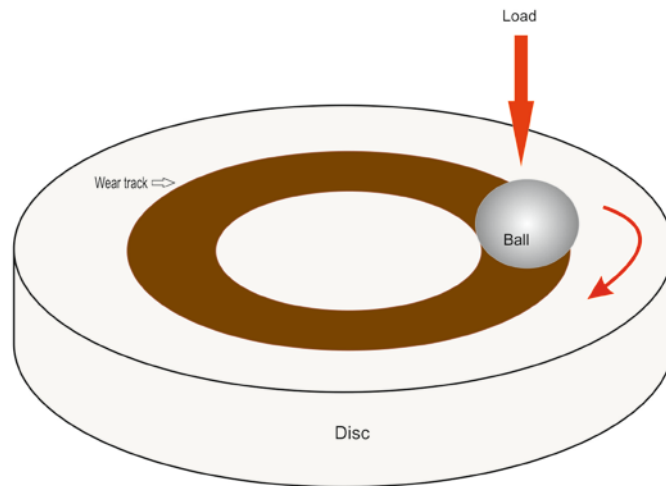
**Fig. 3.6:** Dimensions of tensile test specimen

### 3.10. Heat treatment:

The heat treatment of steel balls was performed in an atmosphere controlled tube furnace in argon atmosphere at 923 K (650 °C) and 753 K (480 °C) for one hour holding time. After heat treatment, the steel balls were quenched in the distilled water (25 °C). The balls were pickled with 10% HCl and thoroughly cleaned with acetone. The average Vickers hardness of steel balls was found to be 300 Hv after heat treatment at 923 K and 450 Hv after heat treatment at 753 K.

### 3.11. Sliding wear test:

The dry sliding wear test in this study was conducted on a ball-on-disc sliding contact wear and friction testing machine (DUCOM TR-201E-M2, Bangalore, India). The schematic representation of ball-on-disc is shown in Fig. 3.7. Commercially available bearing grade AISI 52100 steel balls of 6 mm diameter ( $\sim 800$  H<sub>V</sub>) were used as the mating counterpart. The ball was mounted in a holder and polished specimen disc was mounted onto the platform in the basin of a ball-on-disc sliding contact wear and friction testing machine. Both disc sample and steel balls were ultrasonically cleaned with acetone before and after the wear testing, and dried in hot air stream. Tribological tests were performed in the laboratory ambient conditions of  $25 \pm 5$  °C and  $30 \pm 10\%$  RH. The track radius of ball holder was adjusted so as to make a travelling circle diameter of 3.0 mm from the central axis. Tests were performed at a fixed rotational speed of 500 rpm (linear speed of 0.157m/s) at 5 N or 20 N load. During test runs, frictional force was recorded using an electronic sensor to generate real time coefficient of friction (COF) data. The wear volume was calculated by worn surface profile on the disc.



**Fig. 3.7:** Schematic of ball-on-disc wear testing

### 3.12. Profilometry

A contact type surface profilometer (Mitutoya Surftest SJ-401, Japan) with a stylus having a diamond tip of 90° angle and tip curvature of 2µm radius and a non contact type (Veeco Wyko NT 1100) was used in this study. To calculate the wear volume, surface profilometer was used to trace surface profiles of worn disk specimen to measure the depth, width of the wear tracks of the specimens after each individual test. The measuring method involved with firstly scanning the wear depth profile across a wear track at various locations, and then determining

the average of maximum depth and width. The average of wear track width and depth were further used in computing the wear volume in (mm<sup>3</sup>) according to following relation:

$$\text{Wear volume} = (2 \pi \times \text{Track radius}) \times (\text{Track width}) \times (\text{Track depth}) \dots \dots \dots (3.2)$$

### **3.13. Wear mechanisms study**

The worn surfaces of discs and balls were subjected to SEM-EDS analysis to elucidate the dominant mechanisms of material removal occurring in selected wear conditions. Debris particles were collected during the sliding experiment and were also subjected to SEM-EDS analysis.

---

*In the present part of the thesis, microstructures and mechanical behavior of AA2014-T651 alloy fabricated by one pass FSP and four pass FSP are first studied. This is followed by the fabrication of SiC or TiC particles reinforced AA2014 alloy surface composites by multi-pass FSP and their microstructural and mechanical characterization.*

#### **4.1 Background**

Surface composites with various reinforcement particles were fabricated in the past decade. Choi et al. (2013) fabricated surface composite reinforced with 4  $\mu\text{m}$  size SiC particles in A356 alloy by FSP route. It was reported that FSP resulted in reduction in acicular silicon size and SiC particle size. The hardness of surface composite was also increased to 85 Hv as compared to base alloy hardness of 60 Hv. Asadi et al. (2010) reinforced 5  $\mu\text{m}$  sized SiC particles in AZ91 alloy to fabricate surface composite layer. They reported that due to SiC reinforcement particles and FSP, the surface composite grain size reduced from 150 to 7.17  $\mu\text{m}$ . The stir zone hardness also increased from 63 to 96 Hv because of SiC particles and grain refinement. Barmouz et al. (2011c) fabricated SiC/Cu surface composite with SiC particles size of 5  $\mu\text{m}$  by FSP. It was observed that UTS and elongation percentage was decreased in surface composite reinforced with SiC, whereas in FSP of copper the elongation percentage increased up to three times. They attributed strength reduction to agglomeration of SiC particles.

In this work, effect of multi pass friction stir processing on microstructural and mechanical properties of AA2014 alloy is demonstrated. This is followed by the fabrication of surface composites reinforced with SiC particles or TiC particles in AA2014 alloy by multi pass FSP.

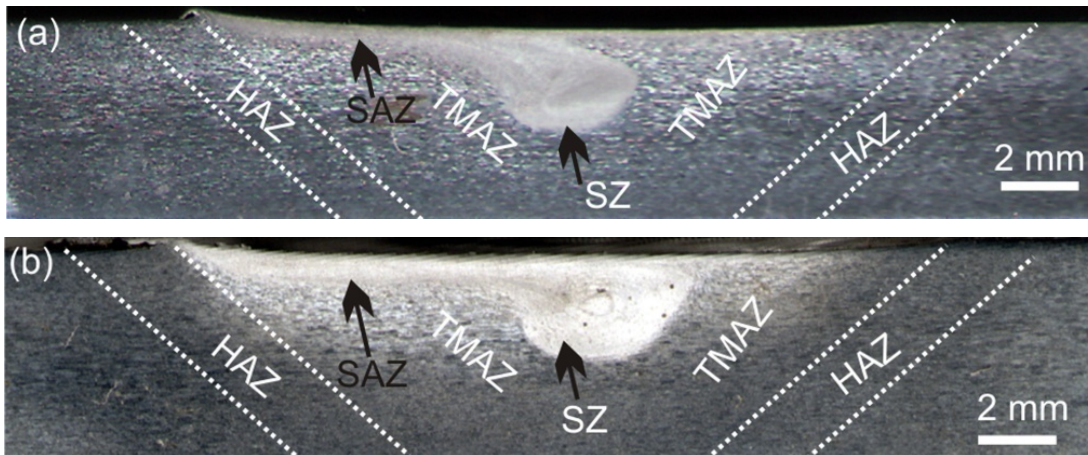
#### **4.2 Effect of multi-pass FSP on microstructure and mechanical properties of AA2014-T651 alloy**

##### **4.2.1 Microstructural characterization:**

Typical optical images of one pass FSPed and four pass FSPed AA2014-T651 alloy exhibiting various microstructural zones are shown in Figs. 4.1 (a) and (b), respectively. Shoulder affected zone (SAZ), thermo-mechanical affected zone (TMAZ), heat affected zone (HAZ), along with advancing side (AS) and retreating side (RS) are distinctly shown. It is clearly evident from images that SZ area of four pass FSPed specimen is large as compared to that of one pass FSPed specimen. A tilted oval shaped and distinct SZ is discernable in one pass FSPed

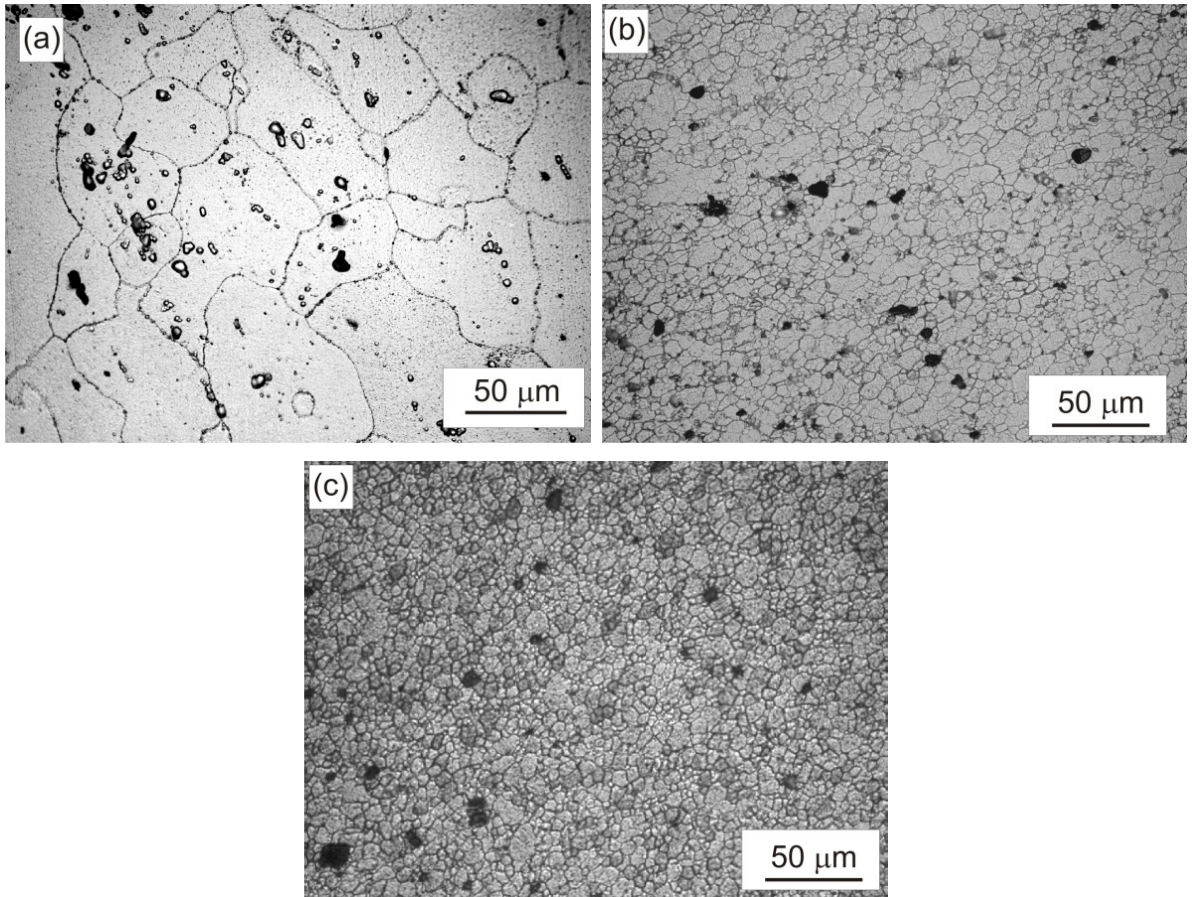


specimen, whereas semi-circular SZ is observed in four pass FSPed specimen. The SAZ is also increased after four passes of FSP. In four pass FSP, repeated thermal cycles and plastic deformation resulted in increased SZ area. As reported in earlier studies, material flow in SZ is governed by shoulder driven and probe driven flow (Kumar and Kailas, 2008). Repetitive thermal cycles with intense plastic deformation probably resulted in merging of SAZ and SZ after four passes of FSP.

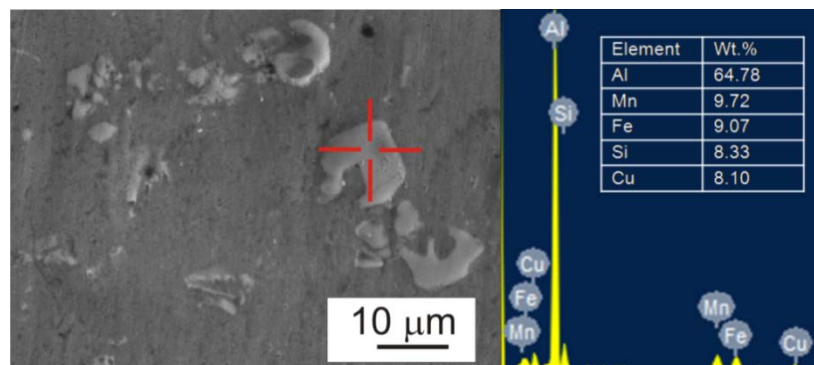


**Fig. 4.1:** Macrographs of (a) one pass FSPed specimen (b) four pass FSPed specimen exhibiting various microstructural zones

Optical micrographs of base alloy, stir zones after one pass and four passes of FSP are shown in Figs. 4.2 (a-c). Micrograph of the base alloy AA2014, as shown in Fig. 4.2 (a) reveal uneven grain size with coarse precipitates. In base alloy, average grain size is found to be 125  $\mu\text{m}$ . Using EDS analysis, these precipitates are confirmed to be composed of Al-Cu, Al-Cu-Mg-Si or Al-Fe-Mn-Cu-Si. Representative EDS analysis of precipitates in base alloy is given in Fig. 4.3. After one pass of FSP, the grain size significantly reduced to 12  $\mu\text{m}$ , but grain size distribution is not uniform in the SZ (Fig. 4. 2b). High temperature exposure caused some of the precipitates to dissolve but few coarse precipitates still exist. Fine grains in SZ were ascribed to dynamic recrystallization in previous studies (Mcnelley 2008; Zhou 2009). After four passes of FSP, SZ exhibits uniform grain size with an average grain size of 7  $\mu\text{m}$  (Fig. 4.2c). Grain size reduction after four passes of FSP is attributed to the repeated severe plastic deformation after each pass of FSP. More grain boundary area is available after each FSP passes, resulting in an increase in number of dislocations, as grain boundaries are sources of dislocations. The dynamic recovery arranges dislocations into sub-grain boundary configuration in aluminum alloys due to high stacking fault energy (Bauri 2011).

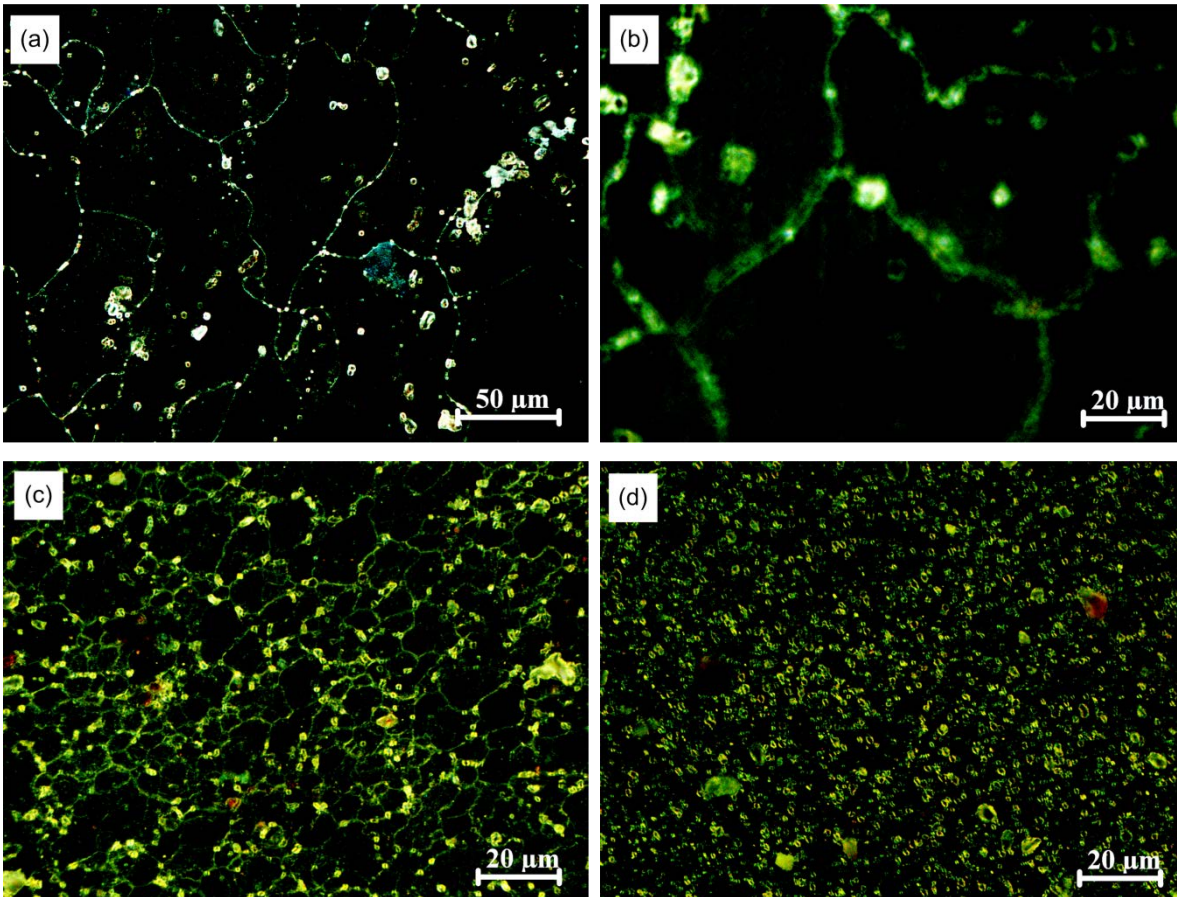


**Fig. 4.2:** Optical micrographs of (a) base alloy (b) one pass FSPed alloy (c) four pass FSPed alloy

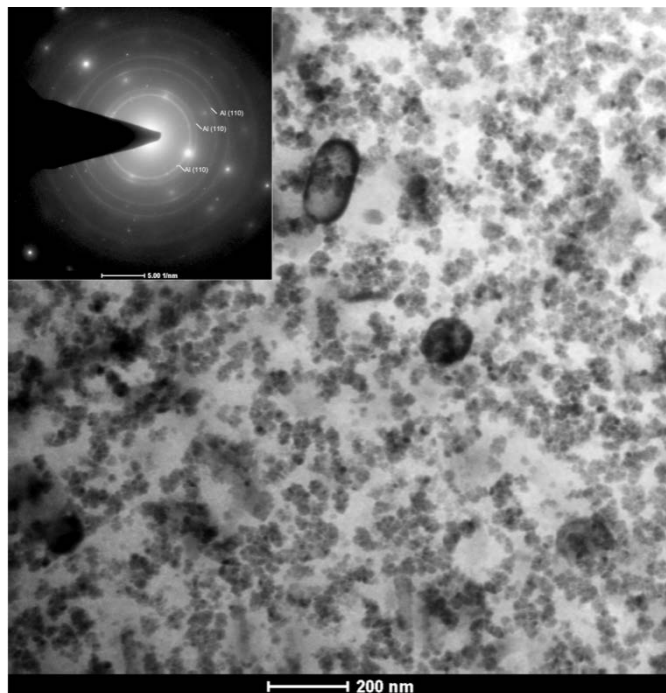


**Fig. 4.3:** SEM image of base alloy and corresponding EDS analysis of precipitates

Fig. 4.4 (a-d) show cross polarized optical micrographs of the base alloy, one pass FSPed alloy and four pass FSPed alloy. The second phase particles are clearly distinguished in polarized micrographs. After four passes of FSP, the coarse second phase particles are refined and uniformly distributed in the matrix (Fig. 4.4d). Furthermore, TEM-SAED analysis of four pass FSPed specimen indicates overaging of crystalline precipitates (Fig. 4.5).



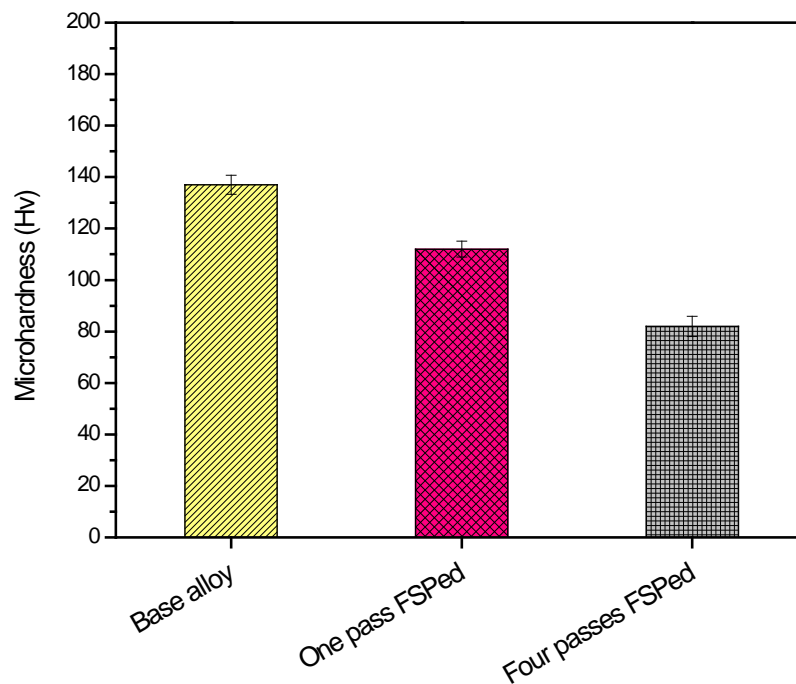
**Fig. 4.4:** Cross polarized optical micrographs of (a) base alloy exhibiting coarse precipitates (b) base alloy at higher magnification showing second phase continuous grain boundary network (c) one pass FSPed alloy (d) four pass FSPed alloy



**Fig. 4.5:** TEM image of four pass FSPed SZ. The SAED pattern is shown in inset

#### 4.2.2 Hardness:

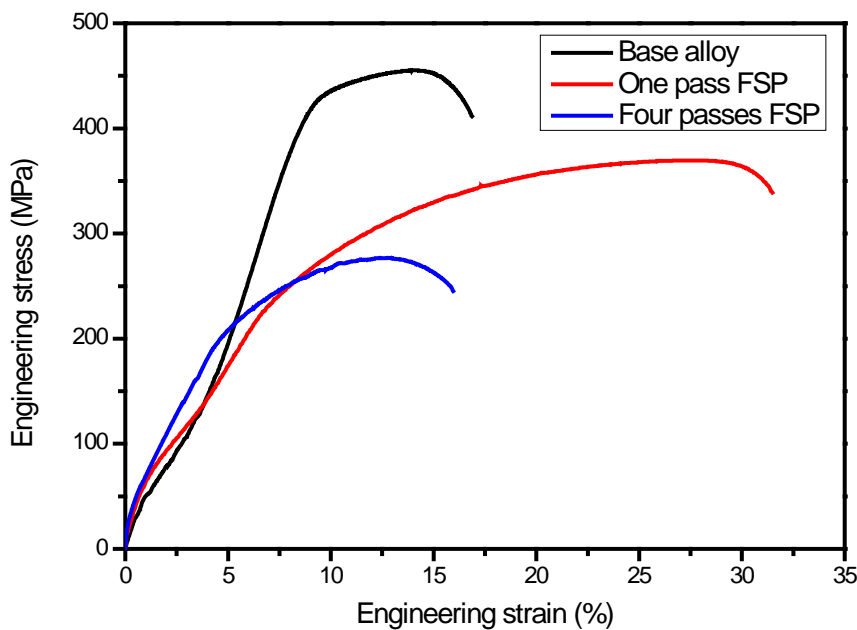
Fig. 4.6 shows distribution of microhardness in transverse section of the processed specimen. One pass FSPed alloy shows higher hardness than four pass FSPed alloy, but it is lower as compared to base alloy hardness. High hardness of as-received base alloy is due to T651 treatment (solutionized, quenched, stress relieved and artificially aged). Lower hardness in FSPed specimens can be attributed to the dissolution or overaging of precipitates due to high temperature exposure and microstructural softening. The softening or low hardness of SZ of FSPed T6 condition aluminium alloy was also observed in earlier studies (El-Rayes and El-Danaf 2012; Woo 2007). Dilip and Ram (2013) demonstrated that hardness reduces due to overaging of precipitates rather than dissolution of precipitates in multi-layer friction deposition of AA2014-T6 alloy. In four passes, the specimen experiences four thermal cycles as that of one cycle in one pass. After four thermal cycles, significant grain refinement occurs, but its contribution to hardness is limited as compared to overage precipitates contribution to softening. El-Rayes and El-Danaf (2012) reported softening of SZ in FSP of AA6082-T651 alloy due to the decomposition of hardening precipitates, overaging of precipitates and low dislocation density. Woo et al. (2007) observed microstructural softening or low hardness in SZ due to dissolution of the precipitates in FSP of AA6061-T6.



**Fig. 4.6:** Microhardness of SZ in base alloy, one pass and four pass FSPed specimens

### 4.2.3 Tensile behavior:

Typical stress-strain curves for base alloy, one pass and four pass FSPed specimens are shown in Fig. 4.7. Regardless of the grain refinement, FSPed specimens show a reduction in tensile strength as compared to base alloy specimen. Base alloy shows maximum ultimate tensile strength (UTS). The UTS exhibits a decreasing trend from one pass to four passes of FSP. The tensile strength is ~ 455 MPa for base alloy, while it is ~369 and ~278 MPa for the one pass and four pass FSPed specimens, respectively. Microstructural softening, as discussed earlier in four passes of FSP resulted in lower UTS. One pass FSPed specimen shows lower UTS as that of base alloy, but a two-fold increase in the ductility is also observed. Earlier studies on other aluminium alloys also reported higher UTS and decreased elongation percentage for one pass FSPed specimen as compared to multi-pass FSPed specimen (El-Rayes and El-Danaf 2012; Al-Fadhlah 2014).

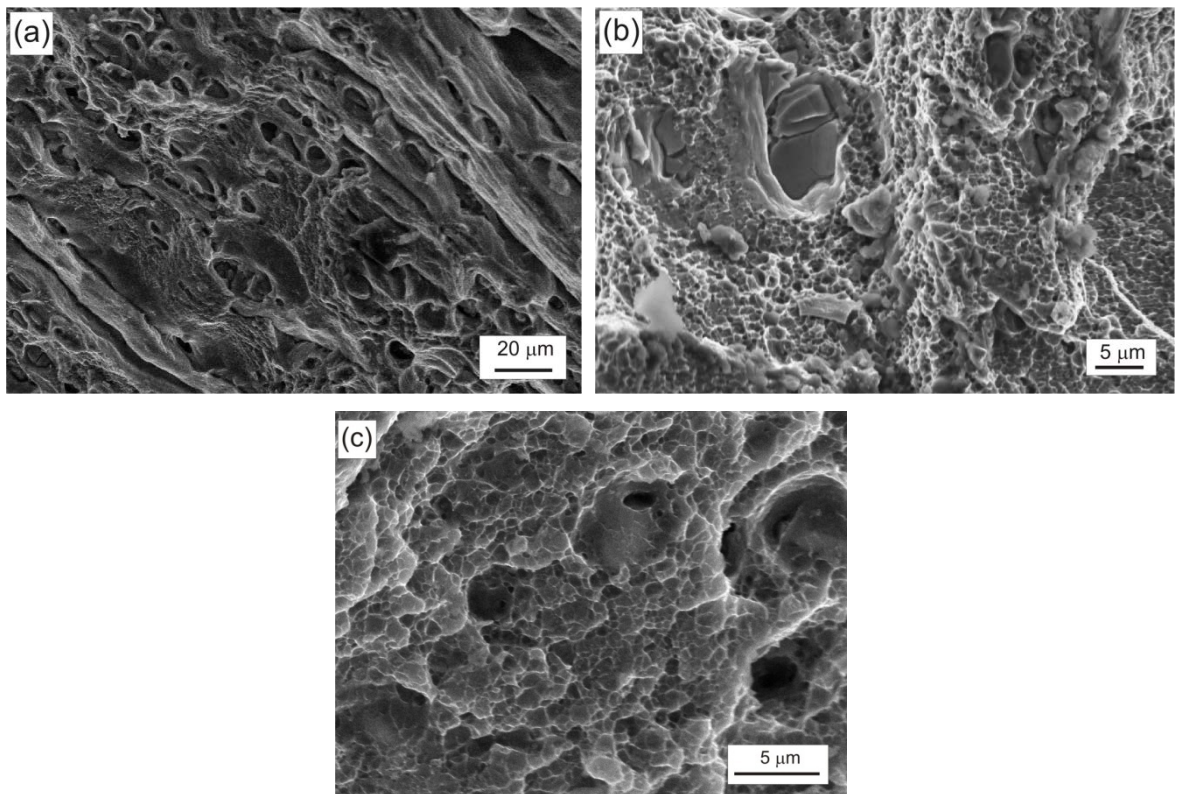


**Fig. 4.7:** Typical stress-strain curves for base alloy, one pass and four pass FSPed specimens

### 4.2.4 Fracture surfaces

Representative SEM images of fracture surfaces of base alloy, one pass and four pass FSPed are shown in Fig. 4.8 (a-c). Fracture surface of base alloy exhibits dimples along with tear ridges (Fig. 4.8a). Fracture surface of base alloy exhibits large dimples as void nucleation occurs from coarse precipitates. One pass FSPed specimen exhibits bi-modal distribution of dimple size with large dimples nucleating from coarse precipitates and fine dimples originating

from aluminum matrix (Fig. 4.8b). Cracking of coarse precipitates is also observed in fracture surface of one pass FSPed specimen. In one pass FSPed specimen, a few coarse precipitates still exist. Four pass FSPed specimen fracture surface shows fine dimples with few coarse dimples (Fig. 4.8c). Four passes of FSP resulted in distribution and break up of coarse precipitates in the matrix. The fine and closely spaced dimples are originated from the fine precipitates. Some shallow dimples are also observed, suggesting the joining of micro-voids by shear deformation.



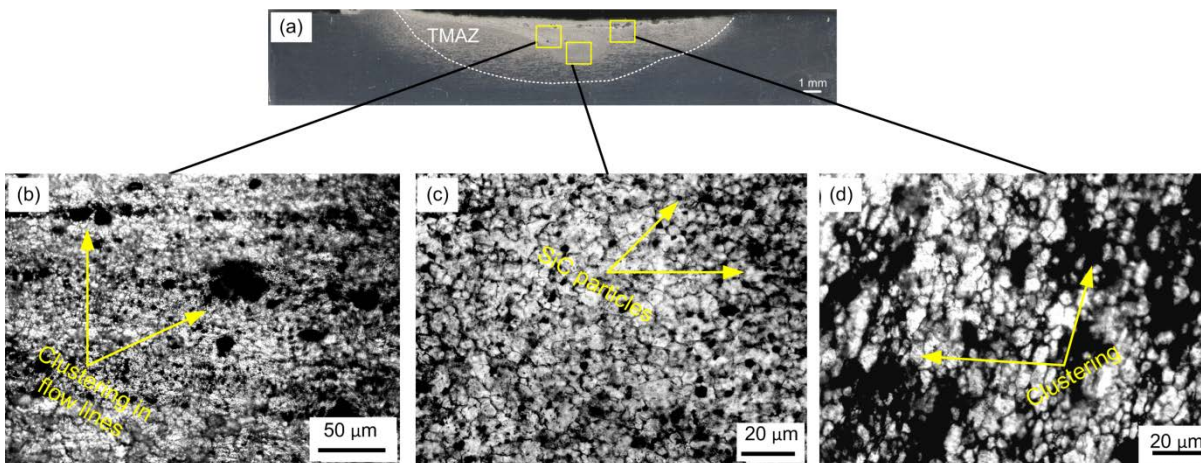
**Fig. 4.8:** Fractographs of (a) base alloy (b) one pass FSPed specimen (c) four pass FSPed specimen

In summary, multi-pass FSP results in grain refinement than one pass FSP for AA2014-T651 alloy. However, extensive dissolution or overaging of precipitates in FSP causes softening and reduces the hardness of the base alloy. The reinforcement of strong and hard ceramic particles is likely to improve mechanical properties of FSPed AA2014-T651 alloy.

### 4.3 Microstructural and mechanical characterization of multi pass friction stir processed SiC/AA2014 and TiC/AA2014 surface composites

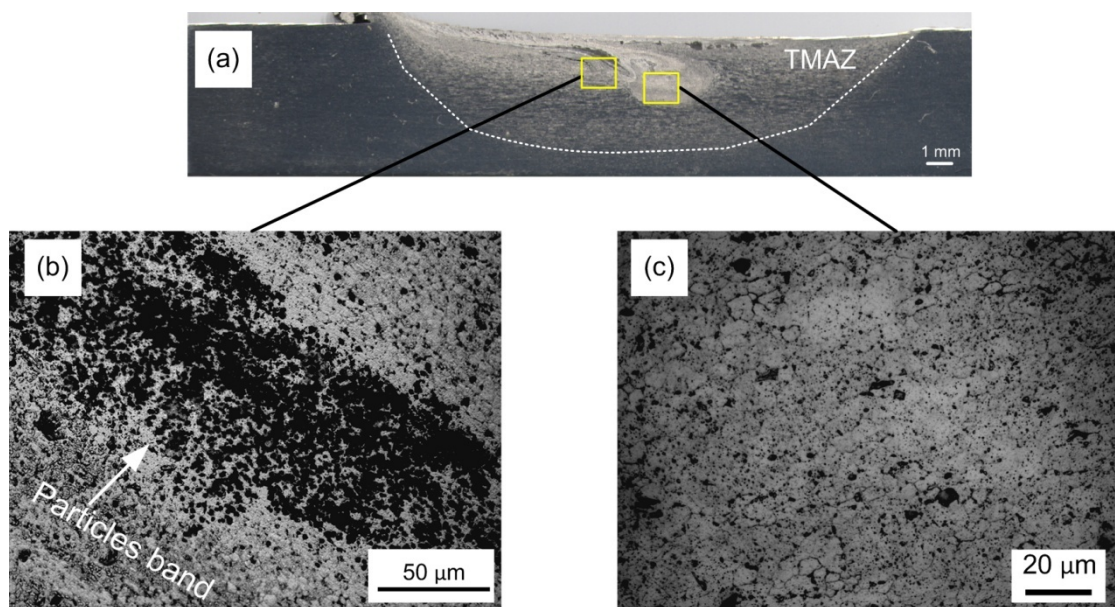
#### 4.3.1 Microstructural study

Typical optical macrograph and micrographs of transverse section of SiC particles reinforced AA2014 surface composite are shown in Figs. 4.9 (a-d). The region enclosed by the dashed line in transverse section of the composite (Fig. 4.9a) indicates TMAZ region. The shoulder imparts deformation in TMAZ region, while tool stirs the SZ region. Clustering of SiC particles in material flow lines is noted in Fig. 4.9 (b). Due to intense stirring, particles moves upward and trapped in the upper part of SZ during processing. The particle clustering in the shoulder zone is due to the absence of stirring. Material flow in this region is governed by rotating shoulder, while distribution of SiC particles in the top layer depends on the shoulder driven material flow. The stir zone of the surface composite exhibits uniform distribution of SiC particles (Fig. 4.9c). The average grain size of the surface composite is 8  $\mu\text{m}$  in SZ. Size reduction of SiC particles due to stirring action of tool under axial load is also observed. Morisada et al. (2006) observed size reduction of SiC particles in fabrication of surface composite reinforced with 1 $\mu\text{m}$  SiC in AZ31 matrix by FSP. Li et al. (2013) also found that some of the  $\sim 5.5 \mu\text{m}$  sized TiC reinforcement particles were reduced to nano-size after one pass of FSP in fabrication of TiC/Ti-6Al-4V surface composite. SiC particles cluster in shoulder affected zone is also shown in Fig. 4.9 (d).



**Fig. 4.9:** Optical images of SiC particles reinforced AA2014 surface composite (a) macrograph of transverse section (b) clustering of SiC particles in material flow lines (c) uniform distribution of SiC particles (d) clustering of SiC particles in shoulder affected region

Representative optical macrograph and micrographs of transverse section of TiC reinforced AA2014 surface composite are provided in Figs. 4.10 (a-c). Fig. 4.10 (a) shows macroscopic view of microstructural zones. Clustering of TiC particles occurs in the material flow region and shoulder affected region. Fig. 4.10 (b) shows particle enriched bands in the surface composites. The distribution of TiC particles in SZ is uniform (Fig. 4.10c). The average grain size in the SZ is found to be 6  $\mu\text{m}$ . The large reduction in grain size of TiC/AA2014 surface composite as compared to SiC/AA2014 is due to finer size of TiC particles. The average particle size of SiC and TiC were 30  $\mu\text{m}$  and 4  $\mu\text{m}$ , respectively. The finer reinforcement particles produce a pinning effect and restrict grain growth resulting in finer grain size.



**Fig. 4.10:** Optical images of TiC particles reinforced AA2014 surface composite (a) macrograph of transverse section (b) TiC particles enriched band (c) uniform distribution of TiC particles

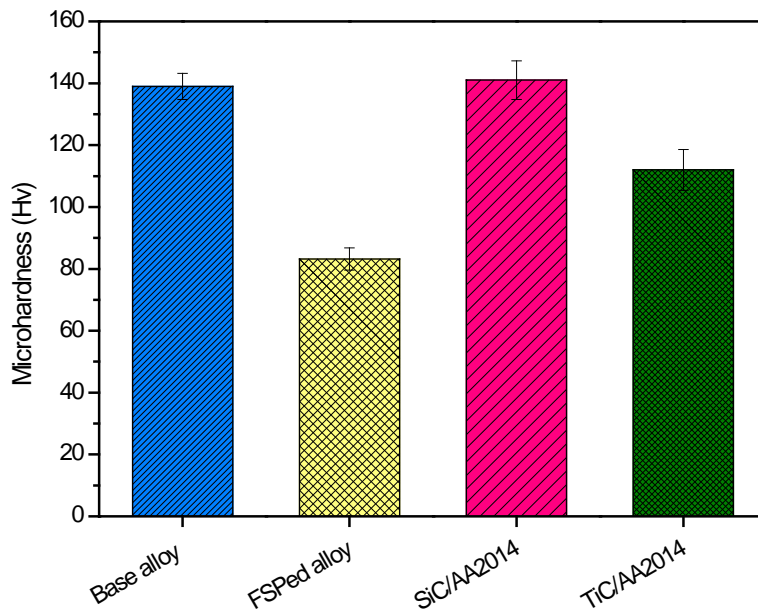
### 4.3.2 Mechanical behavior

#### 4.3.2.1 Hardness:

The microhardness values of the base alloy, FSPed alloy and surface composites are presented in Fig. 4.11. The hardness of the FSPed alloy decreases as compared to base alloy due to microstructural softening, as discussed previously. The average hardness of SZ in SiC/AA2014 surface composite is 141 Hv which is similar to average hardness of base alloy of 139 Hv. On the other hand, a lower average hardness of 112 Hv is obtained for SZ of TiC/AA2014. However, as compared to the hardness of FSPed alloy, the FSPed surface composites exhibit



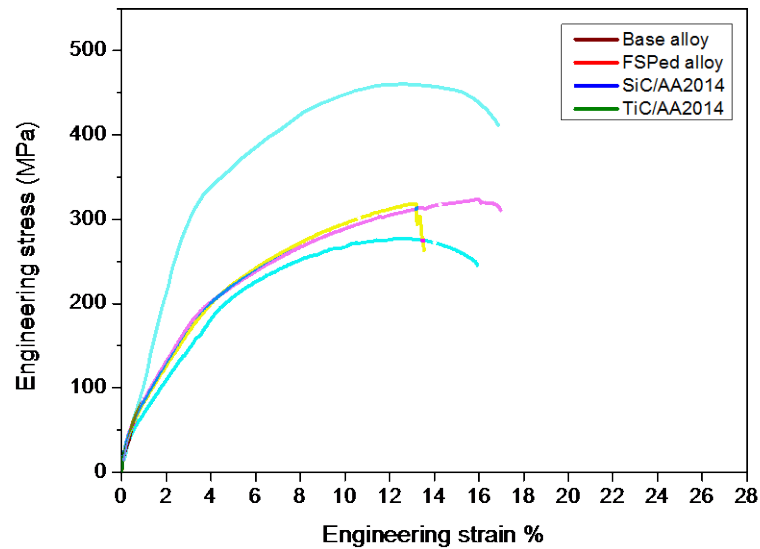
superior hardness. The harder SiC particles impart more hardness as compared to less harder TiC particles.



**Fig.4.11:** Comparison of microhardness of base alloy, FSPed alloy, SiC/AA2014 and TiC/AA2014

#### 4.3.2.2 Tensile strength:

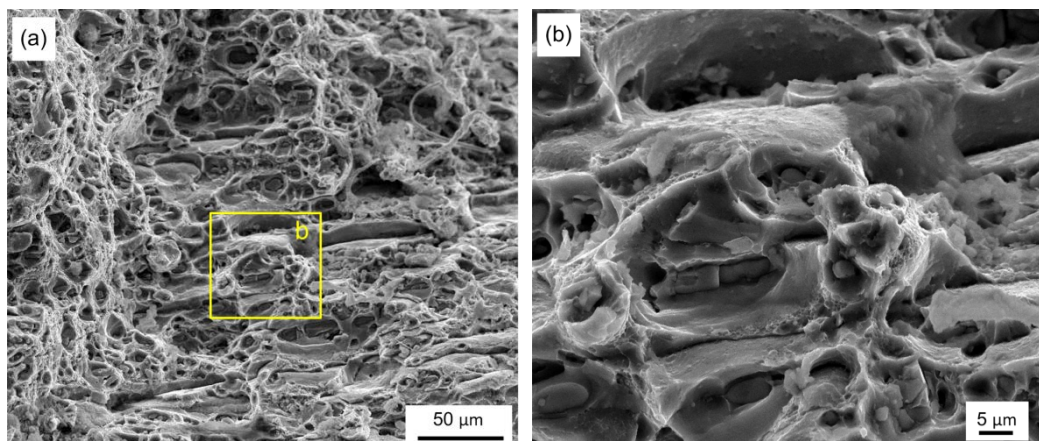
The engineering stress versus engineering strain curves of base alloy, FSPed alloy, SiC/AA2014 and TiC/AA2014 are shown in Fig. 4.12. FSPed surface composites and FSPed alloy show a nearly 40% decrease in ultimate tensile strength (UTS) as compared to base alloy. The decrease in strength is ascribed to the microstructural softening after FSP as base alloy is in T651 condition. Numerous studies report microstructural softening of T6 aluminum alloy and decrease in strength after FSP or FSW (Woo 2007; El-Rayes and El-Danaf, 2012). The UTS of SiC/AA2014 is almost similar to that of TiC/AA2014 surface composites. On the other hand, ductility is higher for base alloy. The less ductility in surface composite is ascribed to the early void nucleation at reinforcement particles (Manigandan 2012). However, higher ductility of TiC/AA2014 than SiC/AA2014 is due to finer size of TiC particles. Similar percentages elongation of 16-17 is obtained for base alloy, FSPed alloy and TiC/AA2014, whereas SiC/AA2014 shows percentage elongation of 13.5.

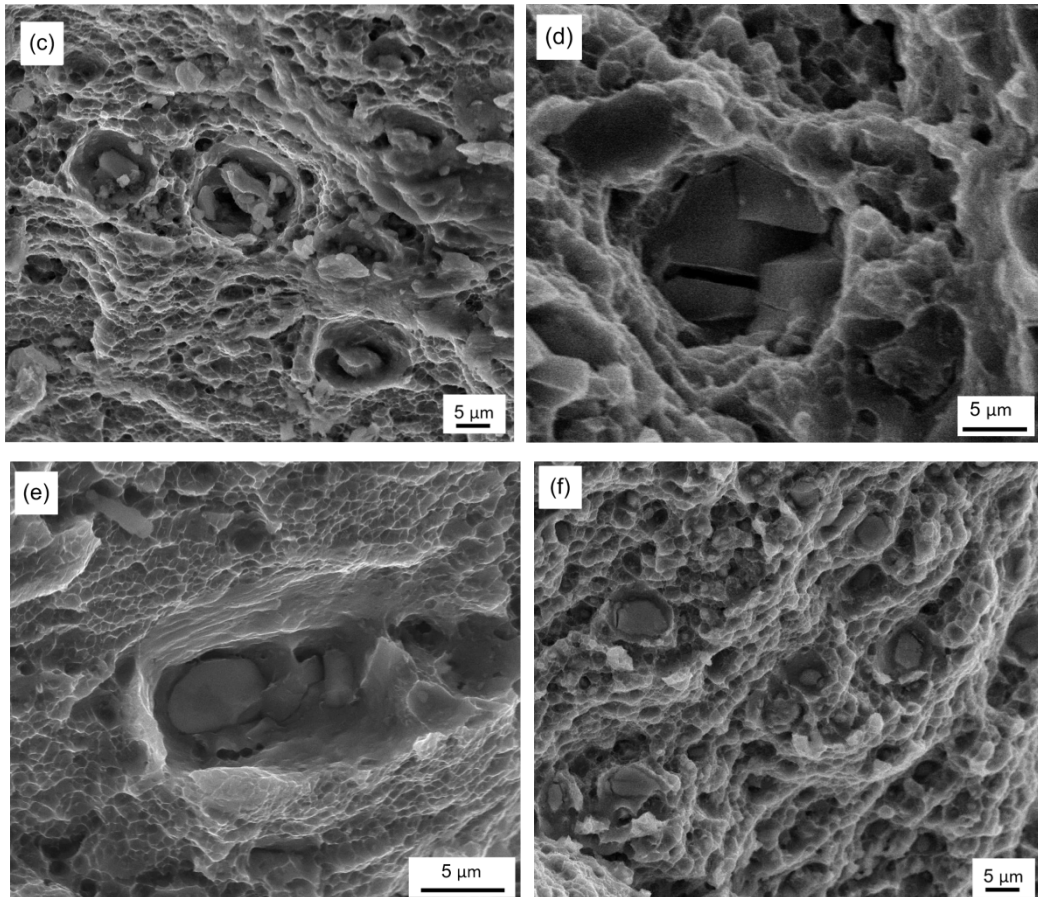


**Fig.4.12:** Stress-Strain curve of base alloy, FSPed alloy, SiC/AA2014 and TiC/AA2014

#### 4.3.2.3 Fracture surface:

Representative SEM images of fracture surfaces of base alloy, FSPed base alloy, SiC/AA2014 and TiC/AA2014 composites are shown in Figs. 4.13 (a-f). The fracture surface of base alloy shows large as well as small size dimples with tear ridges (Fig. 4.13 (a)). Unevenly distributed coarse and fine precipitates results in variations in dimple size. A magnified micrograph of marked region in Fig. 4.13 (a) is shown in Fig. 4.13 (b). Smooth walls without ripples and cracked precipitate are observed in a larger void. The void ligament is smooth indicating shear failure of the ligament. Fig. 4.13 (c) shows large and small size microvoids in the fracture surface of FSPed alloy. The fracture surface of SiC/AA2014 surface composite is shown in Figs. 4.13 (d and e). Fig. 4.13 (d) exhibits particle cracking with small and large microvoids. The clustering of SiC particles creates a large microvoid, as shown in Fig. 4.13 (e). The fracture surface of TiC/AA2014 exhibits ductile failure with small and large microvoids (Fig. 4.13f).





**Fig. 4.13:** Representative SEM images of fractured surfaces: (a) base alloy (b) magnified view of a region in (a) (c) FSPed alloy (d) SiC/AA2014 surface composite exhibiting particles cracking (e) clustering of SiC creates large microvoid in SiC/AA2104(f) TiC/AA2014 surface composite

#### 4.4 Summary:

The effect of four pass FSP in microstructure and mechanical characteristics of AA2014-T651 alloy is studied. The effect of SiC or TiC particles reinforcement in four pass FSPed AA2014-T651 alloy is discussed in terms of microstructure, hardness and tensile behaviour. The following is the major summary.

- (a) The SZ area after multi-passes FSP increases as compared to one pass FSP due to repetitive thermal cycles and deformation.
- (b) The as-received AA2014 average grain size of 125  $\mu\text{m}$  was refined to 12  $\mu\text{m}$  and 7  $\mu\text{m}$  after one pass and multi-passes of FSP, respectively.
- (c) The multi-pass FSP specimen exhibits low average hardness of 82 Hv as compared to base alloy average hardness of 137 Hv. However, the average hardness of one pass FSP specimen is found to be 112 Hv, which is higher as compared to multi-pass FSP.
- (d) The UTS also exhibits a decreasing trend from one pass to four passes of FSP. The tensile strength of as-received base alloy is 455 MPa for base alloy, while it is 369 and 278 MPa for the one pass and multi-passes FSPed specimens, respectively.
- (e) Regardless of significant grain refinement after FSP, the hardness and strength exhibits a decreasing trend with increasing number of passes. The decrease in hardness and strength after multi-passes of FSP is due to overaging of precipitates as base alloy is in T-6 condition. It can be concluded that hardening contribution by precipitates is dominant as compared to grain refinement contribution.
- (f) The SiC/AA2014 and TiC/AA2014 surface composites strength and hardness increases as compared to FSPed alloy without reinforcement particles. However, there is no significant difference in average hardness of SiC/AA2014 surface composite (141 Hv) as compared to base alloy average hardness of 137 Hv.

(g) The TiC/AA2014 surface composites show the average hardness of 112 Hv which is lower as compared to base alloy hardness. The harder SiC particles provide more hardness as compared to TiC particles.

# Friction stir processing strategies to achieve uniform distribution of reinforcement particles in surface composites

## Chapter-5

---

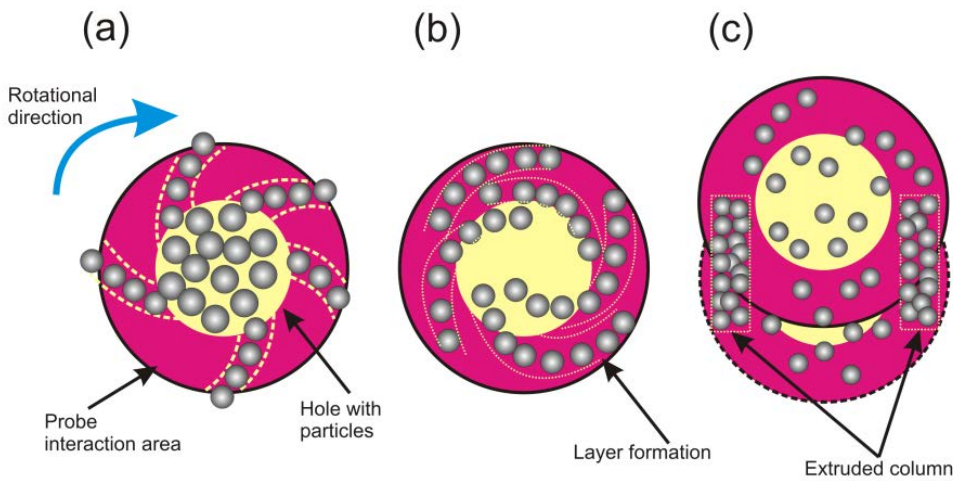
*In friction stir processing, fabricating defect free surface composites with uniform particle distribution is a challenging task. An attempt is made in the present investigation, to elucidate various FSP approaches in achieving uniform distribution of SiC particles in AA5083 alloy. Tool offset, multi-step FSP with a dual tool and rotational speed strategies are mainly discussed in correlation with the distribution pattern of reinforcement particles.*

### 5.1 Background

To fabricate a defect free surface composite and achieve uniform distribution of reinforcement particles, various approaches of FSP have been utilized (Gandra 2011; Sharma 2015; Izadi 2013; Akarmifard 2014). Asadi et al. (2010) demonstrated that a homogeneous microstructure can be obtained in FSP of AZ91 alloy by changing the rotational direction of the tool after every FSP pass. In surface composite fabrication, FSP of three or four passes is reported to achieve uniform distribution of reinforcement particles (Khayyamin 2012). Tool probes with threaded, square or triangular profiles are commonly used in fabricating surface composites. A square probe profile produces more pulse/sec (pulses/s = rotational speed in seconds  $\times$  number of flat faces) as compared to a triangular probe profile, while no such pulsating action is observed in cylindrical, tapered or threaded probe profiles (Elangovan 2007). Mahmoud et al. (2009a) showed that a square probe resulted in a more uniform distribution of SiC particles compared to cylindrical or triangular shape probes in fabricating SiC/A1050-H24 surface composites. Huang et al. (2014) utilized direct FSP to achieve surface composite layer of SiC on AZ31 alloy matrix. When a hollow and probe-less tool pre-filled with SiC particles was used, particles flowed out through the hole of the tool. SiC particles were pressed into the workpiece during processing as the rotating tool traversed along the direction of processing. Salehi et al. (2014) fabricated functionally graded AA6061/SiC nano-composite via multi-step FSP utilizing two different tools. Miranda et al. (2013) used three different strategies for incorporating reinforcement in the workpiece. They studied FSP using a groove filled with reinforcement particles, a uniform layer of reinforcement particles placed on the

workpiece prior to FSP and a consumable rod of aluminium drilled with holes to accommodate reinforcing particles.

The general understanding on the flow and distribution of reinforcement particles in FSP is schematically represented in Fig. 5.1 (a-c). The reinforcement particles are subjected to centrifugal force and the particles are forced outwards, while few of them are trapped and crushed to a finer size. The forced particles are embedded in the softened matrix material. Alternate layers of reinforcement particles and matrix are formed during processing as particles and matrix material are stirred simultaneously in the SZ. As the tool traverses in the forward direction, the stirred material is extruded behind the tool and forms a processed zone. Reinforcement particles are extruded on both sides of the SZ, as shown in Fig. 5.1 (c). This can be ascribed to the change in direction of tool rotation after each pass of FSP. Thus, advancing side (AS) as well as retreating side (RS) are changed after every pass.

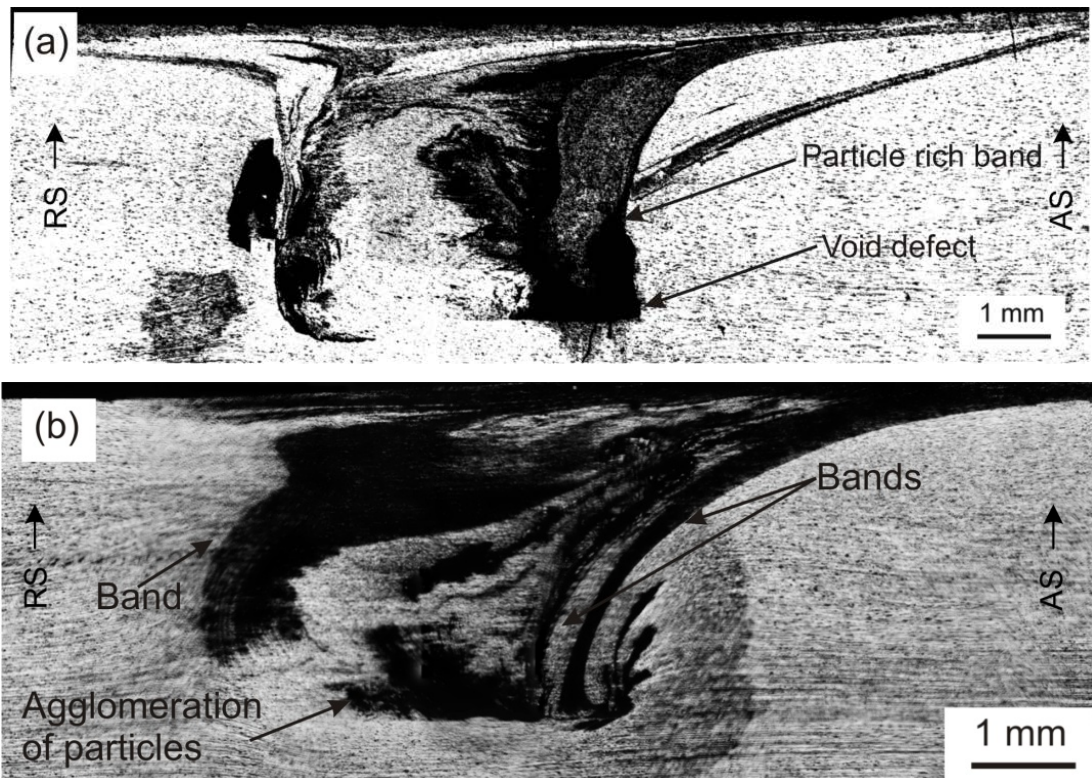


**Fig. 5.1:** Schematic top view of reinforcement particles distribution in FSP

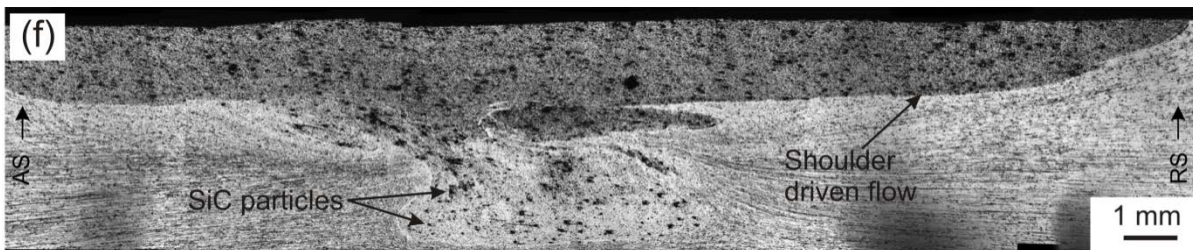
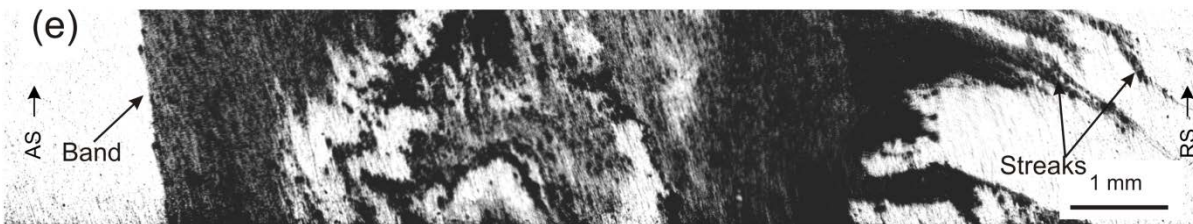
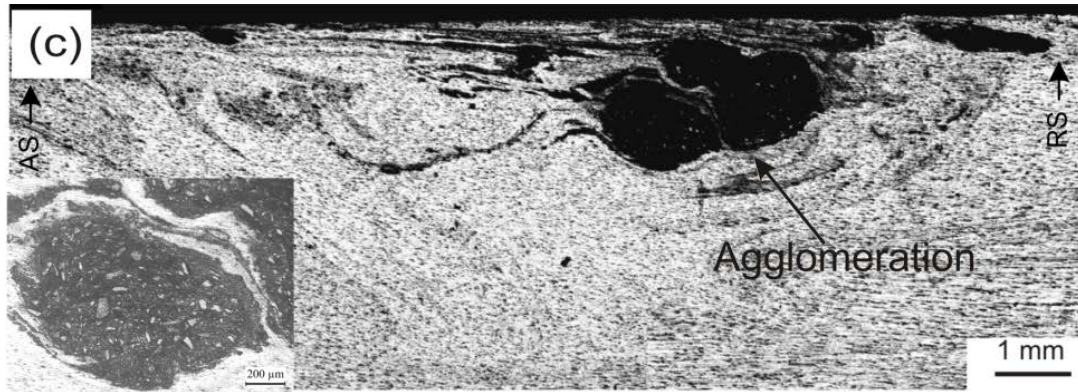
Achieving uniform distribution of reinforcement particles in the surface composites is quite a challenging task. As a part of the present thesis, SiC particles reinforced AA5083 alloy surface composite is fabricated using different friction stir processing strategies including (i) variation in process parameters (rotational and traverse speed), (ii) dual tool processing and (iii) tool offset over-lapping. The distribution pattern of SiC particles in the surface composites prepared by different FSP strategies is thoroughly discussed. The strong influence of FSP strategy on hardness of stir zone in surface composites is also demonstrated.

## 5.2 FSP with variation in rotational and traverse speeds:

Stitched optical micrographs of surface composites with different process parameters are shown in Figs. 5.2 (a-f). A micrograph of surface composite fabricated at low rotational speed of 1000 rpm and traverse speed of 25 mm/min exhibits poor flow of material in stir zone (SZ), as shown in Fig. 5.2 (a). Shahraki et al. (2013) observed that the distribution of ZrO<sub>2</sub> nano-particles in the SZ of AA5083 alloy was not uniform at a low rotational speed of 800 rpm or a high traverse speed of 160 mm/min. Low rotational speeds or high traverse speeds decrease the heat input and stirring of the material. A combination of low rotational speed and high traverse speed resulted in poor plastic flow of the material, agglomeration of particles, and the formation of porosities. Also, a void is found in the SZ of surface composite at 1000rpm and traverse speed of 25 mm/min (not shown). Barmouz et al. (2011) and Sharma et al. (2015) also demonstrated that only certain combinations of low traverse speed and high rotational speed result in uniform dispersion of reinforcement particles in surface composites.







**Fig. 5.2:** Stitched optical micrographs of surface composites fabricated by four passes of FSP at (a) 1000 rpm-25 mm/min (b) 1000 rpm-40 mm/min (c) 1400 rpm-25 mm/min (d) 1400 rpm-40 mm/min (e) top surface of 1400 rpm-40 mm/min (f) 2000 rpm-40 mm/min

Furthermore, agglomeration of reinforcement particles due to poor material flow is found in the lower part and near to the SZ-thermo-mechanically affected zone (TMAZ). Voids are also

observed at the root of SZ due to the flow of less material in processed zone. Material flow depends on heat input in the SZ and at lower rotational speed, heat generation is not sufficient. FSP at a rotational speed of 1000 rpm and a traverse speed of 40 mm/min results in banding and agglomeration of SiC particles, as shown in Fig. 5.2 (b). Insufficient material flow at low rotational speed also causes agglomeration of SiC particles. This can be understood from the extent of temperature rise in FSP. The maximum temperature ( $T_{\max}$ ) in the SZ can be estimated by Eq. 5.1 [5].

$$\frac{T_{\max}}{T_m} = K \left( \frac{\omega^2}{v \times 10^4} \right)^\alpha \dots\dots\dots (5.1)$$

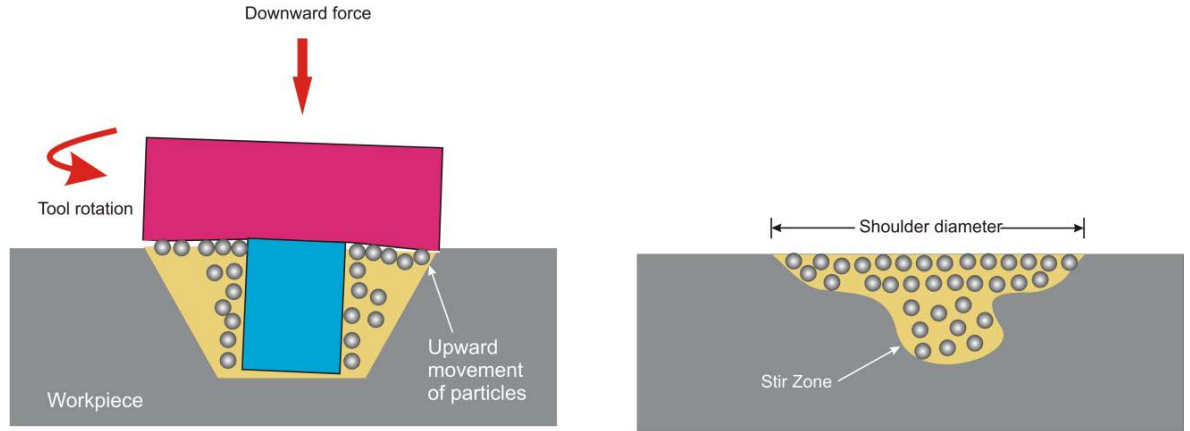
where the constant  $K$  is reported between 0.65 and 0.75,  $\omega$  is the rotational speed in rpm,  $v$  is the traverse speed in inch/min, exponent  $\alpha$  ranges from 0.04 to 0.06 and  $T_m$  is the melting point of the alloy in °C. Commonly, highest values for  $K$  and  $\alpha$  are used for peak temperature estimation. Peak temperature at a rotational speed of 1000 rpm and a traverse speed of 25 mm/min is calculated from Eq. 5.1 to be 502 °C. Peak temperature in SZ occurs at the top layer of workpiece near the probe of tool (Mahoney et al., 1998). The peak temperature is attained in first few seconds and then decreases as the tool passes away. This temperature is sufficient to soften the aluminum alloy but stirring is not effective to form a consolidated zone. Moreover, non-deformable ceramic particles hinder the material flow at lower rotational speed. Temperature in the SZ must be high enough to reduce the material flow resistance offered by SiC particles. In friction stir welding (FSW), the formation of a welded joint was attributed to both stirring and extrusion process (Colligan, 1996). Similarly, the flow of material in low rotational speeds is also governed by stirring action of the tool probe and extrusion of material.

At an increased rotational speed of 1400 rpm, the material flow enhances but agglomeration of reinforcement particles still exists, as shown in Fig. 5.2(c). In the upper part of SZ, agglomeration of reinforcement particles suggests their upward movement and trapping in the stagnant zone. However, in the lower part of SZ, there is uniform distribution of particles without any agglomeration. Azizieh et al. (2011) also pointed out that an increase in rotation speed enhances the material flow in the fabrication of  $Al_2O_3/AZ31$  composites. Asadi et al. (2011) reported that high rotational speed increased heat input, but nano-particles of alumina were homogeneously distributed due to shattering effect of rotation in the fabrication of  $Al_2O_3/AZ31$  surface composites.

In case of FSP at a rotational speed of 1400 rpm and traverse speed of 40 mm/min, uniform distribution of SiC particles in the center of SZ is obtained (Fig. 5.2d). Flow lines or bands enriched with SiC particles are also found at SZ-TMAZ boundary and in shoulder affected zone (SAZ). Repeated FSP passes with changing direction of tool rotation results in the formation of a distinct area beneath the shoulder and can be termed as shoulder dominated zone or SAZ. SAZ forms as the upper surface of workpiece comes in contact with the tool shoulder and subjected to extreme deformation and heat (Sato et al., 1999). Lorrain et al. (2010) also found SAZ in FSW of 7020-T6 aluminum alloy. They stated that frictional heat is mainly responsible for the thickness of SAZ and the top surface softened and stirred due to high temperature at shoulder/plate interface. The particles trapped in the material flow are not governed by the stirring action of the tool. The top surface of composites shows streaks and thick bands of reinforcement particles (see Fig. 5.2 (e)). The thick bands of reinforcement particles arise due to the extrusion occurring during processing.

At a high rotational speed of 2000 rpm and a traverse speed of 40 mm/min, uniform distribution of reinforcement particles is achieved, as shown in Fig. 5.2 (f). Material flow at higher rotational speed is dominated by shoulder flow, resulting in ~ 2 mm thick composite layer on the surface. Moreover, the composite layer is observed to extend to the influencing area of the shoulder (shoulder diameter), indicating shoulder driven flow of material. Kumar and Kailas (2008) pointed out that the material flow driven by both pin and shoulder is responsible for weld joint in FSW of aluminium alloy. The shoulder is the major source of heat and temperature is found to be highest at the top surface of the workpiece. According to Eq. 5.1, peak temperature with a rotational speed of 2000 rpm and a traverse speed of 40 mm/min is found to be 526 °C. A shoulder driven material flow dominates in the processed zone and reinforcement particles are uniformly distributed in the top surface. Reinforcement particles are uniformly distributed also in the SZ. However, less number of particles is observed in SZ as compared to SAZ.

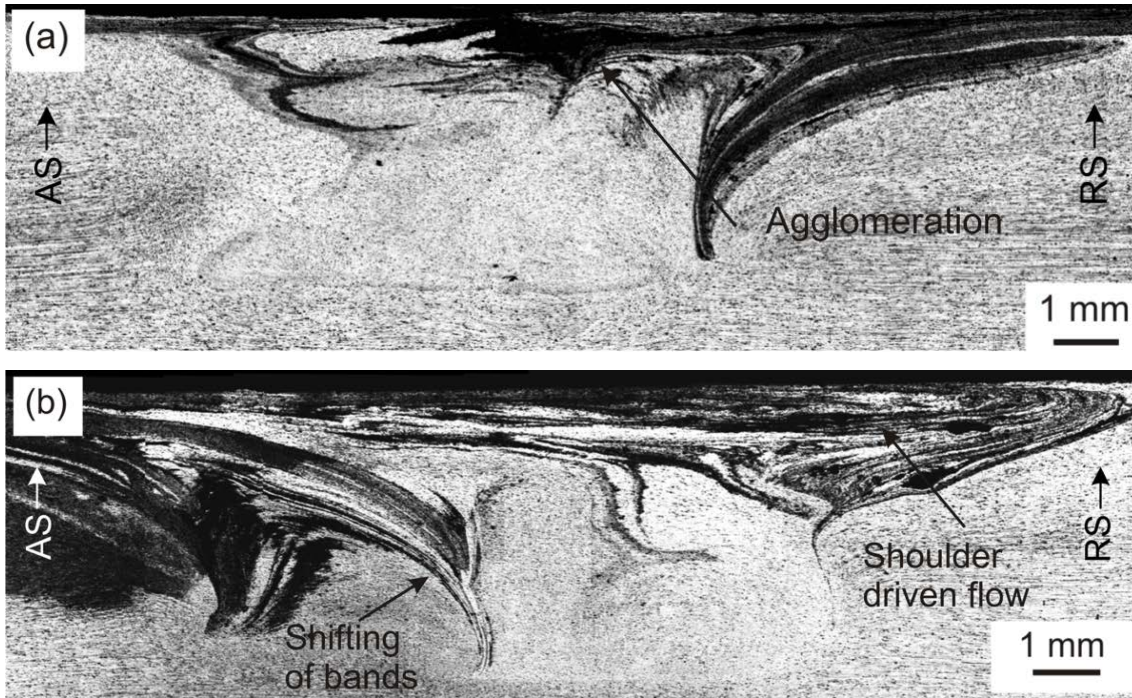
At higher rotational speed, the reinforcement particles move upward due to the intense stirring and being governed by shoulder driven material flow (Fig. 5.3). Interestingly, no extrusion like material flow is observed at high rotational speed, as observed at low rotational speed. In FSW of AA6061, Lee et al. (2004) observed that higher rotational speeds are necessary to force stirred material to the upper surface. So, it can be concluded that in dominance of shoulder driven material flow, the probe driven material flow and extrusion process are less operative for the investigated material.



**Fig.5.3:** Schematic cross sectional view of reinforcement particle distribution in FSP using high rotational speed

### 5.3 Tool offset overlapping

Banded feature in FSW is reported to form periodic deposition of processed material layers (Tongne et al., 2015), while minimum bands can be obtained by changing tool rotational direction (Asadi et al., 2012). In surface composites, bands are formed by alternate layers of reinforcement particles and alloy material. Such bands exist even after changing the tool rotational direction in the present study. To eliminate bands in the composite, a 50% overlapping pass of FSP (tool offset to half of probe diameter) on AS was applied after four passes of FSP. The overlapping pass of FSP completely eliminated bands in the lower part of the SZ, as shown in Fig. 5.4(a). However, bands still exist in the upper part. The stirring action of the rotating tool is not effective in the upper part due to the fact that material flow is governed by the shoulder. To understand the effect of overlapping passes, two 50% overlapping passes of FSP on RS with changing tool rotational direction were further conducted. As result, the band shifts as the tool offsets and two different bands are formed (Fig. 5.4b). The band in the lower part is eliminated due to overlapping multi-passes, similar to that observed after overlapping one pass. Thus, tool offset is effective to some extent in eliminating reinforcement particle bands.

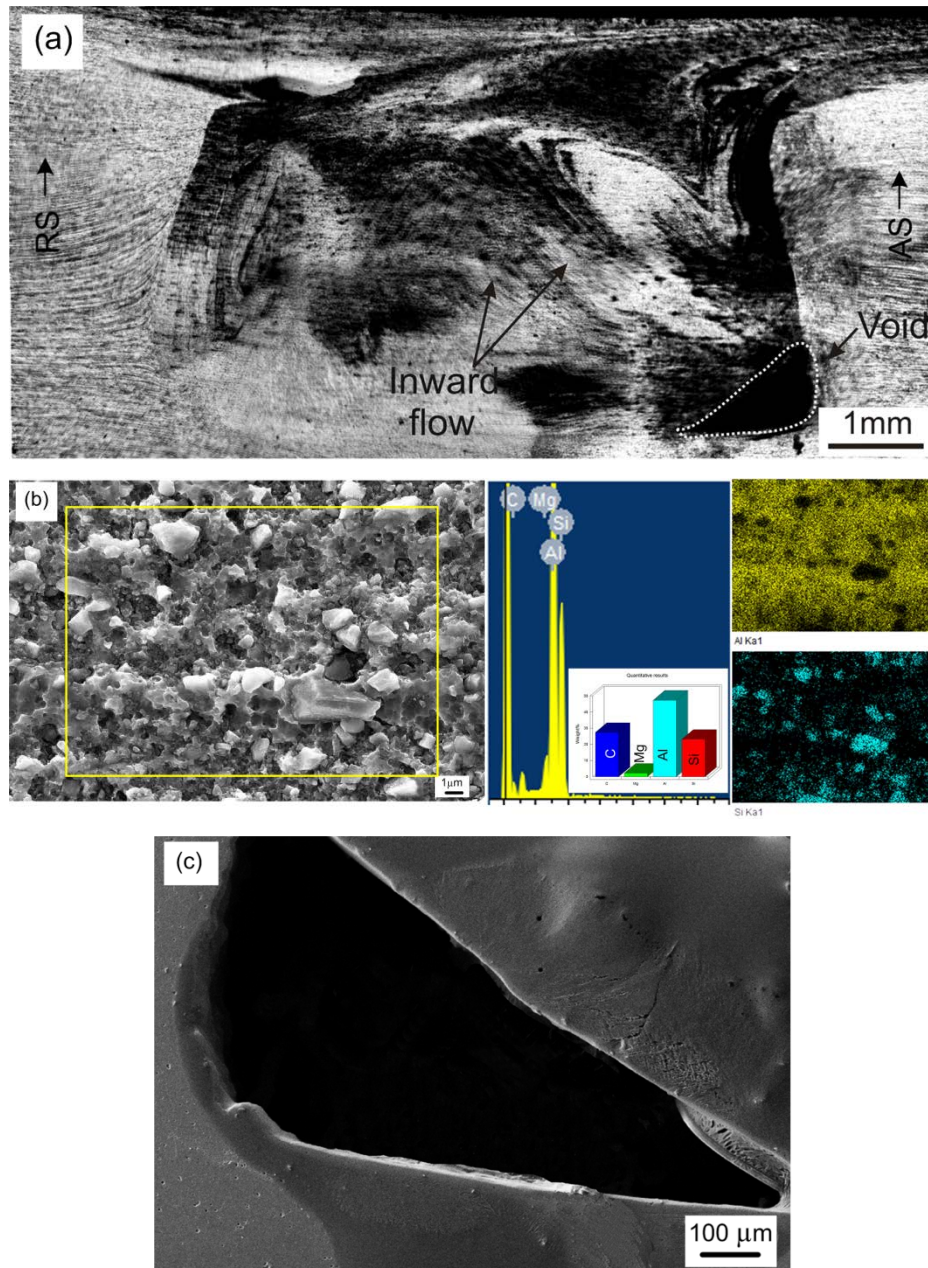


**Fig. 5.4:** Stitched optical micrographs of surface composites fabricated by tool offset overlapping passes at a rotational speed of 1400 rpm and a traverse speed of 40 mm/min. (a) one additional pass on previous four passes of FSP (b) two additional passes on previous four passes of FSP

#### 5.4 Dual tool processing

In other approach, a tool of bigger probe diameter i.e. 6 mm was utilized after four passes of FSP to eliminate bands of the reinforcement particles. Two additional FSP passes were applied at a rotational speed of 1400 rpm and a traverse speed of 40 mm/min by changing the tool rotational direction. The bigger probe diameter tool stirred the banded patterns at SZ-TMAZ interface in the lower part, but these patterns still exist in the upper right side region of the SZ (Fig. 5.5a). The SZ is occupied with the banded patterns and clustering of SiC reinforcement particles. EDS mapping of lower part of SZ of the surface composite fabricated by 6 mm diameter tool exhibits uniform distribution of SiC particles (Fig. 5.5b). Moreover, void arises in the SZ by using the bigger diameter tool (see Fig. 5.5c). This can be attributed to processing more material with the bigger probe diameter tool in the SZ. The estimated volume of processed material using the 6 mm probe diameter is 113.04 mm<sup>3</sup>, whereas the estimated volume using 5 mm probe diameter is 78.5 mm<sup>3</sup>. Thus, an increase of 1 mm in probe diameter results in 44% increases in processed material. As the pin diameter increases, more material is needed to fill the gap (Rai 2011). As the shoulder is the main source of heat, it can be understood that an increase in probe diameter decreases the shoulder

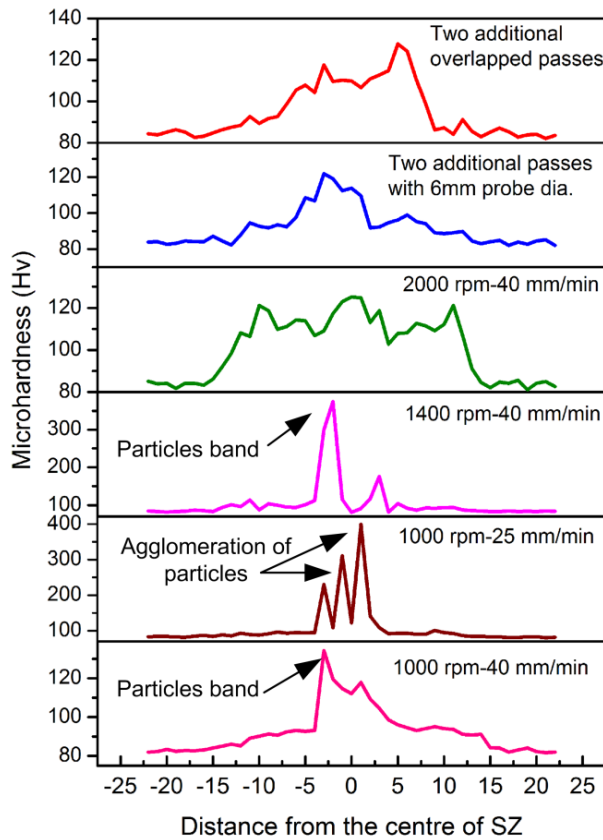
diameter which in turn results in less heat generation (Vijayavel 2014). In the present study, shoulder diameter was reduced by 1mm as probe diameter increased by 1 mm. The less heat generation adversely affects the material flow in a relatively more volume of processed material. In the condition of inadequate material flow, coalescence of material is insufficient to fill the gap in the processed zone.



**Fig. 5.5** (a) stitched optical micrographs of surface composites fabricated by two additional passes with the bigger diameter probe (b) EDS mapping of SZ processed by 6 mm probe diameter tool (c) void in SZ processed by 6 mm probe diameter tool

### 5.5 Hardness of surface composites

The microhardness of the surface composites is shown in Fig. 5.6. The microhardness data shows steep fluctuations due to agglomeration and bands of SiC particles. The uniform distribution of particles causes less variation in microhardness as found in surface composite fabricated at 2000 rpm and traverse speed of 40 mm/min. The average hardness found in this surface composite is 124 Hv, whereas the average hardness of base alloy is 82 Hv.



**Fig. 5.6:** Hardness variation of surface composites

The surface composite fabricated at a rotational speed of 1400 rpm and a traverse speed of 40 mm/min shows a maximum hardness of ~374 Hv in agglomerated SiC particles region. In surface composites fabricated at a rotation speed of 1400 rpm and a traverse speed of 40 mm/min, formation of bands in SZ causes rise in hardness. The surface composite after two additional passes with bigger probe diameter i.e. 6 mm shows a uniform microhardness in the SZ with the average microhardness of 116 Hv. After two additional passes, a uniform distribution of hardness is obtained in the overlapped side, whereas high hardness is observed in the banded region.

## 5.6 Summary

SiC particles reinforced AA5083 alloy surface composite was prepared using FSP strategies: Variation in rotational and traverse speeds, dual tool processing and tool offset overlapping. The following is the summary on the suitability of the strategy with respect to distribution of reinforcement particles.

- a) Bands of reinforcement particles are found at the lower rotational speed of 1000 and 1400 rpm, while no such bands are observed at higher rotational speed of 2000 rpm.
- b) Shoulder driven flow dominated at a higher rotational speed of 2000 rpm, whereas probe driven flow dominated with extrusion column is observed at lower rotational speeds of 1000 and 1400 rpm.
- c) At higher rotational speed of 2000 rpm, the surface composite with uniformly distributed SiC particles was extended to the complete area influenced by the shoulder.
- d) Post processing of the surface composite by a bigger diameter tool produces defects and particle distribution was also inhomogeneous.
- e) After tool offset passes, bands of reinforcement particles still exist but their position shifted accordingly to the tool offset.
- f) The overlapping passes by tool offset or high rotational speed are effective strategies to improve the distribution of particles.
- g) The overlapping passes by tool offset and high rotational speed are effective strategies in improving distribution of particles.





# **Fabrication and sliding wear behavior of ceramic and metallic particles reinforcement in friction stir processed surface composites**

## **Chapter-6**

---

*This chapter deals with the study of microstructural characteristics, mechanical properties and tribological behavior of surface composites reinforced with graphite and tin in LM24 alloy. The reinforcement of graphite and tin was done in equal wt. % proportion and surface composites were fabricated at two different rotational speeds of 1400 and 1000 rpm. The friction and wear characteristics were studied at 5 and 20 N loads against steel ball in ambient conditions.*

### **6.1 Background**

Al-Si alloys are suitable materials in several engineering applications owing to high strength to weight ratio, low coefficient of thermal expansion, high corrosion resistance and better wear resistance, but its microstructural features limit applicability as needle or acicular morphologies of silicon, porosity and intermetallics are detrimental to mechanical properties (Lados and Apelian 2004; Ma 2006). Presently, Al-Si alloys are extensively used in automotive applications because of their superior tribological and high temperature performance (Karthikeyan 2010). However, need for further enhancement in performance exists in order to increase engine efficiencies and develop material for harsh operating conditions.

FSP provides a synergistic effect of breaking-up acicular Si and decreased grain size in Al-Si alloys. Microstructural refinement in Al-Si alloys by FSP exhibited a significant improvement in mechanical properties (Sharma 2004; Karthikeyan 2010). Previous studies on FSPed Al-Si alloys have shown that the size of acicular Si particles can be decreased to submicron (Ma 2006). The incorporation of hard or soft reinforcement particles in Al-Si alloys by FSP to fabricate surface composites can further enhance the performance. Several reinforcements such as  $\text{Al}_2\text{O}_3$ , SiC,  $\text{B}_4\text{C}$ , TiC,  $\text{MoS}_2$ , graphite etc. are used for fabricating surface composite by FSP route. (Mahmood 2009b; Rejil 2012; Alidokht 2011; Devaraju 2012). The graphite is a common solid lubricant phase utilized in fabrication of surface composites as it reduces frictional forces and enhances tribological properties (Rohatgi 1992). Further, low melting point element tin provides a softer phase in aluminum. It is commonly added in moving automotive parts or bearing materials to

prevent seizure when system is running out of lubrication (Wu 2011). The tin is also known for its anti-welding characteristics with iron (El-Salam 2010).

Several studies are reported on friction stir processing of Al-Si alloys for surface modification and improvement in mechanical properties (Tsai and Kao 2012; Rao 2009; Ma 2006). Alidokht et al. (2011) studied tribological characteristics of surface composites of A356 alloys reinforced with SiC or MoS<sub>2</sub> particles via FSP route. They found that addition of lubricant particles MoS<sub>2</sub> enhances the wear resistance by forming a mechanically mixed stable layer. Mazaheri et al. (2011) investigated mechanical properties of surface composite fabricated by utilizing FSP on coated A356 alloy with micro and nano sized Al<sub>2</sub>O<sub>3</sub> particles. Their results showed that Al<sub>2</sub>O<sub>3</sub>/A356 surface nano-composite exhibited better hardness due to Orowan strengthening mechanism. Choi et al. (2013) studied mechanical properties of surface composite fabricated by FSP with reinforcement of silicon carbide (SiC) particles in A356 alloy. They reported that uniform distribution of SiC particles and spheroidization of Si needles results in improved hardness of the surface composite. Tutunchilar et al. (2012) utilized FSP to transform the surface of Al-Si alloy LM13 into a modified hypereutectic alloy by the addition of 10 vol. % Si particles. After FSP, the fracture mode changes from brittle to ductile as compared to the as-cast specimen due to grain refinement and breakup of needle-like Si particles.

There are limited studies on the tribological characteristics of FSPed surface composites of aluminum alloys reinforced with metallic reinforcement. In the present part of the thesis, graphite particles and tin (Sn) were reinforced in the Al-Si alloy LM24 by FSP route. Surface composites were prepared using graphite or graphite +tin reinforcement and rotational speed of 1000 rpm or 1400 rpm and traverse speed of 63 mm/min. The rotational speed was varied so as to obtain different heat input conditions. The surface composites are designated as surface composite A (reinforced with graphite; rotational speed 1400 rpm- traverse speed 63mm/min), surface composite B (reinforced with graphite and tin in equal amounts in terms of weight; rotational speed 1400 rpm- traverse speed 63mm/min), surface composite C (reinforced with graphite and tin in equal amounts in terms of weight; rotational speed 1000 rpm- traverse speed 63mm/min) and surface composite D (reinforced with graphite; rotational speed 1000 rpm- traverse speed 63mm/min). Designations of FSPed surface composites are also provided in Table 6.1. Further, the effect of graphite or graphite +tin reinforcement on sliding wear of LM24 alloy against steel ball is studied as function of rotational speed.

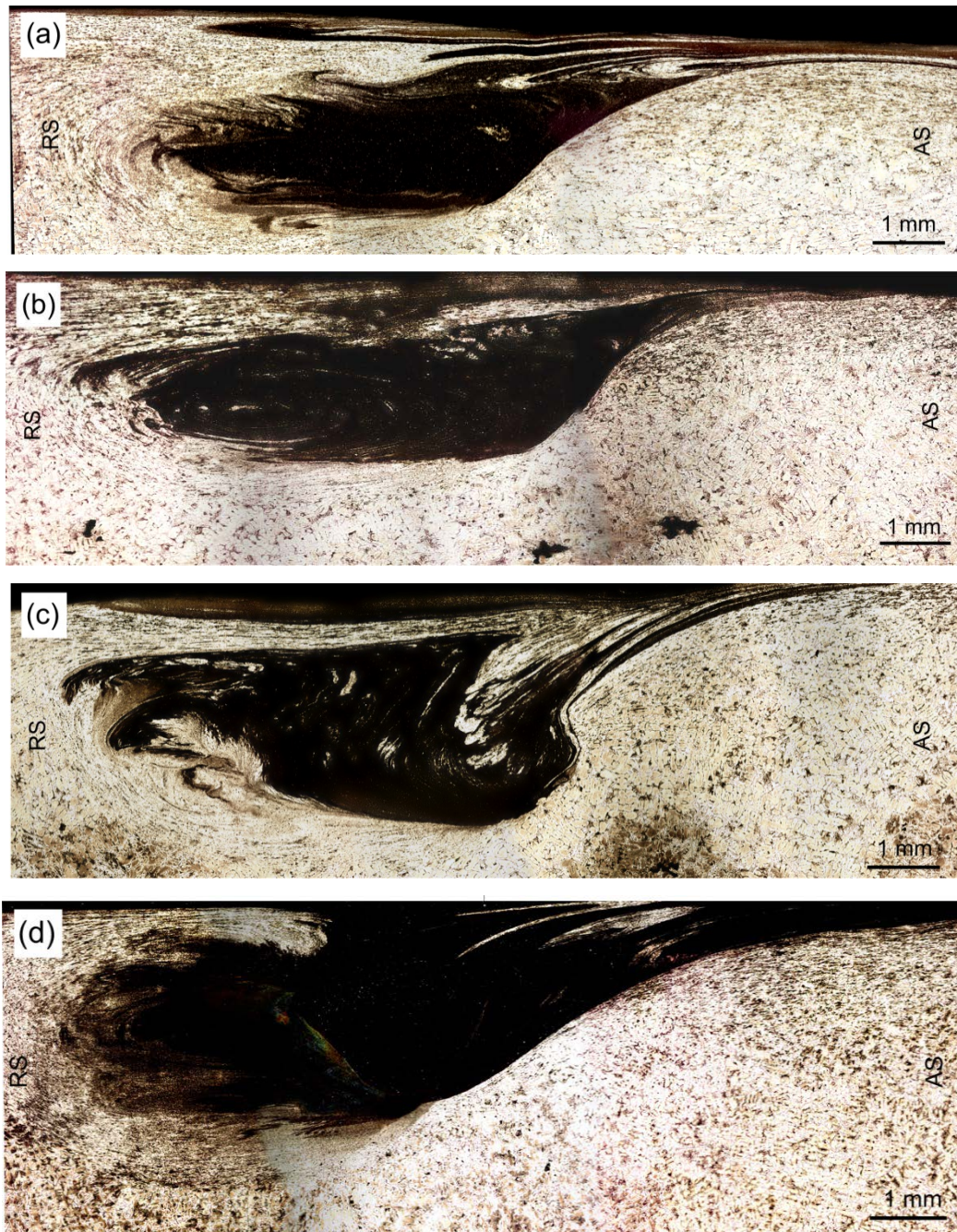
**Table 6.1:** Designation and details of reinforcement and tool speeds of LM24 surface composites

<b>Surface composite designation</b>	<b>Reinforcement</b>	<b>Rotational speed (rpm)</b>	<b>Traverse speed (mm/min)</b>
A	Graphite	1400	63
B	50 wt % Graphite + 50 wt % tin	1400	63
C	50 wt % Graphite + 50 wt % tin	1000	63
D	Graphite	1000	63

## 6.2 Results and Discussion

### 6.2.1 Macrographs

The macrographs of graphite or graphite + tin reinforced LM24 surface composites FSPed at 1000 rpm and 1400 rpm are shown in Figs. 6.1 (a-d). The SZ of all composites in general exhibit elliptical shape. Commonly, two types of nugget zones namely basin-shaped zone (widens near the upper surface) and elliptical shaped zone are found in FSW (Mishra 2005; Ma 2006). Sato et al. (1999) suggested that the top surface of workpiece experiences intense deformation and heating which resulted in the formation of a basin-shaped zone. Ma et al. (2006) found formation of a basin shaped nugget zone at lower tool rotation and an elliptical shaped zone at higher rotational speed in FSP of A356. The surface composites reinforced with tin shows a chaotic flow in SZ as similar to that observed in FSW of dissimilar alloys (Li 1999). Fig. 6.1 (a) shows the macrograph of surface composite 'A' with distribution of reinforcement particles in the SZ. The macrograph of surface composite 'B' is shown in Fig. 6.1 (b) exhibits an elliptical SZ with banding pattern on RS. The surface composite 'C' shows disorder or chaotic flow in SZ, as shown in Fig. 5.1 (c). Fig. 6.1 (d) shows the SZ of the surface composite 'D'.



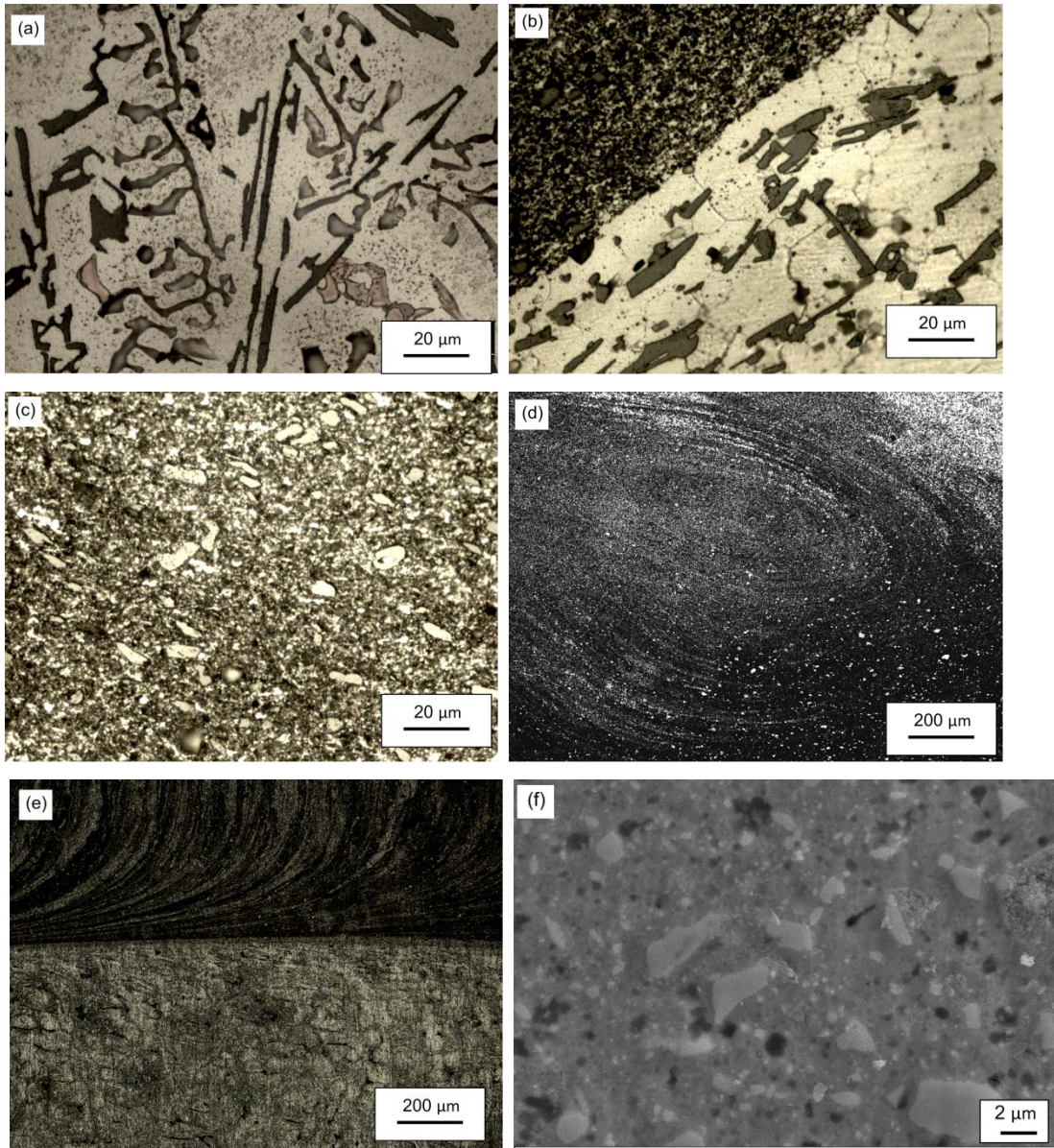
**Fig. 6.1:** The stitched optical micrographs of surface composite (a) A (b) B (c) C (d) D. Refer Table 6.1 for designation of surface composites

### 6.2.2 Microstructures

Microstructural features in each zone of the investigated friction stir processed surface composites are explained in this section.

### 6.2.2.1 Surface composite-A

The optical micrographs of base alloy and surface composite A is shown in Figs. 6.2 (a-e). The micrograph of base alloy is shown in Fig. 6.2 (a). Second phases in base alloy LM24 are eutectic silicon and primary silicon with intermetallic phases of  $\text{Al}_2\text{Cu}$  and  $\text{AlMnFeSi}$ . Fig. 6.2 (b) shows the SZ and adjacent TMAZ region of the surface composite. It is evident from Fig. 6.2 (b) that there is a significant transition in size of acicular or flaky silicon and grain refinement. The SZ micrograph of the surface composite A (shown in Fig. 6.2c) reveals the microstructural refinement and uniform distribution of graphite particles. The silicon size reduced to  $< 10 \mu\text{m}$  in SZ as compared to 20-60  $\mu\text{m}$  in the base alloy. The formation of onion ring in SZ is shown in Fig. 6.2 (d). Fig. 6.2 (e) shows the section of SZ cut along the processing line to visualize the formation of onion rings. The onion rings are commonly found in transverse sections of the FSP/FSW processed zone (Mishra and Ma 2005). Krishnan (2002) investigated the formation of onion rings in FSW of aluminium alloys. It was suggested that the onion rings are formed due to the extrusion of one layer of semi cylinder profile in one rotation of the tool. Fig. 6.2 (f) shows SEM image of SZ exhibiting submicron size of silicon.

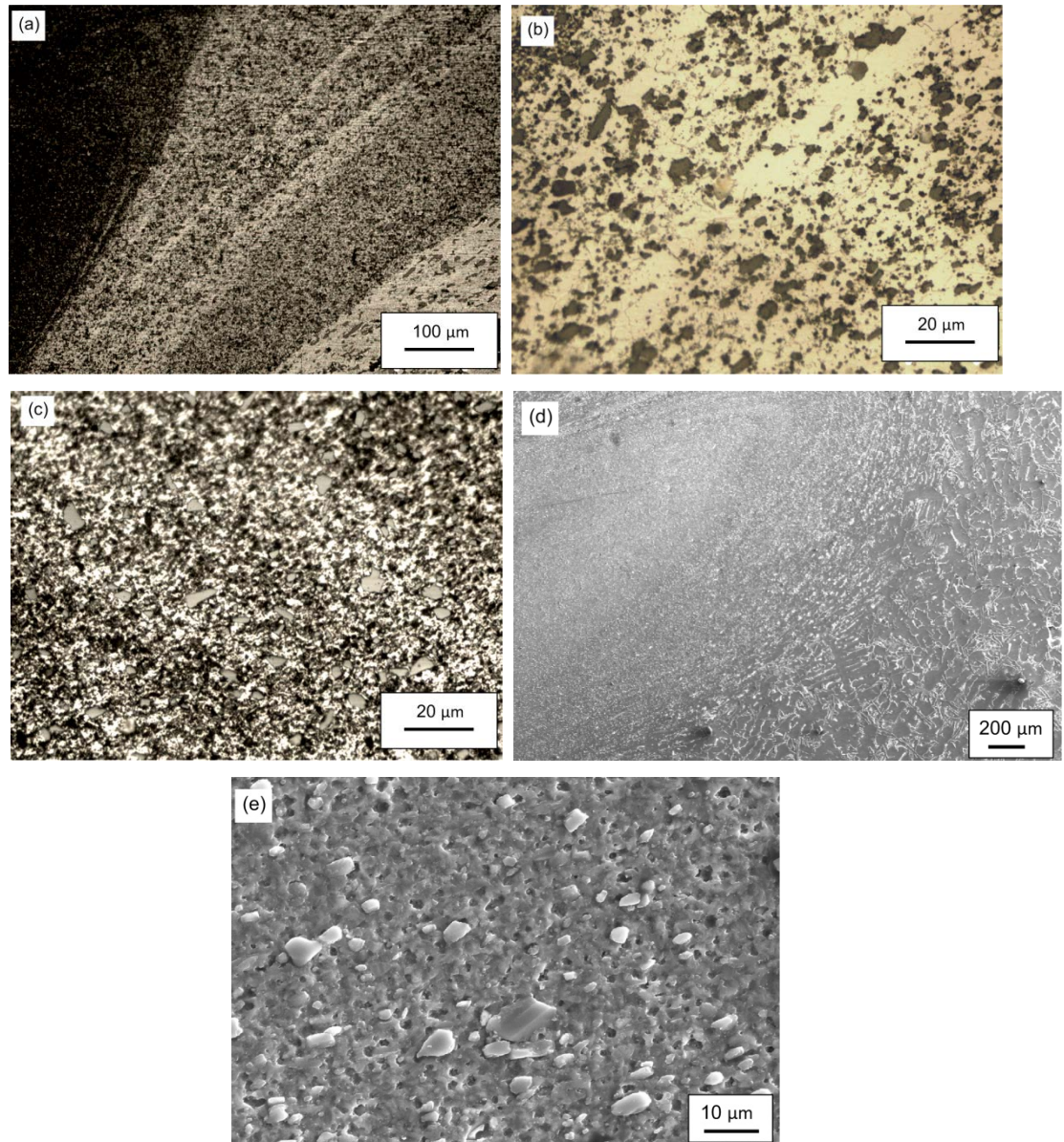


**Fig.6.2:** Optical and SEM images of (a) surface composite A (b) base alloy (c) SZ-TMAZ interface(d)SZ (e) onion ring in SZ sliced section along processing direction (f) SEM image of SZ

### 6.2.2.2 Surface composite-B

The optical micrographs of hybrid surface composite B is shown in Figs. 6.3 (a-c). Fig. 6.3 (a) shows SZ-TMAZ interface with alternative particle-rich and particle-free bands. A magnified view of the bands is shown in Fig. 6.3 (b). Cui et al. (2008) showed that the wavy flow pattern formed as a result of material flow from various locations in SZ. The SZ of surface composite B with uniform distribution of reinforcement particles is shown in Fig. 6.3 (c). SEM image of SZ-TMAZ interface

(Fig. 6.3d) indicate microstructural refinement in SZ, while that of SZ (Fig. 6.3e) shows refined silicon as well as uniform distribution of reinforcement particles.



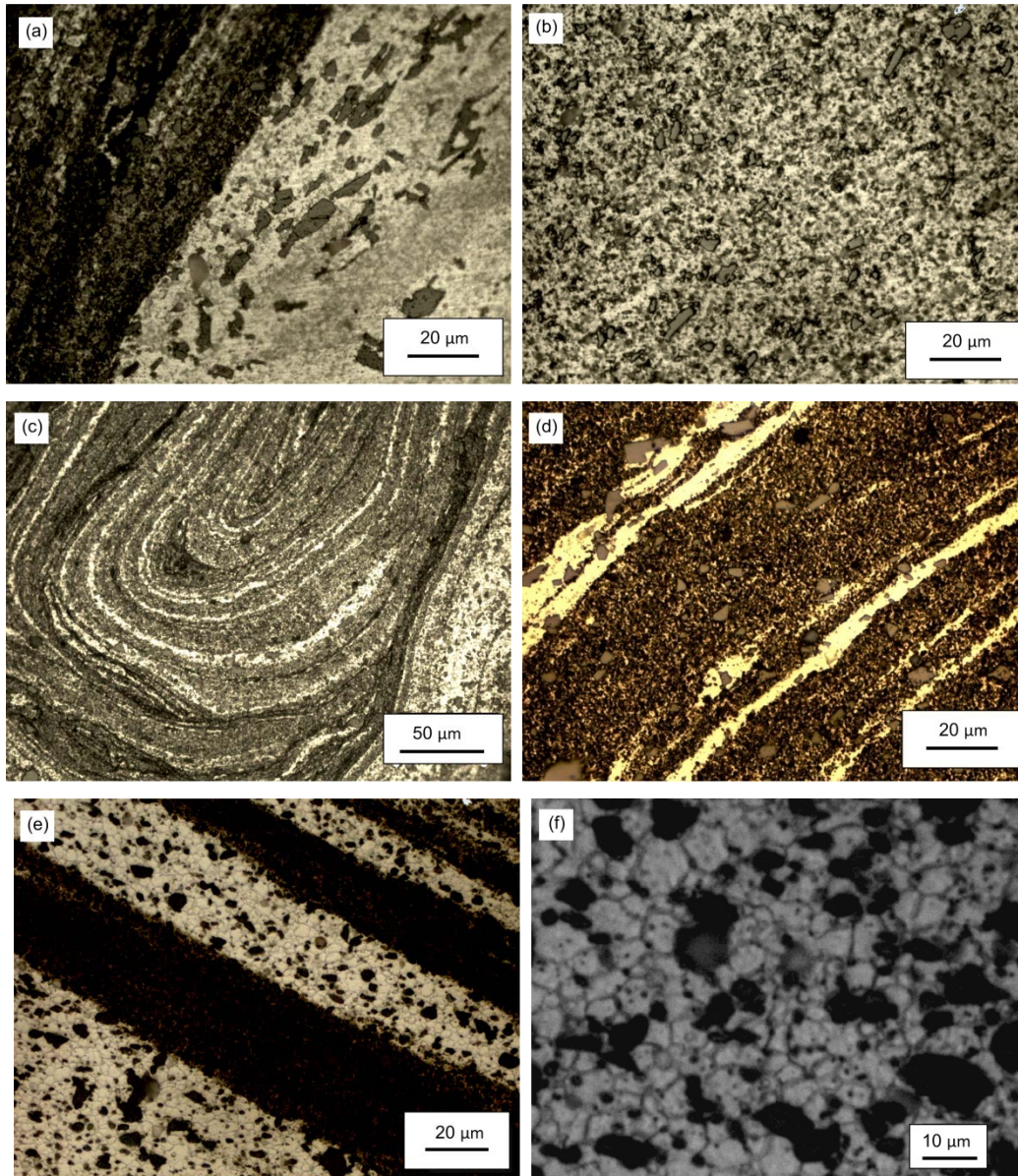
**Fig.6.3:** Optical and SEM images of surface composite B:(a) SZ-TMAZ interface (b) magnified view of bands in SZ-TMAZ interface (c) SZ (d) SEM micrograph of SZ-TMAZ interface (e) SEM image of SZ

### 6.2.2.3 Surface composite-C

The optical and SEM images of hybrid surface composite C are shown in Fig. 6.4 (a-f). The SZ-TMAZ interface of surface composite C is shown in Fig. 6.4 (a). The interface shows breakup of



acicular silicon and refined microstructure in the SZ. Fig. 6.4 (b) shows SZ of surface composite C exhibiting homogeneous distribution of second phases.



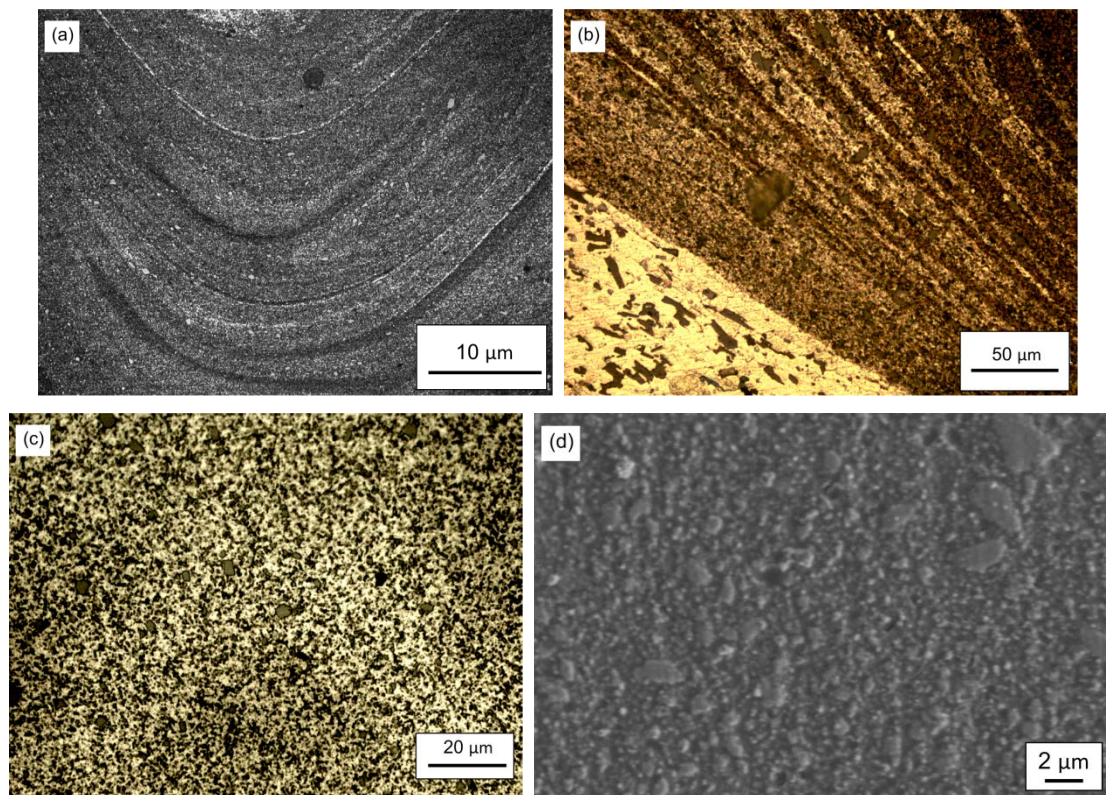
**Fig.6.4:** Optical images of surface composite C (a) SZ-TMAZ interface (b) SZ (c) onion ring pattern (d) bands on the RS of SZ (e) bands in material flow lines (f) magnified view of particle-free band region

The onion ring with alternative pattern of particle-rich and particle-free band is shown in Fig. 6.4 (c). These alternative patterns in the AS of SZ may be due to the addition of low melting point

reinforcement tin. The banded pattern is also observed on RS of the SZ (Fig. 6.4 (d)). In the AS of SZ, banded pattern of material flow lines is observed in Fig. 6.4 (e). The magnified view of the region of particle-free band exhibiting grain size  $< 5 \mu\text{m}$  is shown in Fig. 6.4 (f).

#### 6.2.2.4 Surface composite-D

The optical and SEM images of surface composite D are presented in Fig. 6.5 (a-d). Fig. 6.5 (a) shows the onion ring pattern of the SZ of surface composite D. The absence of tin in the reinforcement provides less variation or alternate layers in the onion rings, as observed in hybrid surface composites B and C. The banded pattern in the AS of SZ is shown in Fig. 6.5 (b). Fig. 6.5 (c) shows SZ of surface composite with uniform distribution of particles and microstructural refinement. The SEM image in Fig. 6.5 (d) shows the refinement of acicular silicon to even submicron size.



**Fig. 6.5:** Optical and SEM images of surface composite D (a) SZ-TMAZ interface (b) SZ (c) onion ring pattern (d) bands on the RS of SZ (e) bands in material flow lines (f) magnified view of particle-free band region

### 6.2.3 Hardness

The microhardness values of base alloy and surface composites are shown in Fig. 6.6. The average microhardness of base alloy is found to be 120 Hv. The surface composites exhibit microhardness in the range of 106-118 Hv. The reduction in microhardness of the surface composites as compared to base alloy is due to softer phases of reinforcement. Devaraju et al. (2013) reported that with the increase in graphite content, hardness decreases in hybrid surface composites (SiC+graphite/AA6061) fabricated by FSP. On the other hand, reduction in dislocation density was ascribed to reduction in hardness of Al-Si alloys after FSP (Tutunchilar 2012; Rao 2009). Rao et al. (2009) attributed decrease in hardness after one pass of FSP of Al-30%Si to low dislocation density in DRX grains.

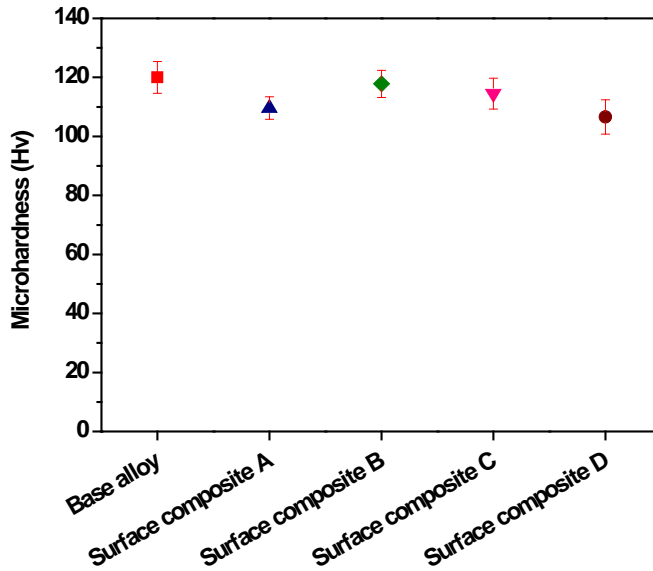
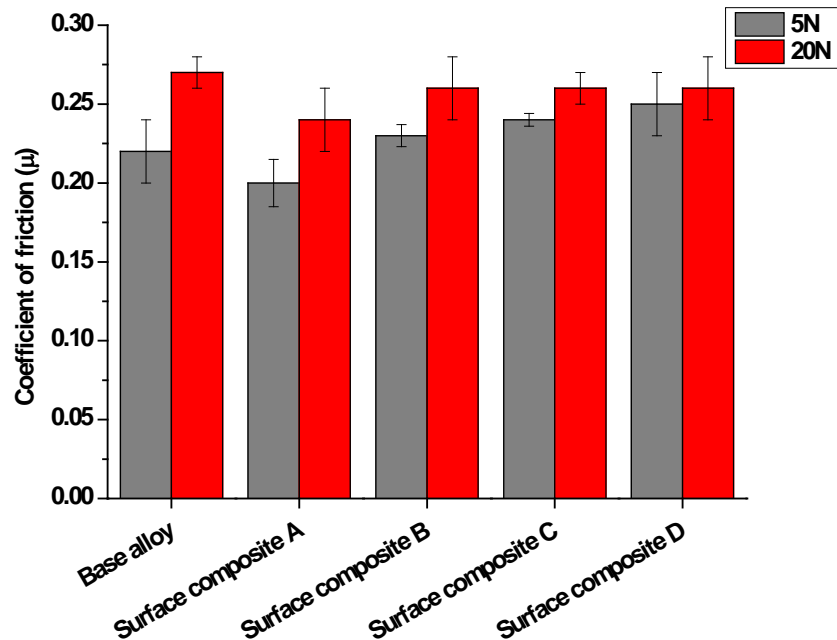


Fig. 6.6: Hardness of base alloy and surface composites

### 6.2.4 Friction characteristics

The coefficients of friction (COF) of base alloy and surface composites are presented as function of sliding load 5 N and 20 N are shown in Fig. 6.7. The COF for surface composites at a lower load of 5N varies from 0.20-0.24 whereas at a higher load of 20N, it varies from 0.23-0.26. For the base alloy COF is 0.22 at 5 N and 0.27 at 20N load. The presence of 100% graphite as a reinforcement provides a solid lubricating effect. However, surface composite D with similar percentage of graphite reinforcement but lower rotational speed has less material flow and results in non uniform distribution of particles. The significant effect of tin as a hybrid reinforcement on COF is not observed. In tribological study of graphite reinforced AA7075 composites,

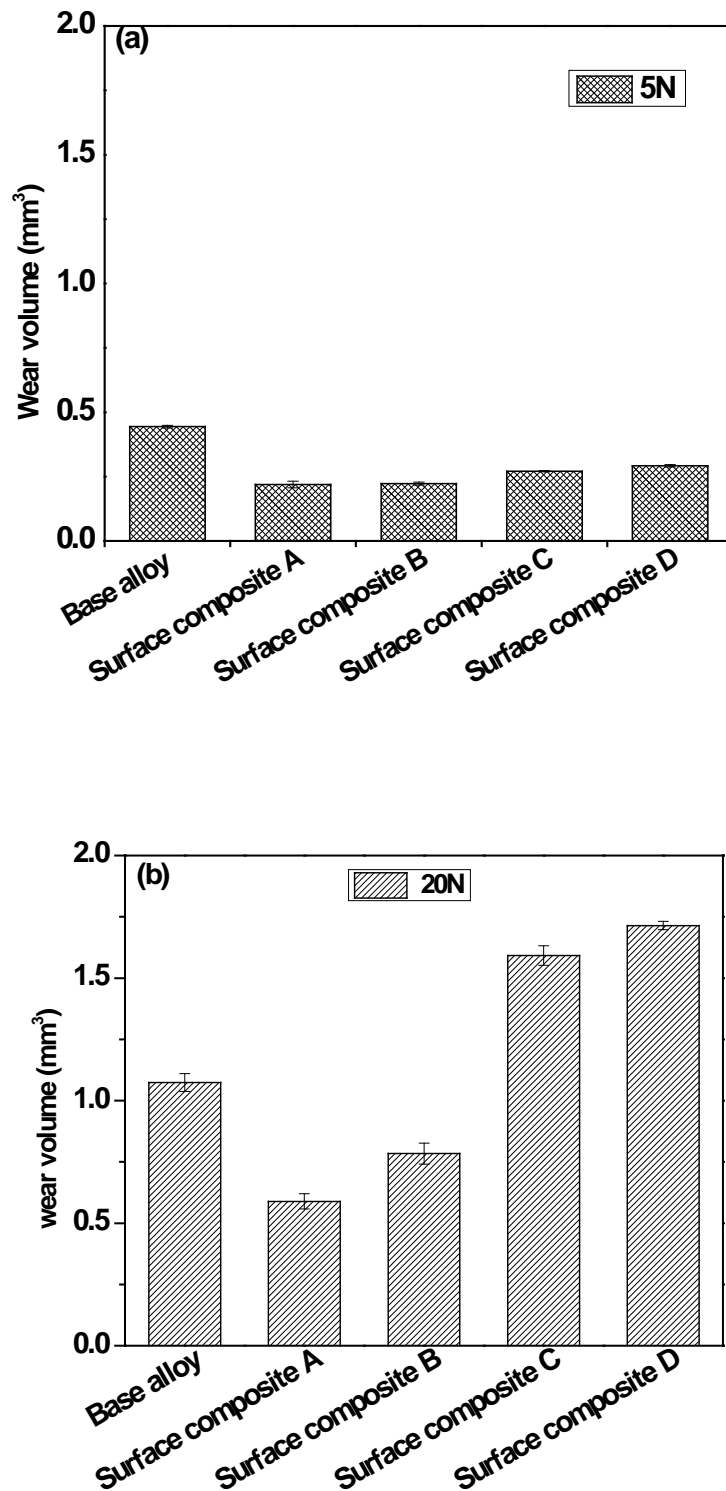
Bardeshwaran and Perumal (2014) found COF in the range of 0.2-0.25 with different weight percentages of graphite.



**Fig. 6.7:** Coefficient of friction of base alloy and surface composites at 5 N and 20 N load

### 6.2.5 Wear volume

The wear volume data for base alloy and surface composites is shown in Figs. 6.8 (a, b). Fig. 6.8 (a) shows the wear volume of base alloy and surface composites at 5 N load. The surface composites exhibit lower wear as compared to the base alloy. In surface composites, the surface composite A shows less wear due to lubrication effect provided by the graphite. At 20 N load, the wear volume increases significantly as shown in Fig. 6.8 (b). The surface composite A shows less wear as compared to other surface composites.

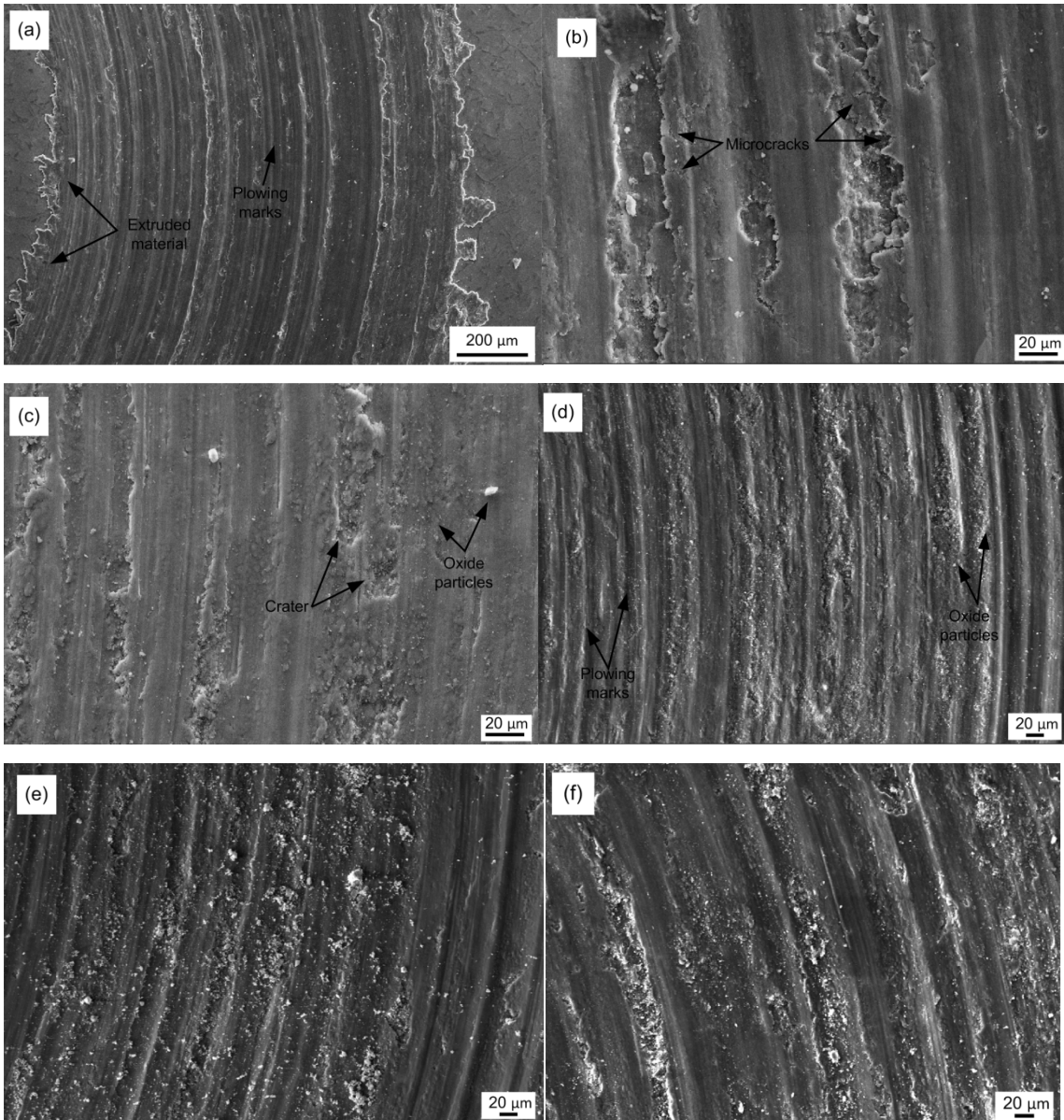


**Fig. 6.8:** The wear volume of base alloy and surface composites of LM24 after sliding against steel ball at (a) 5 N load and (b)20 N load

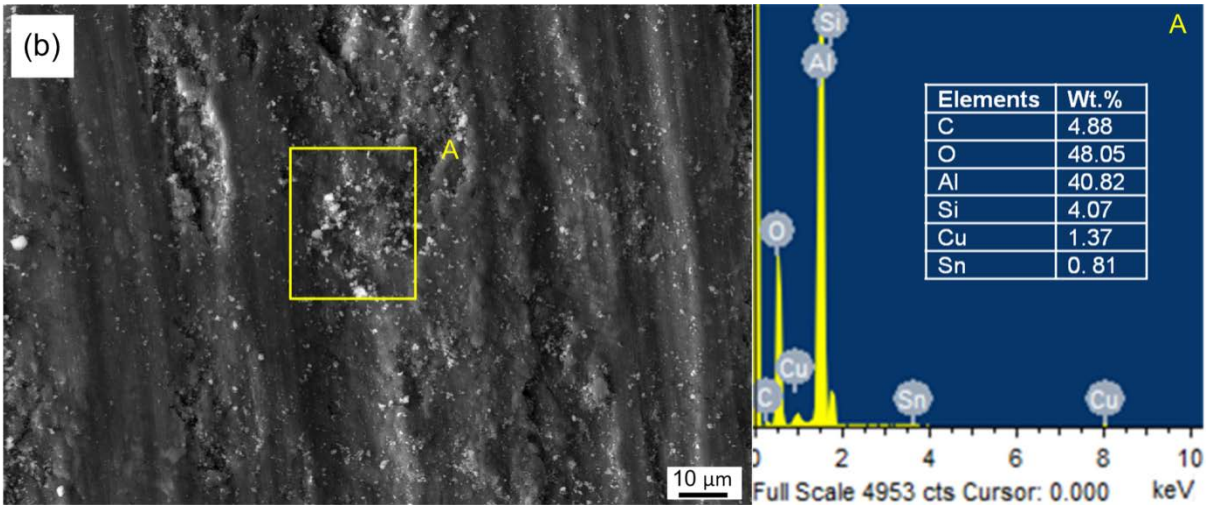
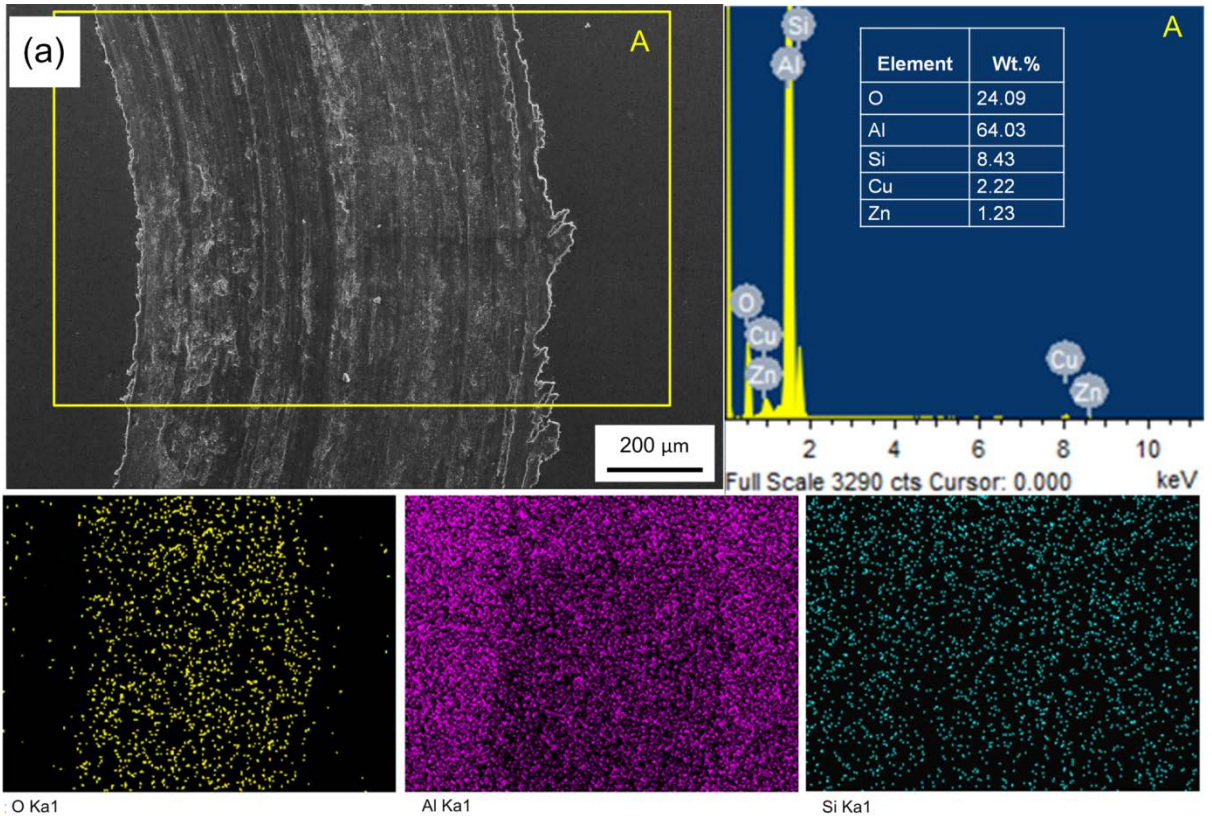
### 6.2.6 SEM-EDS analysis of surfaces worn at low load

The worn surfaces of the base alloy and surface composites at 5N load are shown in Figs. 6.9 (a-f). The worn surfaces of base alloy and surface composites reveal the flow of material. The asperities flatten at the contact and the material flows in the form of layers by ploughing action of the hard steel counterbody. The plastic flow of asperities along the sliding direction and in sideways of track is termed as flow wear (Akagaki and Kato, 1991). The layer formation with plowing marks in sliding direction and perpendicular to sliding direction in worn surface of base alloy (Fig.6.9a) exhibits flow wear characteristics. A magnified micrograph of base alloy worn surface shows microcracks in perpendicular direction of sliding (Fig. 6.9b). The presence of microcracks at the boundary of removed material suggests delamination wear as proposed by Suh (1973). Suh (1973) proposed that the plastic deformation nucleates subsurface cracks while these cracks propagate and interlink to generate plate like wear debris from the surface layer. The worn surface of surface composite A exhibits shallow plowing marks and deformation in form of layer, as shown in Fig. 6.9 (c). Craters are also observed indicating mild adhesion on the worn surface. The graphite induces a lubricating effect by forming a layer and avoids metal to metal contact. However, in absence of continuous layer, mild adhesion is likely to occur and material transfers on to the counterbody. Jerina and Kalin (2014) found early transfer of material in aluminum alloy and steel counter surface. Fig. 6.9 (d) shows worn surface of surface composite B in which shallow plowing marks with disintegrated oxide particles (bright features) are noted. These oxide particles are originated from the tribolayer or mechanically mixed layer (MML). It was well established that, during continued sliding, the initial transferred fragments of tribo-material are mechanically mixed i.e. deformed, fractured and blended, leading to the formation of mechanically mixed material (MML) on the sliding surfaces (Rosenberger 2005; Kalin 2014; Pogacnik and kalin 2013). The disintegrated wear particles with shallow and deeper plowing marks are observed in the worn surface of surface composite C (Fig 6.9e). The disintegrated wear particles act as abrasives or consolidateto form a MML. The deeper plowing marks are due to the abrasive action of the wear particles. Fig. 6.9 (f) shows worn surface of surface composite D. The presence of plowing marks and removal of material from the ridges of plowing marks are observed. The ridges protrude and make contacts with counterbody steel ball; so the material removal initiates from ridges. Typical EDS analysis of worn surfaces of surface composites is shown in Fig. 6.10(a-d). High oxygen content is found on the worn surfaces of all composites. The repeated sliding and removal of material accelerates oxidation process. The material from the counter body i.e. iron is found in

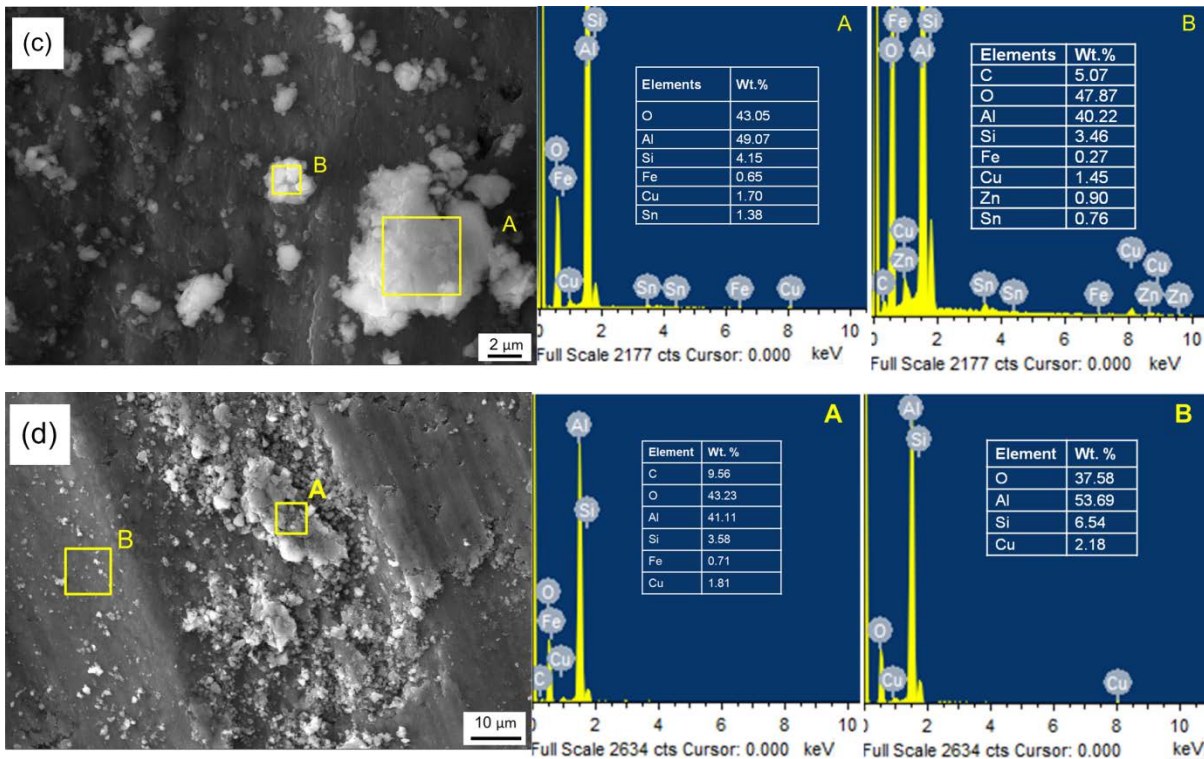
very less quantity (<1%) suggesting absence of MML at lower load of 5 N. After analyzing the worn surface at 5N load, it is concluded that at lower load plowing, oxidative wear and adhesive wear mechanism are operative in surface composites and plowing, adhesive and delamination wear are dominant in base alloy.



**Fig. 6.9:** SEM micrographs of worn surface of base and surface composites slid against 5N load (a) base alloy exhibiting flow wear (b) microcrack formation in base alloy (c) surface composite A (d) surface composite B (e) surface composite C (f) surface composite D



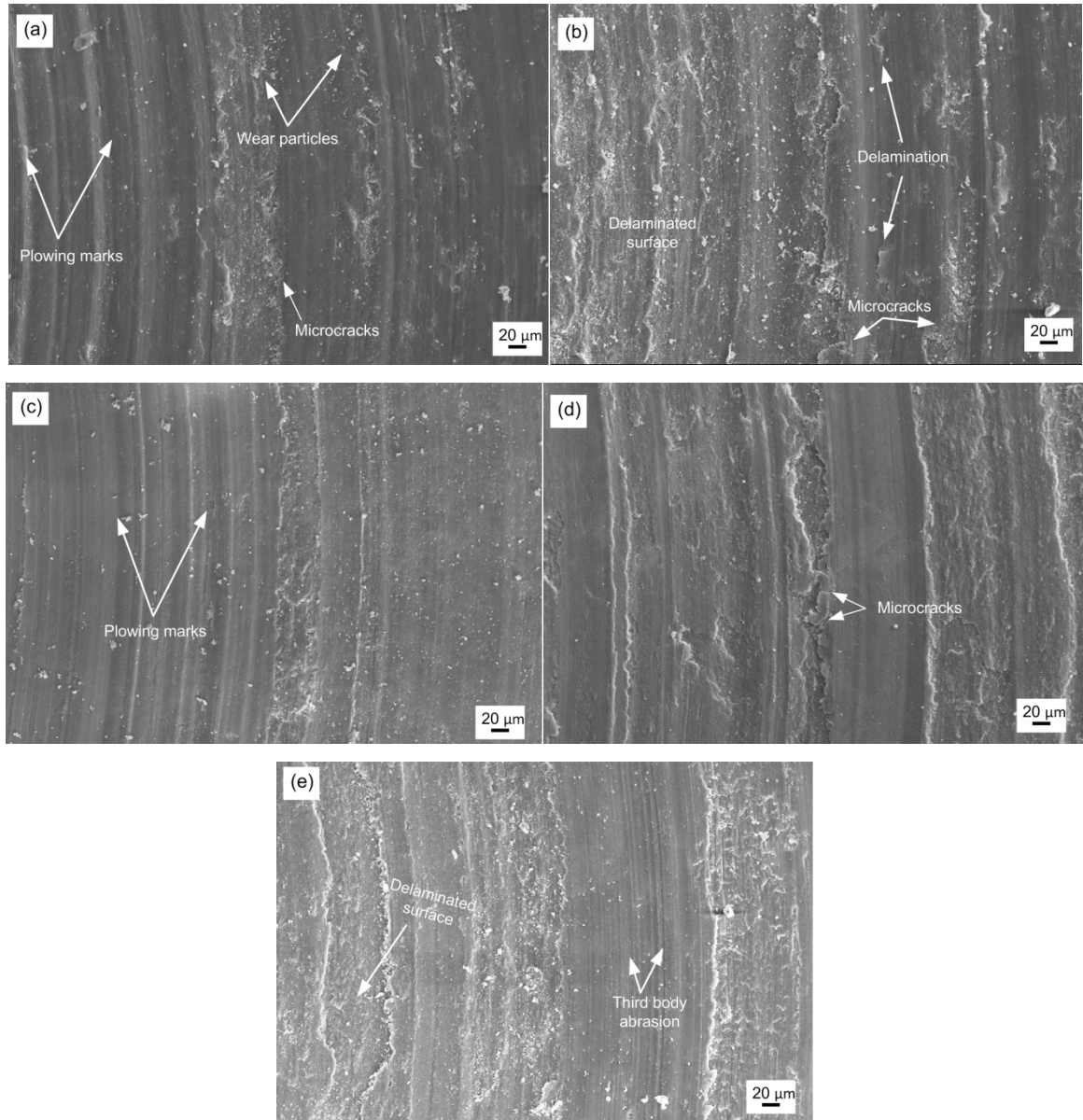




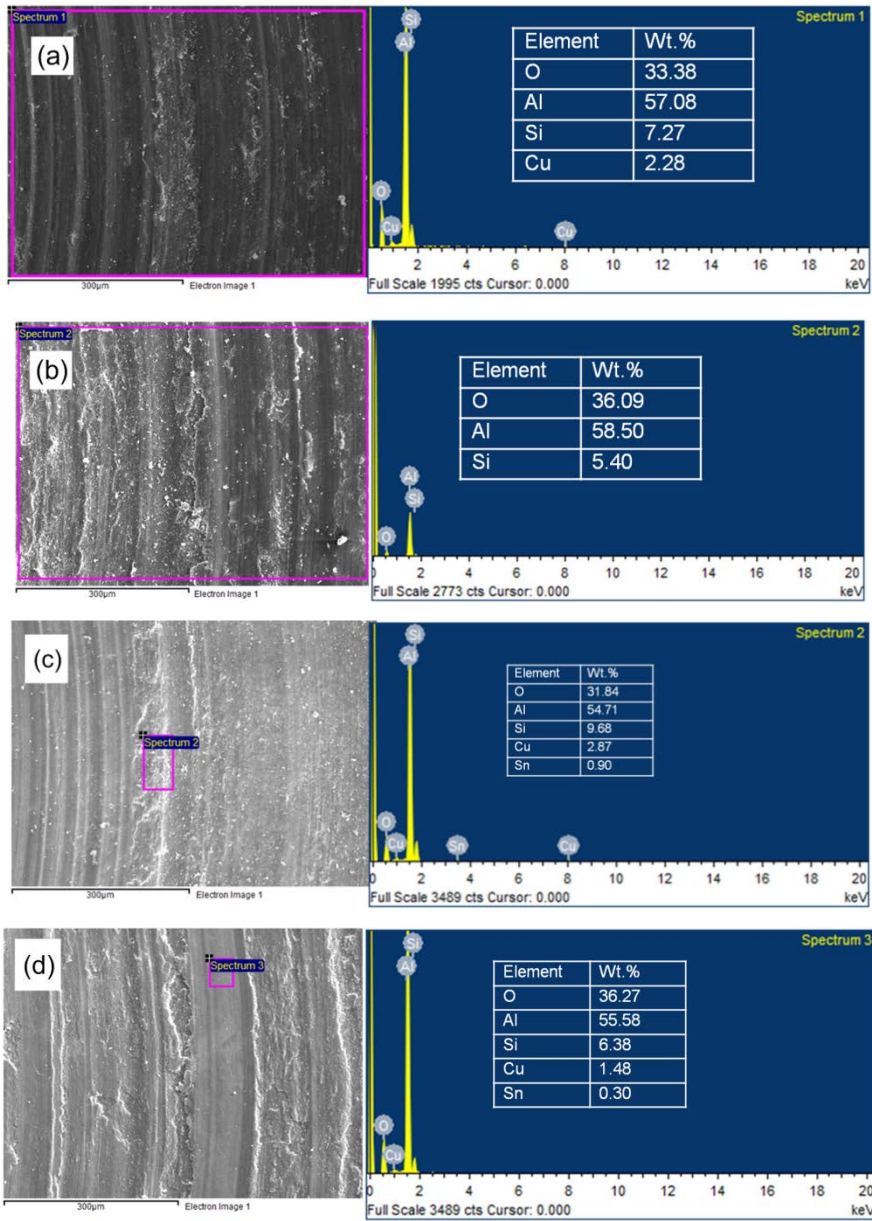
**Fig. 6.10:** EDS analysis of worn surface (a) surface composite A (b) surface composite B (c) surface composite C (d) surface composite D

### 6.2.7 SEM-EDS analysis of surfaces worn at high load

The worn surfaces of base alloy and surface composites at 20 N load are shown in Figs. 6.11 (a-e). The worn surface of base alloy exhibits deeper plowing marks and microcracks (Fig. 6.11a). At higher load of 20 N, the microcracks easily generate and interlink to provide large number of wear particles. The worn surface of surface composite A shows delaminated surface and a smooth surface with microcracks (Fig. 6.11b). It can be observed from the Fig. 6.11 (b) that a thin layer of material is formed and breaks by delamination. The worn surface of surface composite B reveals smooth and delaminated surface (Fig. 6.11c). The worn surface of surface composite C exhibits microcracks and delamination (Fig. 6.11d). The worn surface of surface composite D shows fine plowing marks indicating third body abrasion by trapped wear particles (Fig. 6.11e). The delaminated surface shows a continuous removal of material on the surface layer. The EDS analysis of worn surfaces of base alloy and surface composite are shown in Fig. 6.12 (a-d). The EDS analysis shows oxygen content suggesting oxidative wear, whereas the materials from counterbody i.e. iron is not found.



**Fig. 6.11:** SEM micrograph of worn surface of base alloy and surface composites at 20 N load (a) base alloy (b) surface composite A (c) surface composite B (d) surface composite C (e) surface composite D



**Fig. 6.12:** EDS analysis of worn surface of (a) base alloy (b) surface composite A (c) surface composite B (d) surface composite C

### 6.3 Summary

The influence of reinforcing of graphite or graphite and tin in LM24 alloy and two rotational speed (1000 or 1400 rpm) on microstructure and mechanical properties is studied. The tribological performance in unlubricated sliding conditions at 5 or 20 N load against steel ball is discussed as function of rotational speed and reinforcement. The following is the summary:

- a) Surface composites exhibit microhardness in the range of 106-118 Hv which is lower as compared to base alloy LM24 microhardness of 120 Hv. Marginal decrease in hardness is ineffective on tribological performance as FSP provides microstructural refinement and uniform distribution of reinforcement particles.
- b) The lubrication effect of graphite as reinforcement decreased wear. The surface composite A shows a low COF and wear as compared to base alloy and all other surface composites. Wear increased with increase in load.
- c) The wear and friction increased for the surface composite D reinforced with similar reinforcement of surface composite A i.e. graphite. The discrepancy in the tribological performance of surface composite D is due to low rotational speed of 1000 rpm as compared to rotational speed of 1400 rpm for surface composite A.
- d) The higher rotational speed provides more shattering effect and high input in the SZ, which enhances material flow.
- e) The worn surface analysis indicated that material transfer, abrasion, flow wear and delamination wear are dominated in base alloy, while abrasion and material transfer are observed in surface composites.



# Effect of counterbody hardness on sliding wear properties of friction stir processed surface composites

## Chapter-7

---

*In this part of the thesis, the effect of hardness of steel ball on friction and wear of FSPed  $Al_2O_3/AA5083$  surface composites in sliding wear conditions is discussed. To study the effect of counterbody hardness, the AISI 52100 steel balls are heated at different temperatures to obtain different hardness. The dominant mechanisms of material removal are elucidated as function of hardness of counterbody and sliding load.*

### 7.1 Background

Aluminum alloys are extensively used in engineering applications owing to high strength to weight ratio, and resistant to corrosion (Zohoor 2012). However, low hardness limits its applicability for tribological applications. To enhance tribological characteristics, ceramic particles are reinforced in aluminum alloys (Basu and Kalin 2011). Al-Mg based alloys and in particular AA 5083 alloy is widely used in automobile, transportation and marine applications due to excellent corrosion resistance, good weldability, high strength and formability (Hosseinipour 2009).

Surface composites are suitable materials in engineering applications where surface contact is involved. In such applications, the useful life of component mainly depends on the surface properties like hardness and wear resistance. Therefore, it is highly desirable that surface of the component exhibits desired hardness, while the substrate still maintains the original structure with good ductility and toughness (Mishra 2003; Zohoor 2012). Surface composites are fabricated by reinforcing matrix material with various reinforcement particles such as  $Al_2O_3$ , SiC,  $ZrSiO_4$ ,  $SiO_2$ ,  $B_4C$  etc. in micron or nano size (Khayyamin 2013; Arora 2011; Tang 2008; Sharma 2015) The alumina particles are widely used reinforcement in aluminum alloys due to thermal stability and cost effectiveness (Khayyamin 2013).

Wear mechanisms of metal matrix composites are known to be governed by several factors in a sliding wear system. Hard ceramic particle reinforcement plays a dominating role but formation and stability of mechanically mixed layer, humidity and counter body are also effective parameters

in influencing wear mechanisms (Rigney 1984). Mechanical and chemical interaction in tribosystem influences the friction and wear characteristics. The mechanical and chemical interaction in dry sliding tribosystem mainly depends on mechanical properties of counter body and humidity. In high humid conditions, the hardness of counter body plays a dominant role in formation of mechanically mixed layer (MML). The formation and stability of MML was known to reduce wear of tribosystem as a layer of different composition separates the interacting surfaces. However, if MML is not stable and breaks up easily and abrasion action of wear particles results in a high wear rate and coefficient of friction (COF).

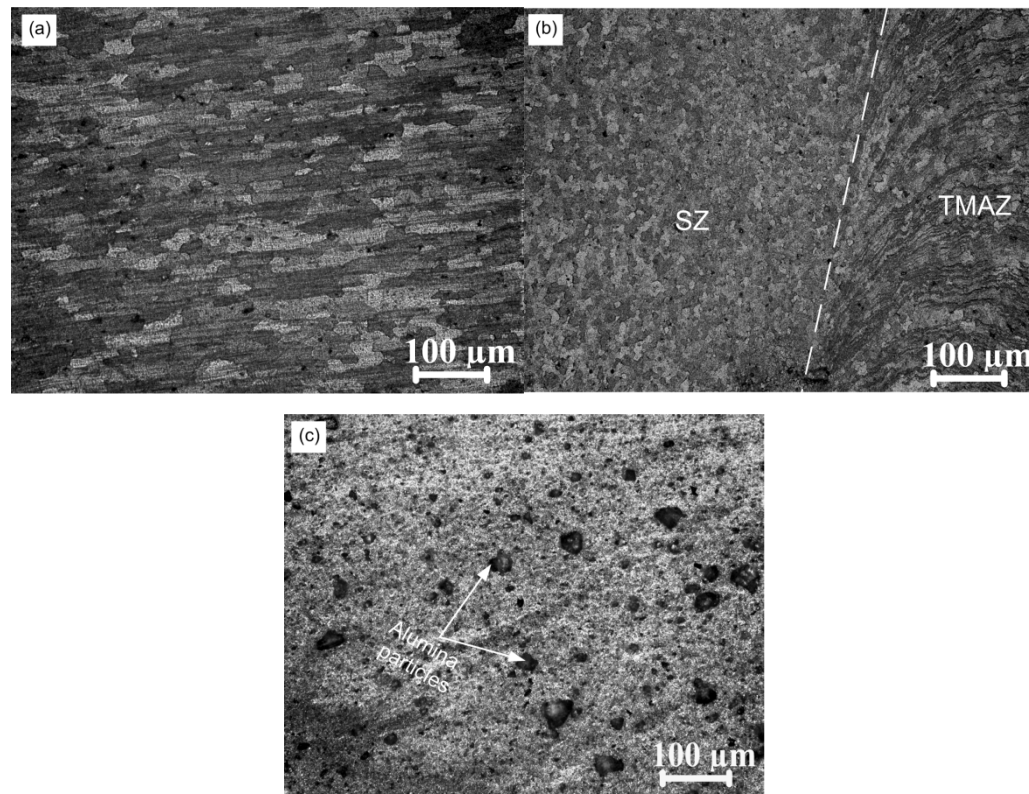
Ma et al. (2009) studied tribological characteristics of copper-graphite composite against different counterpart materials. They used aluminum alloy 2024, magnesium alloy AZ91D and titanium alloys Ti-6Al-4V as a counterpart material. It was found that tribological characteristics of copper-graphite composite strongly depended on its counterpart materials. Formation of transfer layer in composite with different counterpart materials influences the tribological characteristics. The friction and wear behavior of  $TiB_2$  and  $TiB_2-TiSi_2$  against two different counterpart materials: bearing grade steel and WC-Co ball was studied by Raju and Basu (2012). In fretting wear test, they found that steel ball was worn out whereas mild abrasion and tribo-oxidation was observed on WC-Co ball. The harder  $TiB_2$  abrades the steel counterbody and the transfer of tribolayer to the  $TiB_2$  surface contributes to negative wear of  $TiB_2$  ceramics. Tribochemical layer was observed in steel counterbody whereas no such layer was found in WC-Co counterbody. Haseeb et al. (2000) used two different counterpart materials of quenched-tempered iron and austempered ductile iron with same hardness level. The difference between the wear resistance of quenched-tempered and austempered ductile irons both having the same initial hardness was attributed to the difference in their microstructures. Soleymani et al. (2012) fabricated surface composites by reinforcing molybdenum disulphide ( $MoS_2$ ) and SiC particles in AA5083 alloy via FSP route. They observed that hybrid composites showed the highest wear resistance due to the formation of solid lubricating film. Behnagh et al. (2012) found that the coefficient of friction in FSPed AA5083 alloy was nearly half as compared to the base alloy due to increase in hardness after FSP. But tribological characteristics as function of counterbody characteristics were not reported.

While the effect of counterbody on wear behavior of conventionally prepared metal matrix or ceramic matrix composites is considerably reported, understanding on the effect of counterbody hardness on the friction and wear behavior of FSPed aluminum alloy surface composites is not available.

In the present work, FSPed  $\text{Al}_2\text{O}_3/\text{AA5083}$  surface composites are subjected to unlubricated sliding wear at 5 or 20 N load against steel balls of different hardness. The as-received AISI 52100 bearing grade steel ball of 800 HV is subjected to heat treatment at 650 and 480 °C so as to obtain hardness of 300 HV and 450 HV, respectively. The effect of hardness of steel ball on friction and wear of FSPed  $\text{Al}_2\text{O}_3/\text{AA5083}$  surface composites is discussed. The dominant mechanisms of material removal are elucidated as function of hardness of counterbody and applied sliding load.

## 7.2 Microstructure

Typical optical microstructures of base alloy AA5083, FSPed alloy and  $\text{Al}_2\text{O}_3$  reinforced surface composite are shown in Figs. 7.1 (a-c). The base alloy shows elongated grains with average grain size of 80  $\mu\text{m}$  (Fig. 7.1a). The SZ-TMAZ interface of FSPed base alloy exhibits microstructural refinement in SZ (Fig. 7.1b). The micrograph of surface composite shows uniform distribution of reinforcement particles in the matrix (Fig. 7.1c).

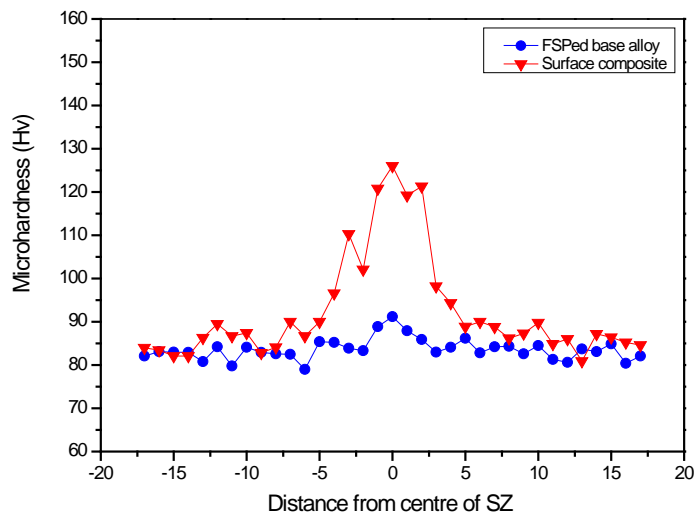


**Fig.7.1:** Optical micrographs (a) base alloy (b) FSPed alloy at SZ-TMAZ interface (c)  $\text{Al}_2\text{O}_3/\text{AA5083}$  surface composite



### 7.3 Hardness

The microhardness across the transverse sections of FSPed alloy and Al<sub>2</sub>O<sub>3</sub>/AA5083 surface composite are presented in Fig. 7.2. After FSP, the hardness of AA5083 increases to ~91 Hv in the SZ as compared to average hardness of base alloy (~82 Hv). The increase in hardness is attributed to the microstructural refinement after FSP. The Al<sub>2</sub>O<sub>3</sub>/AA5083 surface composite exhibits maximum hardness of 126 Hv in the SZ. The high hardness of surface composite is due to addition of Al<sub>2</sub>O<sub>3</sub> particles and grain refinement.

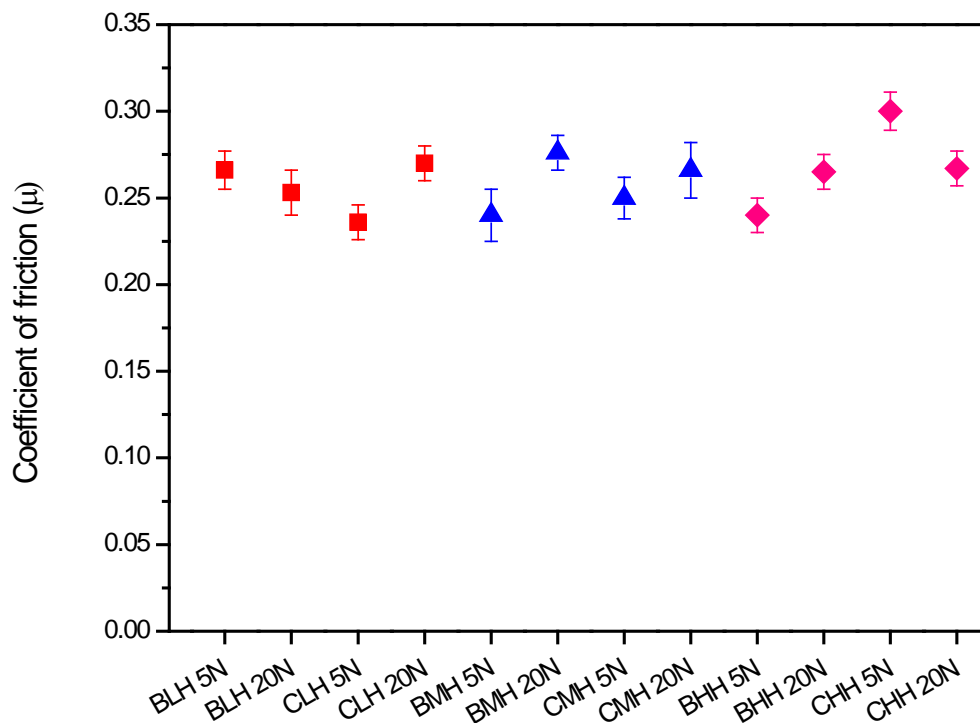


**Fig.7.2:** Microhardness across the transverse sections of FSPed base alloy and surface composite

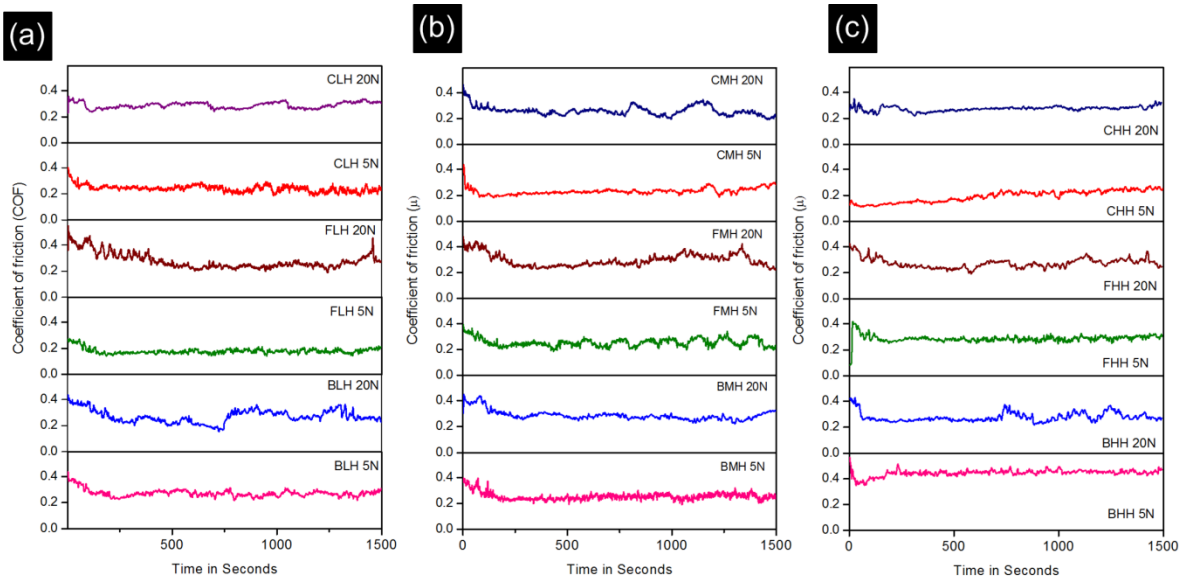
### 7.4 Friction characteristics

The coefficient of friction (COF) of different tribo-pairs is presented in Fig. 7.3. The average COF varied between 0.23 and 0.3 for surface composite and base alloy when against different hardness of counterbodies. In all the tribopairs, the surface composite slid against low hardness counterbody (CLH) at 5N load exhibits low COF of 0.23, whereas a relatively higher COF of 0.3 was noticed for tribopair of high hardness counterbody (CHH) and surface composite at 5N load. It is interesting to note that COF of surface composite slid against CHH at 20N load was 0.26. This discrepancy in COF can be attributed mainly to the adherence of material on the counterbody, protruding reinforcement particles, abrading action of the wear debris and stability of the tribolayer. The reduction in COF at higher loads may be due to the sliding between tribochemical layers, instead of the virgin surfaces of the tribopair. The representative COF curves for base alloy

and surface composites slid against different counterbodies is shown in Figs. 7.4 (a-c). COF attained steady state after ~100 seconds in all counterbody hardness conditions. Fluctuations in COF curves are more pronounced at higher loads of 20N irrespective of the counter body hardness.



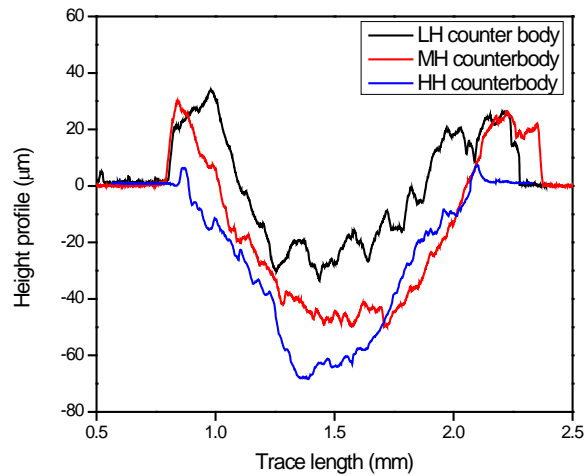
**Fig.7.3:** Coefficient of friction for the investigated surface composites of alumina/AA5083 surface composites. BLH: base alloy against low hardness ball; CLH: surface composite against low hardness ball; BMH: base alloy against medium hardness ball; CMH: surface composite against medium hardness ball; BHH: base alloy against high hardness ball; CLH: surface composite against high hardness ball



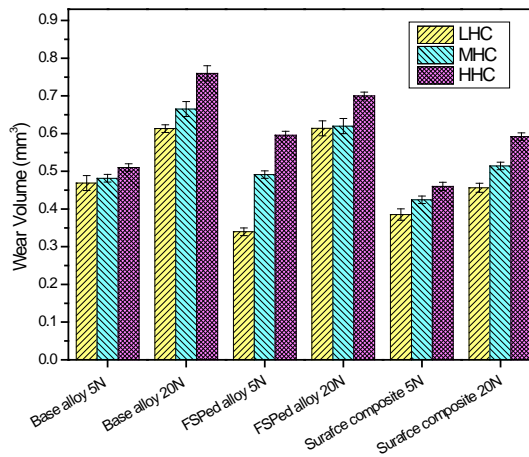
**Fig. 7.4:** Representative COF curves for base alloy and surface composites slid against (a) low hardness steel ball (b) medium hardness steel ball and (c) high hardness steel ball. BLH: base alloy against low hardness ball; CLH: surface composite against low hardness ball; BMH: base alloy against medium hardness ball; CMH: surface composite against medium hardness ball; BHH: base alloy against high hardness ball; CLH: surface composite against high hardness ball

### 7.5 Wear results

Typical worn surface profiles of  $Al_2O_3/AA5083$  surface composite slid against different hardness steel ball at 20 N load are shown in Fig. 7.5. The surface profile obtained after sliding against low hardness steel ball shows less material removal as compared to that against medium or high hardness steel ball.



**Fig. 7.5:** Typical worn surface profiles of surface composites slid against counterbody steel balls with difference in hardness. LH: low hardness; MH: medium hardness; HH: high hardness



**Fig. 7.6:** Wear volume of surface composites at 5 N and 20 N loads as function of hardness of counterbody steel ball. LHC: low hardness counterbody; MHC: medium hardness counterbody; HHC: high hardness counterbody

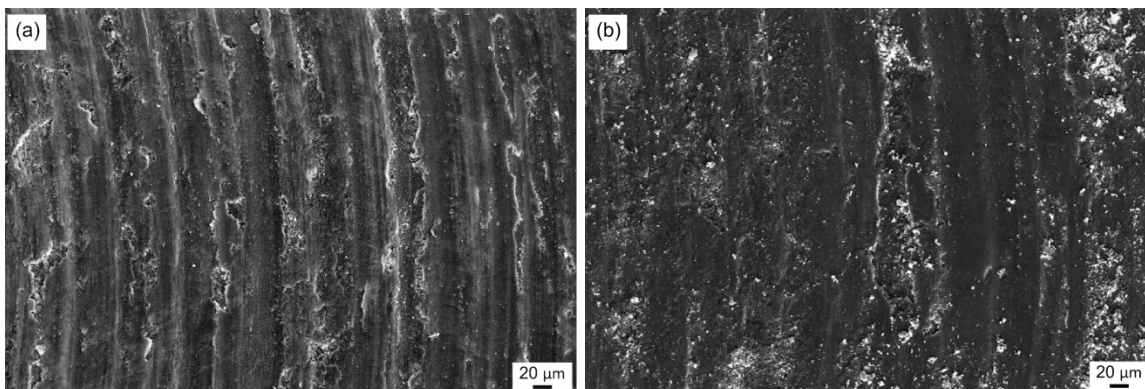
The wear volume of base alloy AA5083, FSPed base alloy and  $\text{Al}_2\text{O}_3/\text{AA5083}$  surface composite at 5 N and 20 N loads are shown as function of hardness of counterbody steel ball in Fig. 7.6. Wear volume of investigated materials ranged from 0.35 to 0.75  $\text{mm}^3$  with changes in load or hardness of counterbody. Wear volume of base alloy, FSPed alloy or surface composite increased with increase in load when slid against steel ball of any hardness. In general, the surface composite

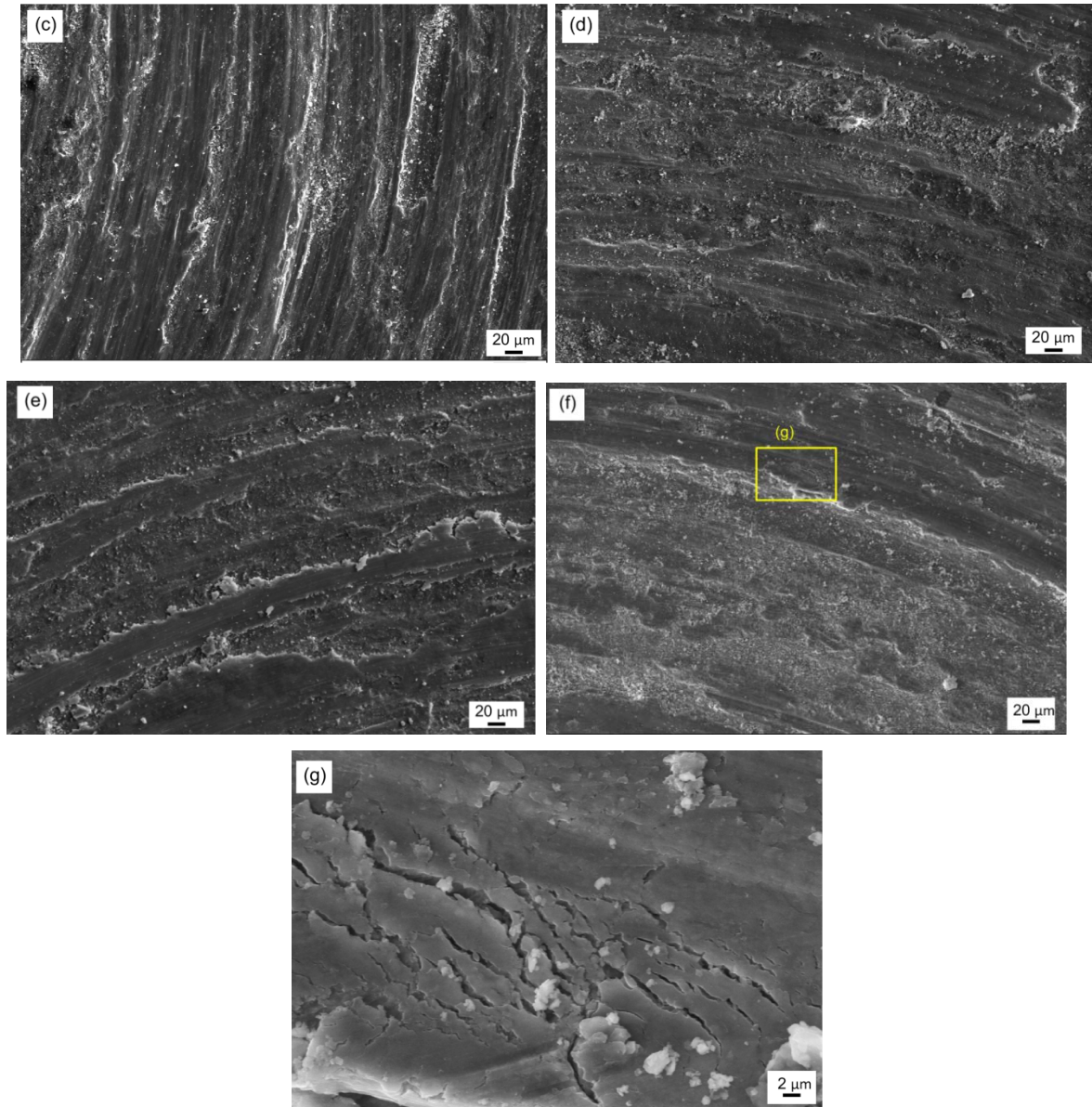
exhibits less wear (except for FSPed alloy at 5 N). Wear volume of any material increases with the hardness of counterbody steel ball.

## 7.6 Worn surface analysis

### 7.6.1 Surface analysis of materials worn against low hardness counter body

The worn surfaces of base alloy and surface composite after sliding against low hardness counterbody at 5 N and 20 N loads are shown in Figs. 7.7 (a-g). The worn surface of base alloy at 5 N load exhibits flow wear like characteristics with plowing marks (Fig. 7.7a). The material deformed in layers due to plowing action of hard asperities. FSPed alloy worn surface at 5 N load shows plowing marks with microcracks and wear particles (Fig. 7.7b). The worn surface of surface composite (Fig. 7.7c) shows plowing marks with craters suggesting material removal by abrasive and adhesive wear mechanisms. The worn surface of base alloy at 20 N load indicates material removal from upper layer by delamination, as shown in Fig. 7.7 (d). The wear particles on the surface are also observed suggesting crushing of trapped wear particles. The trapped wear particles provide an abrading action by acting as a third body, which increase the wear rate. A stable tribolayer can have a beneficial effect by forming a protective layer that separates the surfaces of tribopair and reduces friction and wear (Cherif 1997). The worn surface of FSPed base alloy at 20 N exhibits layers with microcracks (Fig. 7.8e). It can be noted that repeated deformation generates microcracks in the layers and these microcracks interlink to generate wear particles. The worn surface of surface composite after sliding at 20 N load (Fig. 7.8f) reveals the presence of intact layer as well as rough surface after layer removal. A higher magnification micrograph of selected region in Fig. 7.8 (f) is shown in Fig. 7.8 (g). It can be observed that random cracks are generated in the layer which eventually generated wear particles on further deformation.



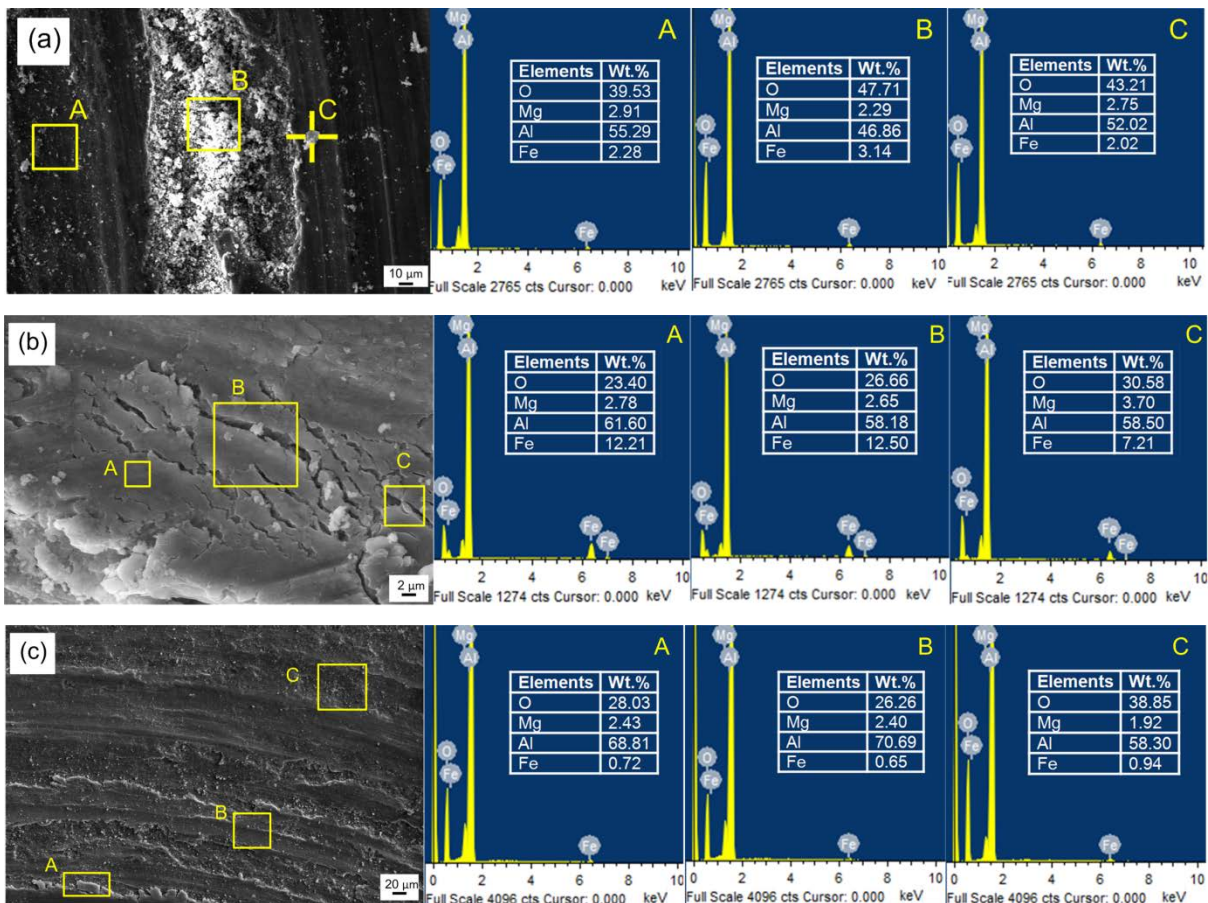


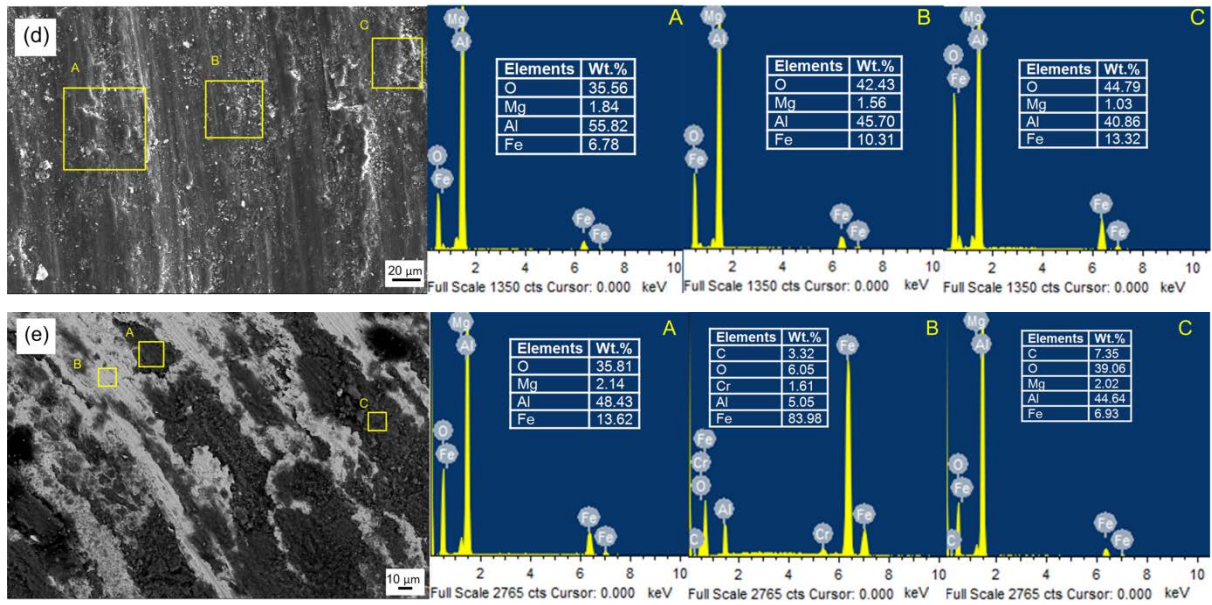
**Fig. 7.7:** SEM images of worn surfaces after sliding against low hardness steel ball: (a) base alloy at 5 N load (b) FSPed alloy at 5 N (c) surface composite at 5 N load (d) base alloy at 20 N load (e) FSPed alloy at 20 N load (f) surface composite at 20 N load (g) higher magnification view of Fig. (f)

Typical EDS analysis of worn surface of surface composite, FSPed alloy and steel counterbody is shown in **Figs. 7.8 (a-e)**. The EDS analysis of worn surface of surface composite indicates the presence of iron and oxygen content. The iron content is derived from the counterbody, while oxygen is picked up from the environment in the tribocontact. The presence of counterbody material on worn surface suggests two ways transfer of material in the tribosystem. It was reported

that abrasive action of the hard reinforcement particles picks the iron from counterbody and enhances the formation of tribolayer (Alpas and Zhang 1994). The high content of 7-12 percent of iron in EDS analysis suggests that a mechanical mixing occurs during sliding between the material derived from the surface of composite, surface of counterbody and environment. This mechanically mixed material is consolidated to form a layer or ejected from the tribosystem.

The worn surface and EDS analysis of FSPed alloy at 20 N load, as shown in **Fig. 7.8 (c)** clearly reveal the role of hard reinforcement particles in the formation of MML. The iron content is less than 1 percent suggesting less transfer of material from the counterbody. The role of reinforcement particles is more clear from the EDS analysis of worn surface of surface composite at 5 N load (Fig. 7.8d). At lower load, the iron content is found be in the range of ~ 6-13 percent suggesting that Al<sub>2</sub>O<sub>3</sub> particles effectively picks iron from the counter body even and favors the formation of tribolayer. The EDS analysis of worn surface of counterbody slid against surface composite at 20 N load along with back scattered SEM image is given in Fig. 7.8(e). The adhered mechanically mixed material containing oxidized iron and aluminum is observed.





**Fig. 7.8:** EDS analysis of worn surfaces after sliding against low hardness steel ball: (a) surface composite at 20 N load (b) layer formed on surface composite at 20 N load (c) FSPed alloy at 20 N load (d) surface composite at 5 N load (e) ball surface slid against surface composite at 20 N load.

The 3-D optical profilometer images of worn surface of low hardness steel balls slid against surface composite at 5 N and 20 N load are shown in Figs. 7.9 (a-b). The top and side views of worn surface at 5 N load exhibit transferred material and plowing marks (Fig. 7.9a). At 20 N load, less material is adhered to the counterbody as material transfers to a large extent at higher load (Fig. 7.9b)



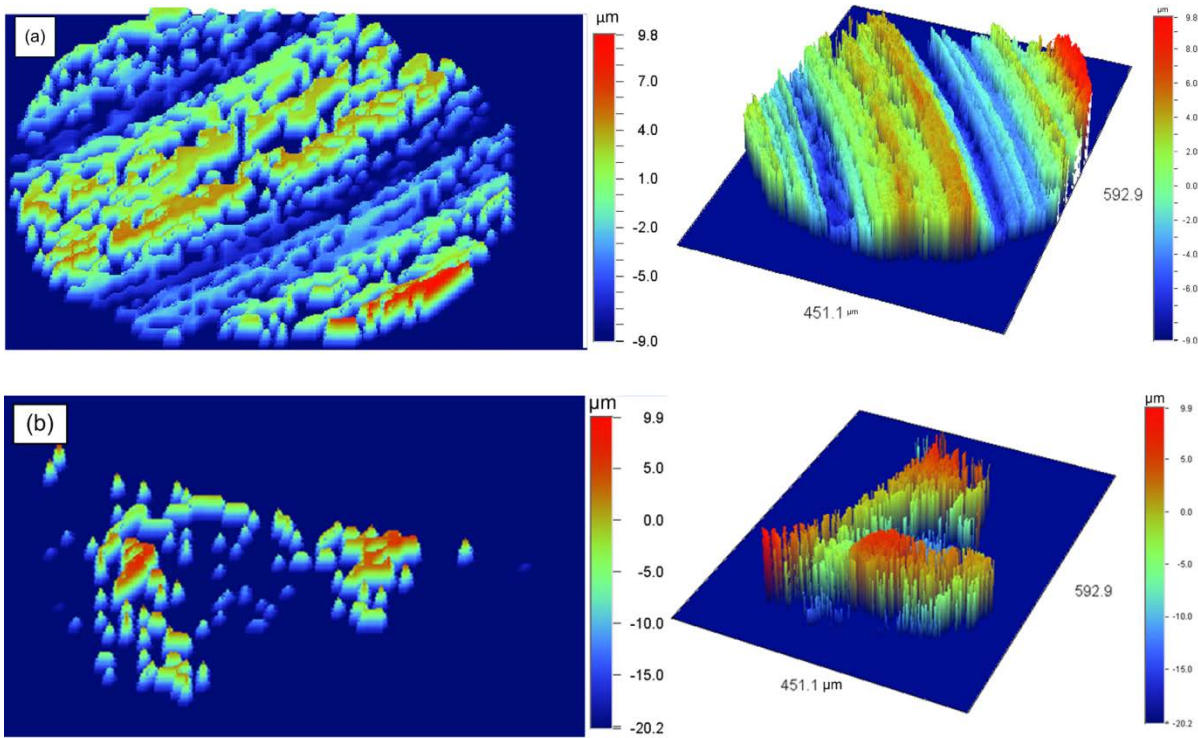
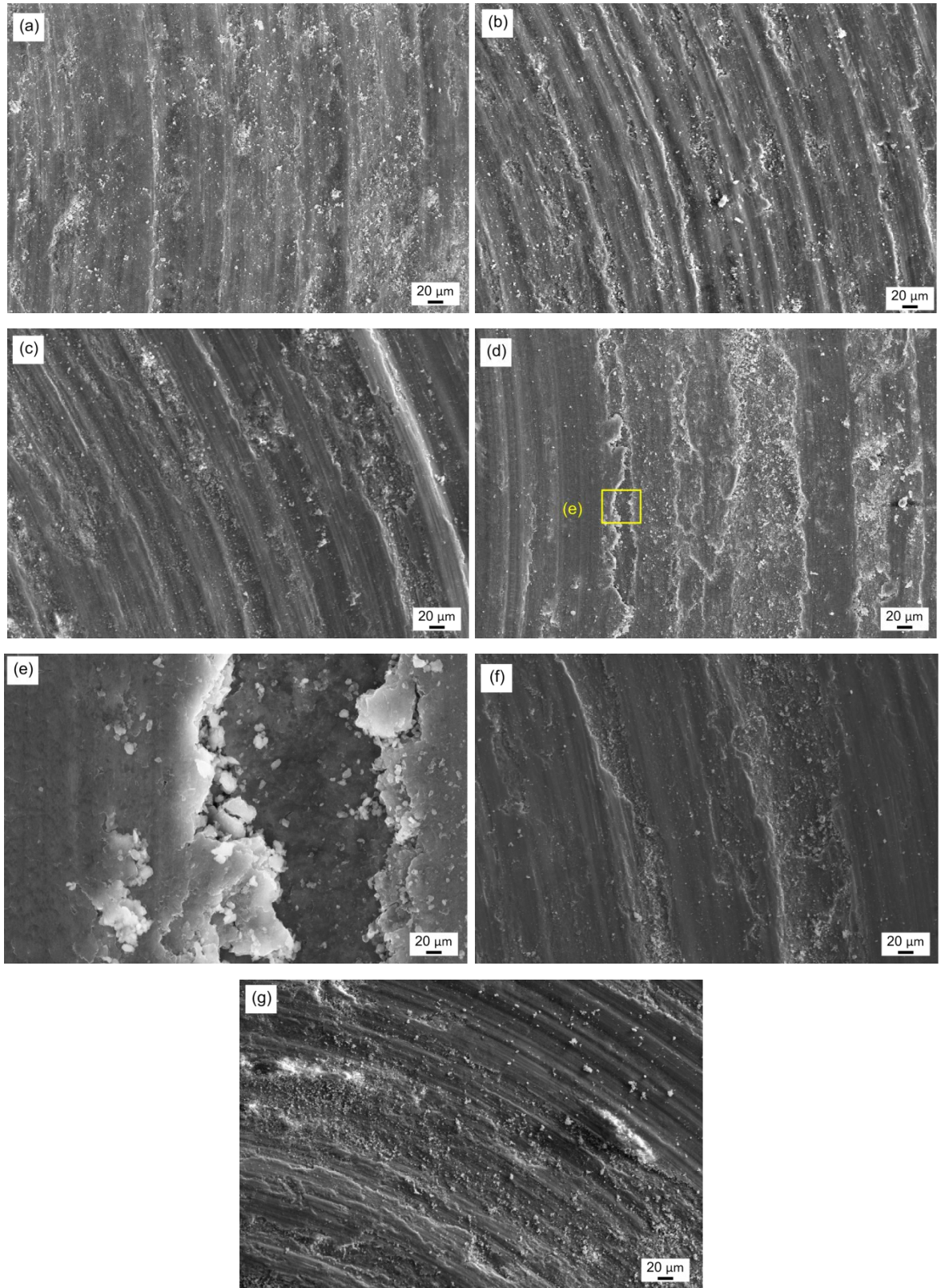


Fig.7.9: 3-D optical profilometer images of low hardness steel ball after sliding against surface composites at (a) 5 N load (b) 20 N load

### 7.6.2 Surface analysis of materials worn against medium hardness counter body

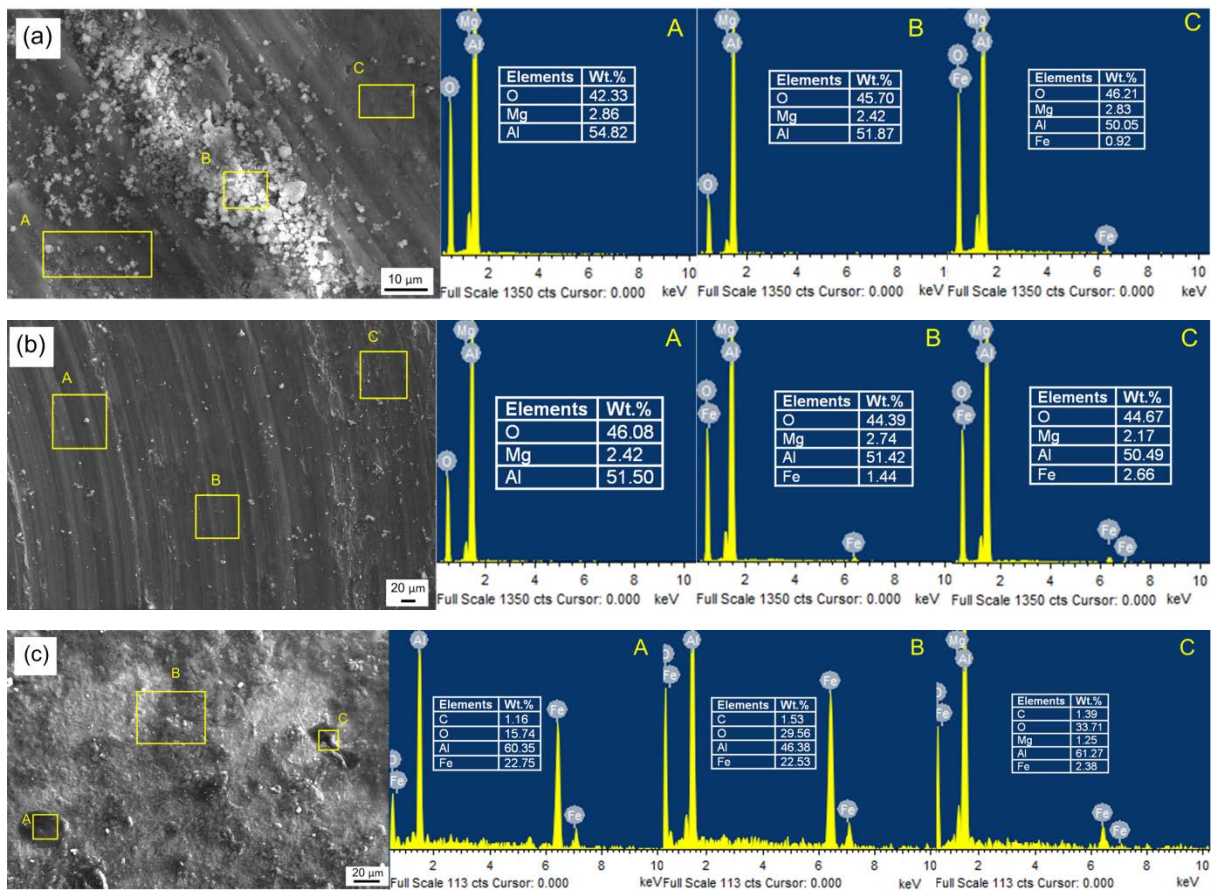
The worn surfaces of base alloy and surface composite slid against medium hardness steel ball at 5 N and 20 N loads are shown in Figs. 7.10 (a-g). The base alloy worn surface at 5 N load exhibits shallow plowing marks with fine wear particles (Fig. 7.10a). The worn surface of FSPed base alloy slid at 5 N load exhibits plowing marks (Figs. 7.10b). The material removal from layers and the presence of wear particles are also observed. The fine wear particles are formed due to crushing of trapped wear particles during sliding. The worn surface of surface composite at 5 N load exhibits plowing marks, as shown in Fig. 7.10 (c). Fig. 7.10 (d) shows the worn surface of base alloy at 20 N load. The material deforms in the layers and cracks are generated on further deformation during sliding. A magnified image of selected region in Fig.7.10 (d) (showed in Fig. 7.10e) exhibits microcracks at edges of layer. This suggests delamination wear at a load of 20 N in the base alloy. The FSPed alloy also exhibits flow like characteristics, as shown in Fig. 7.10 (f). The worn surface of surface composite after sliding at 20 N load exhibits smooth region with plowing marks and rough surface suggesting material removal by adhesion and delamination (Fig. 7.10g).



**Fig.7.10:** SEM images of worn surfaces after sliding against medium hardness steel ball (a) base alloy at 5 N load (b) FSPed alloy at 5 N (c) surface composite at 5 N load (d) base alloy at 20 N

load (e) higher magnification view of Fig. (d) (f) FSPed alloy at 20 N load (g) surface composite at 20 N load

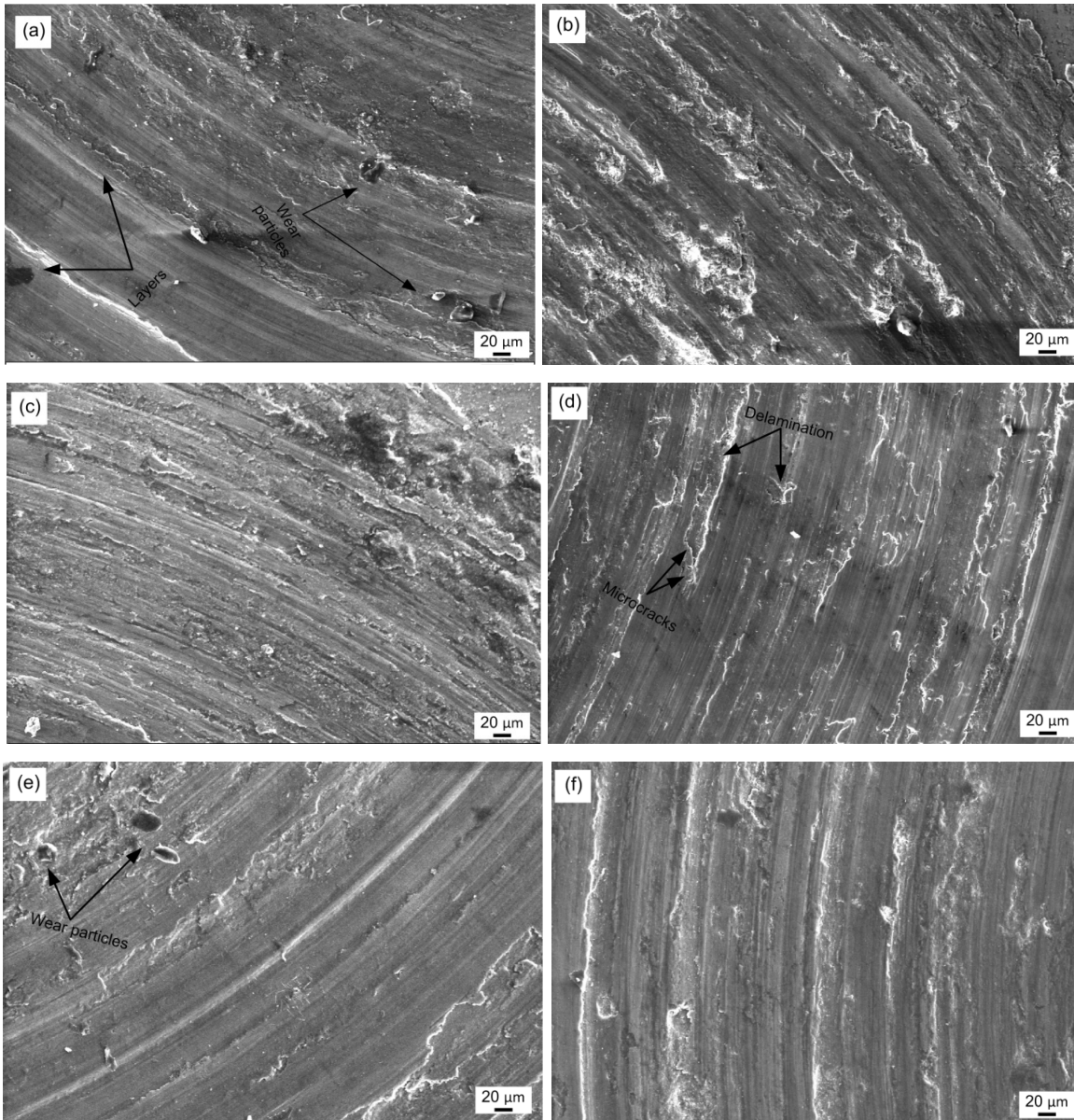
The EDS analysis of worn surface of surface composite and counterbody slid against medium hardness counterbody at 5 N and 20 N loads is shown in Figs.7.11 (a-c). The worn surface of surface composite at 5 N load shows less content of iron suggesting absence of stable MML formation (Fig. 7.11a). Fig. 7.11 (b) shows EDS analysis of worn surface composite after sliding at 20 N load. The iron content on worn surface is increased at 20 N load as compared to 5 N load. However, the increase in iron content is limited to less than 3 percent. The EDS analysis of worn surface of counterbody shows transferred aluminum from the matrix of composite (Fig. 7.11c).



**Fig.7.11:** EDS analysis of worn surfaces after sliding against medium hardness steel ball (a) surface composite at 5 N load (b) surface composite at 20 N load (c) ball surface slid against surface composite at 20 N load

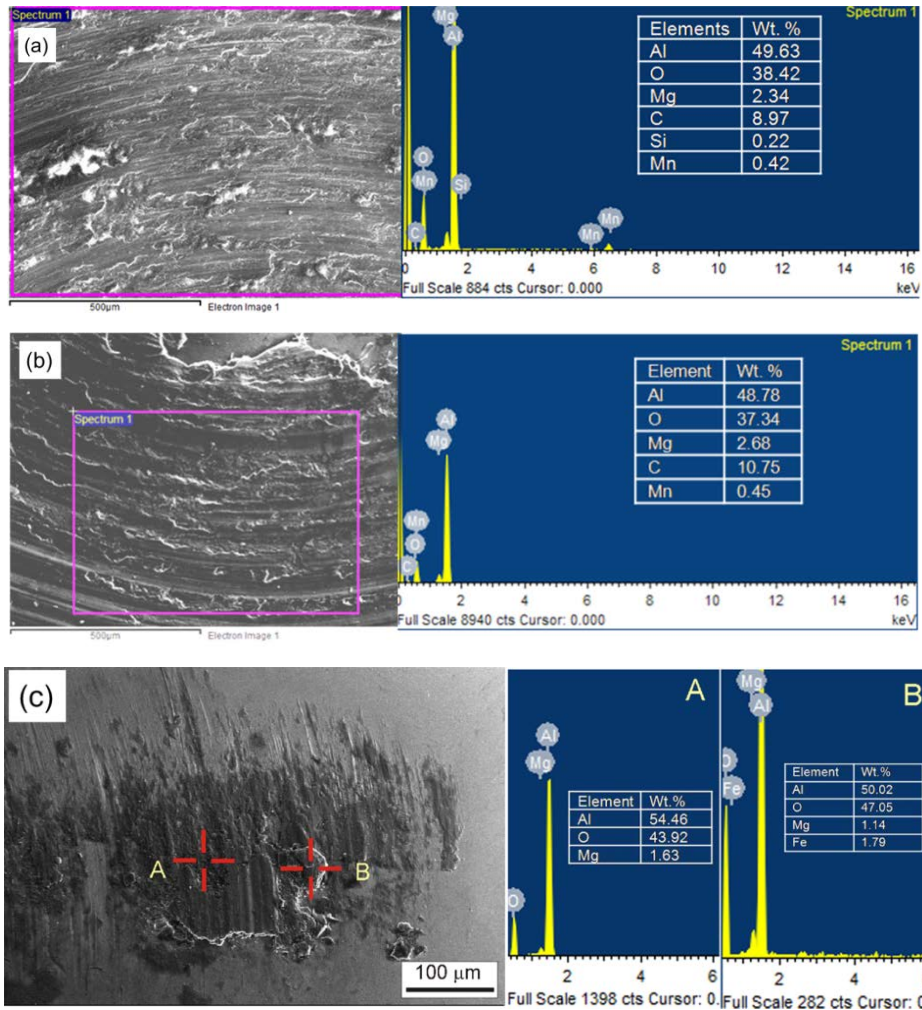
### **7.6.3 Surface analysis of materials worn against high hardness counter body**

The worn surface SEM images of base alloy and surface composite slid against high hardness counterbody at 5 N and 20 N load are presented in Fig. 7.12 (a-f). The worn surface of the base alloy when slid at 5N load exhibits flow of material in the direction of sliding (Fig.7.12a). A step in layered features is observed due to removal of adjacent material layers is attributed to delamination wear mechanism. The presence of plowing marks along with craters can be observed on the worn surface of FSPed alloy after sliding at 5 N load (Fig.7.12b). The craters are formed due to material removal by adhesive wear mechanism. The softer material from the matrix is transferred to harder counterbody. Fig.7.12 (c) reveals material removal by delamination wear on the worn surface of surface composite. The worn surface of base alloy at 20 N load shows the microcrack generation and material removal by interlinking of these cracks (Fig. 7.12d). Also, the worn surface of FSPed alloy exhibits material flow in layers and generates microcracks at edges of layers. The worn surface of surface composite when slid at 20 N load shows deeper plowing marks with craters (Fig.7.12e). The craters are formed due to delamination and adhesive mechanisms.



**Fig.7.12:** SEM images of worn surfaces after sliding against high hardness steel ball (a) base alloy at 5 N load (b) FSPed alloy at 5 N (c) surface composite at 5 N load (d) base alloy at 20 N load (e) FSPed alloy at 20 N (f) surface composite at 20 N load

Typical EDS analysis of worn surface of surface composite and counterbody steel ball is shown in Fig. 7.13 (a-c). Fig.7.13 (a) shows worn surface of surface composite when slid at 5 N load. EDS analysis indicates the absence of iron on the worn surface at 5 N load. Similarly at 20 N load, the presence of iron is not detected, as shown in Fig. 7.13 (b). However, a small amount (<2%) of iron is detected on the transferred material on the counterbody as shown in Fig. 7.13 (c).

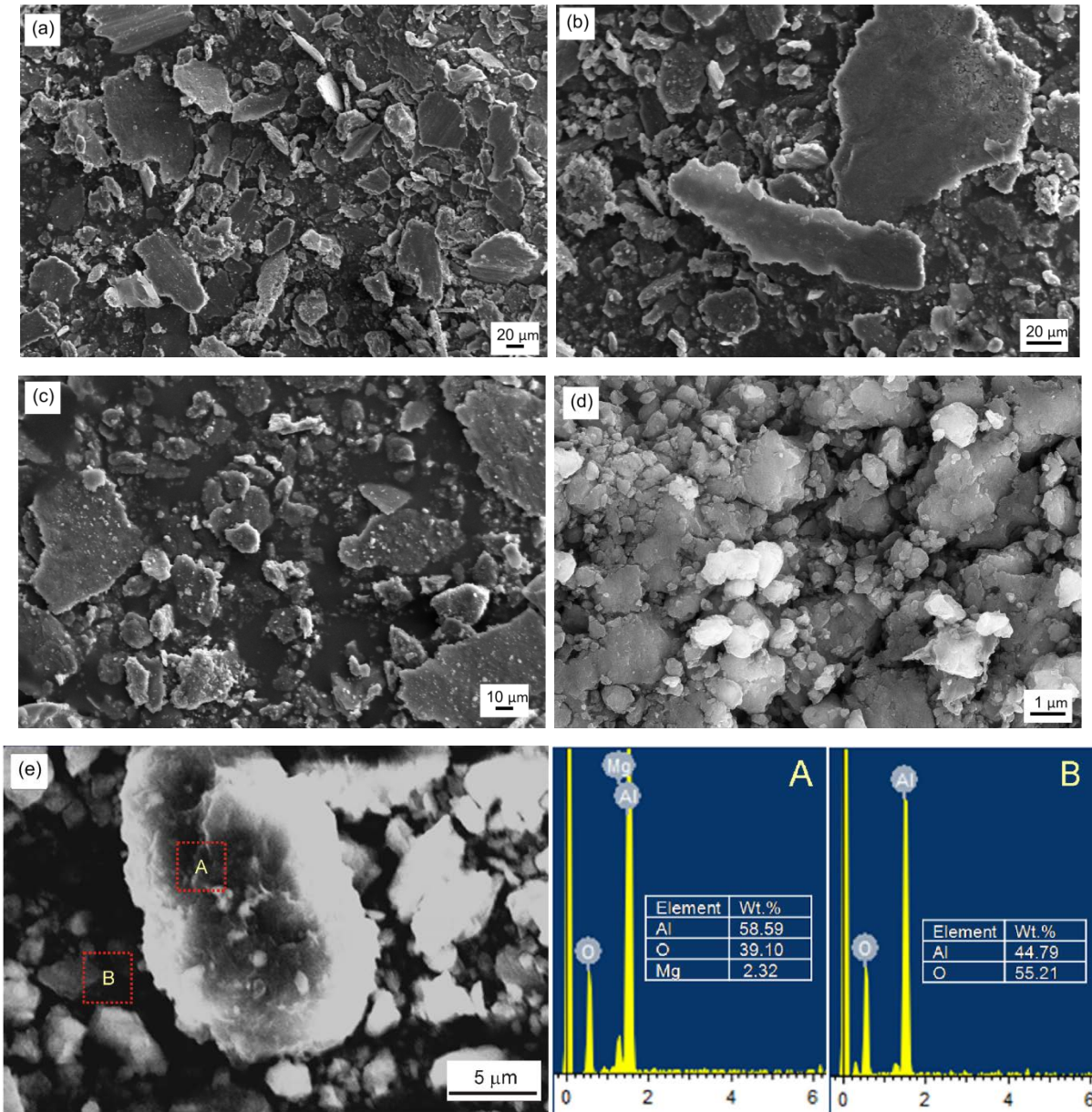


**Fig.7.13:** EDS analysis of worn surfaces after sliding against high hardness steel ball:(a) surface composite at 5 N load (b) surface composite at 20 N load (c) counterbody at 20 N load

### 7.7 Wear debris analysis

SEM-EDS analysis of wear debris collected during sliding against high hardness steel ball is shown in Figs. 7.14 (a-e). Fig. 7.15 (a) shows wear debris particles obtained when base alloy slid at 20 N load. The debris particles are mostly flaky shaped, while few are crushed to small size suggesting domination of delamination wear. The wear debris particles of FSPed alloy are also flaky type (Fig. 7.14b). Crushed debris agglomerates are also observed. On the other hand, ultrafine wear debris particles are also formed along with flaky debris when surface composite worn at 5 N load (Fig. 7.14c). The wear debris particles of surface composite worn at higher load of 5 N are mostly ultrafine in size, while flaky debris particles are not found (Fig.7.14d). At higher

load, wear debris particles are trapped and crushed to a finer size due to repeated sliding. EDS analysis of wear debris at 20 N load shows high oxygen content and absence of iron (Fig. 7.14e).



**Fig.7.14:** Wear debris of worn surfaces after sliding against high hardness steel ball:(a) base alloy at 20 N load (b) FSPed alloy at 20 N load (c) surface composite at 5 N load (d) surface composite at 20 N load (e) EDS analysis of wear debris generated at 20 N load

## 7.8 Summary

Surface composites of alumina/AA5083 were prepared using multi-pass FSP and subjected to sliding wear at 5 or 20 N load in unlubricated sliding conditions against steel balls with variation in hardness. The dominant wear mechanisms were elucidated as function of hardness of steel ball and sliding load. Summary of major results is provided here.

- a) Sliding at low load of 5 N also results in lower wear when compared against wear at 20 N.
- b) Material transfer, abrasion, flow wear and delamination are dominated in base alloy while abrasion and material transfer are observed in surface composites.
- c) Results showed that wear of surface composites against low hardness counter body enhances the formation of mechanical mixed stable layer at the contact and improves wear resistance as compared to that against high hardness counter body.
- d) Low hardness counter body enhances the formation of mechanical mixed stable layer as compared to high hardness counter body.





**8.1. Conclusions**

The major aim of the present investigation is to understand the influence of friction stir process parameters on microstructure, mechanical or wear behavior of aluminium alloy surface composites. Three alloys of aluminium AA2014, LM24 and AA5083 were selected as matrices, while ceramics particles SiC, TiC, Al<sub>2</sub>O<sub>3</sub>, graphite or metallic particles Sn were used as reinforcements. The tribological performance of the FSPed surface composites against steel ball was studied using a ball-on-disc tribometer in unlubricated sliding conditions. The total research can be divided into four major parts.

In the first part, the effect of multi-pass and SiC or TiC particle reinforcement on microstructure and mechanical characteristics of AA2014 surface composites was studied. The microstructure and mechanical characterization of AA2014 surface composites is provided in **Chapter 4**. Results demonstrated that multi-pass FSP provides increased refinement of grains than one pass FSP in base AA2014-T651 alloy. However, extensive overaging of precipitates in FSP causes softening and reduces the strength and hardness of the FSPed alloy. After FSP, the average grain size of the surface composite SiC/AA2014 is found to be 8 μm, whereas the average grain size in TiC/AA2014 surface composite is found to be 6 μm. The restricted grain growth TiC/AA2014 surface composite as compared to SiC/AA2014 is due pinning effect of finer TiC particles.

In the second part, suitability of FSP strategies to achieve uniform distribution of SiC particles in AA5083 alloy was discussed. Strategies including variation in rotational speed, dual tool processing and tool offset over-lapping were studied. The major findings are provided in **Chapter 5**. Results from this part of the research demonstrated that bands of reinforcement particles are formed at the lower rotational speed of 1000 or 1400 rpm, while no such bands are observed at higher rotational speed of 2000 rpm. A microstructure with uniformly distributed SiC particles completely extending to the area influenced by the shoulder is obtained in surface composites FSPed at a higher rotational speed of 2000 rpm. The tool offset method provided bands, whereas the post processing by a bigger diameter tool produced notable defects and inhomogeneous distribution of particles. It is concluded that FSP using high rotational speeds is an effective strategy to improve the distribution of particles.

Keeping view of the importance of lubricious effect of graphite and anti-seizure effect of tin in tribological contacts, the synergetic effect of rotational speed (1000 or 1400 rpm) in graphite or graphite and tin (in equal wt. % proportion) reinforcement in LM24 alloy on microstructural characteristics, mechanical properties and tribological behavior were studied in the subsequent part of the thesis, and results are provided in **Chapter 6**. It is found that the higher rotational speed provides more shattering effect and high input in the SZ leading to enhanced material flow. Wear reduced in surface composites fabricated using a rotational speed of 1400 rpm. Only graphite addition provides less friction and wear for the composites fabricated at a rotational speed of 1400 rpm. The worn surface analysis indicated that material transfer, abrasion, flow wear and delamination wear are dominant in base alloy, while abrasion and material transfer are observed in surface composites.

In the last part of the thesis, the effect of counterbody hardness on tribological behavior of alumina reinforced AA5083 surface composites in sliding conditions. To study the effect of counterbody hardness, the ASI52100 steel balls were heated at different temperatures to obtain different hardness. Results are given in **Chapter 7**. The wear of surface composites against less harder (300 Hv) steel ball enhances the formation of mechanical mixed stable layer at the contact and improves wear resistance as compared to that against harder (800Hv) steel ball. Sliding at low load results in less wear.

Results obtained from the series of experiments in the present research truly illustrate the significant role of friction stir processing parameters, reinforcement and sliding conditions on the tribological performance of aluminium alloy surface composites. A change in process parameters or type of reinforcement leads to considerable difference in microstructural features, particularly the particle distribution and mechanical properties of aluminium alloy surface composites. With respect to tribological behavior, sliding test conditions like load or counterbody hardness additionally influence friction and wear characteristics of aluminium alloy surface composites by changing the wear mechanisms. Therefore, it can be concluded that friction stir processing of aluminium alloy surface composites should be done using suitable process parameters and reinforcement for given tribological application as the mechanisms of wear are highly sensitive to microstructure and contact interactions at the sliding interface.

In the backdrop of the present experimental research, it can be concluded that high rotational speeds are recommended for fabricating SiC/AA5083 surface composites with highly uniform distribution of reinforcement. The addition of tin in graphite/LM24 surface composite is not suggested for use in sliding wear contacts against steel. On the other hand, alumina/AA5083 surface composites are recommended for use against less harder (300 Hv) steel balls in sliding conditions.

## 8.2. Scope for future work

- In the present work, the distribution of reinforcement particle in aluminium surface composites is studied qualitatively, whereas quantitative analysis of particle distribution is recommended in identifying suitable combination of friction stir process parameters. Work in this direction is suggested.
- The external cooling of is likely to modify microstructure of the FSPed surface. Thus, it would be interesting to study the effect of controlled external cooling on the microstructure, mechanical or wear behavior of aluminium alloy surface composites.
- Friction stir processing of aluminium alloy surface composites reinforced with micron sized particles is studied in the present work. The influence of reinforcement of nano size particles on the microstructure and tribological performance is recommended for future work.
- The reinforcement of graphite and tin in LM24 alloy is shown to be ineffective than reinforcement of only graphite in LM24 alloy in reducing friction and wear. A study on microalloying with other low melting point materials like lead can be carried on the tribological behaviour of graphite/LM24 surface composites.
- In order to explore full potential of FSP as a technique in fabricating surface composite, modeling studies on the wear performance as function of FSP parameters are recommended.
- As general remarks, FSP can also be studied in developing defect free polymer surface composites. It can be developed as an alternative to thermal spray coating. As tool wear is an important issue, efforts should also be put on developing durable and cost effective tools.

## References

---

- 1) Abd El-Salam F., Abd El-Khalek A.M., Nada R.H., Wahab L.A., Zahran H.Y., 2010. Effect of Sn content on the structural and mechanical properties of Al-Si alloy. *Materials Science and Engineering: A* 527, 1223-1229.
- 2) Akagaki, T., Kato, K., 1991. Effects of additives on wear mode and morphology of wear debris generated in the lubricated sliding of steel. *Wear* 143, 119-135.
- 3) Akramifard H.R., Shamanian M., Sabbaghian M., Esmailzadeh M., 2014. Microstructure and mechanical properties of Cu/SiC metal matrix composite fabricated via friction stir processing. *Material and Design* 54, 838-844.
- 4) Alidokht S.A., Abdollah-zadeh A., Soleymani S., Assadi H., 2011. Microstructure and tribological performance of an aluminium alloy based hybrid composite produced by friction stir processing. *Material and Design* 32, 2727-2733.
- 5) Alpas A.T., Zhang J., 1994. Effect of microstructure (particulate size and volume fraction) and counterface material on the sliding wear resistance of particulate-reinforced aluminum matrix composites. *Metallurgical and Materials Transactions A* 25, 969-983.
- 6) Anvari S.R., Karimzadeh F., Enayati M.H., 2013. Wear characteristics of Al-Cr-O surface nano-composite layer fabricated on Al6061 plate by friction stir processing. *Wear* 304, 144-151.
- 7) Arbegast W.J., 2008. A flow-partitioned deformation zone model for defect formation during friction stir welding. *Scripta Materialia* 58, 372-376.
- 8) Arbegast W.J., and Hartley P.J., 1998. Friction stir weld technology development at Lockheed martin michoud space system- an overview., In: Vitek, J.M., Johnson, J.A. (Ed.), In: *Proceedings of the Fifth International Conference on Trends in Welding Research*, Pine Mountain, GA, USA. pp. 541-546.
- 9) Argade G.R., Kandasamy K., Panigrahi S.K., Mishra R.S., 2012. Corrosion behavior of a friction stir processed rare-earth added magnesium alloy. *Corrosion Science* 58, 321-326.
- 10) Arora H.S., Singh H., Dhindaw B.K., 2011. Composite fabrication using friction stir processing-A review. *The International Journal of Advanced Manufacturing Technology* 61, 1043-1055.
- 11) Arora H.S., Singh H., Dhindaw B.K., Grewal H.S., 2012. Some Investigations on Friction Stir Processed Zone of AZ91 Alloy. *Transactions of the Indian Institute of Metals* 65, 735-739.

- 12) Arora R., Kumar S., Singh G., Pandey O., 2014. Influence of particle size and temperature on the wear properties of rutile-reinforced aluminium metal matrix composite. *Journal of Composite Materials* 49, 843-852.
- 13) Arsenault R.J., and Shi N., 1986. Dislocation generation due to differences between the coefficients of thermal expansion. *Materials Science and Engineering* 81, 175-187.
- 14) Asadi P., Faraji G., Besharati, M.K. 2010. Producing of AZ91/SiC composite by friction stir processing (FSP). *The International Journal of Advanced Manufacturing Technology* 51, 247-260.
- 15) Asadi P., Givi M.K.B., Parvin N., Araei A., Taherishargh M., Tutunchilar S., 2012. On the role of cooling and tool rotational direction on microstructure and mechanical properties of friction stir processed AZ91. *The International Journal of Advanced Manufacturing Technology* 63, 987-997.
- 16) Asadi, P., Faraji, G., Masoumi, A., Besharati Givi, M.K., 2011. Experimental Investigation of Magnesium-Base Nanocomposite Produced by Friction Stir Processing: Effects of Particle Types and Number of Friction Stir Processing Passes. *Metallurgical and Materials Transactions A* 42, 2820-2832.
- 17) Avettand-Fènoël M.N., Simar A., Shabadi R., Taillard R., de Meester B., 2014. Characterization of oxide dispersion strengthened copper based materials developed by friction stir processing. *Material and Design* 60, 343-357.
- 18) Azizieh M., Kokabi A.H., Abachi P., 2011. Effect of rotational speed and probe profile on microstructure and hardness of AZ31/Al<sub>2</sub>O<sub>3</sub> nanocomposites fabricated by friction stir processing. *Material and Design* 32, 2034-2041.
- 19) Balasubramanian V., 2008. Relationship between base metal properties and friction stir welding process parameters. *Materials Science and Engineering: A* 480, 397-403.
- 20) Baradeswaran A., Perumal A.E., 2014. Wear and mechanical characteristics of Al 7075/graphite composites. *Composites Part B: Engineering* 56, 472-476.
- 21) Barmouz M., Givi M.K.B., 2011c. Fabrication of in situ Cu/SiC composites using multi-pass friction stir processing: Evaluation of microstructural, porosity, mechanical and electrical behavior. *Composites Part A: Applied Science and Manufacturing* 42, 1445-1453.
- 22) Barmouz M., Besharati Givi M.K., Seyfi J., 2011a. On the role of processing parameters in producing Cu/SiC metal matrix composites via friction stir processing: Investigating microstructure, microhardness, wear and tensile behavior. *Materials Characterization* 62, 108-117.

- 23) Barmouz M., Seyfi J., Kazem Besharati Givi M., Hejazi I., Davachi S.M., 2011b. A novel approach for producing polymer nanocomposites by in-situ dispersion of clay particles via friction stir processing. *Materials Science and Engineering: A* 528, 3003-3006.
- 24) Basavarajappa S., Chandramohan G., Mahadevan A., Thangavelu M., Subramanian R., Gopalakrishnan P., 2007. Influence of sliding speed on the dry sliding wear behaviour and the subsurface deformation on hybrid metal matrix composite. *Wear* 262, 1007-1012.
- 25) Batalha G.F., Farias A., Magnabosco R., Delijaicov S., Adamiak M., Dobrzański L.A., 2012. Evaluation of an AlCrN coated FSW tool. *Journal of Achievements in Materials and Manufacturing Engineering* 55, 607-615.
- 26) Bauri R., 2014. Optimization of process parameters for friction stir processing (FSP) of Al-TiC in situ composite. *Bulletin of Materials Science* 37, 571-578.
- 27) Bauri R., Yadav D., Suhas G., 2011. Effect of friction stir processing (FSP) on microstructure and properties of Al-TiC in situ composite. *Materials Science and Engineering: A* 528, 4732-4739.
- 28) Behnagh R.A., Besharati Givi M.K., Akbari M., 2012. Mechanical Properties, Corrosion Resistance, and Microstructural Changes during Friction Stir Processing of 5083 Aluminum Rolled Plates. *Materials and Manufacturing Processes* 27, 636-640.
- 29) Berbon P.B., Bingel W. H., Mishra R. S., Bampton C. C., and Mahoney M. W., 2001. Friction stir processing: A tool to homogenize nanocomposite aluminum alloys. *Scripta Materialia* 44, 61-66.
- 30) Bijwe J., 1997. Composites as friction materials: recent developments in non-asbestos fiber reinforced friction materials-A review. *Polymer Composites* 18, 378-396.
- 31) Borgonovo C., Apelian D., 2011. Manufacture of Aluminum Nanocomposites: A Critical Review. *Materials Science Forum* 678, 1-22.
- 32) Brahma Raju G., Basu B., 2010. Wear mechanisms of TiB<sub>2</sub> and TiB<sub>2</sub>-TiSi<sub>2</sub> at fretting contacts with steel and WC-6wt% Co. *International Journal of Applied Ceramic Technology* 7, 89-103.
- 33) Buffa G., Fratini L., Micari F., and Settineri L., 2012. On the choice of tool material in friction stir welding of titanium alloys, In:North American Manufacturing Research Conference. Society of Manufacturing Engineers, Notre Dame, Indiana, USA.
- 34) Chabok A., Dehghani K., 2012. Effect of Processing Parameters on the Mechanical Properties of Interstitial Free Steel Subjected to Friction Stir Processing. *Journal of Materials Engineering and Performance* 22, 1324-1330.



- 35) Chang C.I., Lee C.J., Huang J.C., 2004. Relationship between grain size and Zener-Holloman parameter during friction stir processing in AZ31 Mg alloys. *Scripta Materialia* 51, 509-514.
- 36) Chang C.I., Wang Y.N., Pei H.R., Lee C.J., Huang J.C., 2006. On the Hardening of Friction Stir Processed Mg-AZ31 Based Composites with 5–20% Nano-ZrO<sub>2</sub> and Nano-SiO<sub>2</sub> Particles. *Materials Transactions* 47, 2942-2949.
- 37) Chen C.F., Kao P.W., Chang L.W., Ho N.J., 2009. Effect of Processing Parameters on Microstructure and Mechanical Properties of an Al-Al<sub>11</sub>Ce<sub>3</sub>-Al<sub>2</sub>O<sub>3</sub> In-Situ Composite Produced by Friction Stir Processing. *Metallurgical and Materials Transactions A* 41, 513-522.
- 38) Chen C.M., Kovacevic R., 2003. Finite element modeling of friction stir welding-thermal and thermomechanical analysis. *International Journal of Machine Tools and Manufacture* 43, 1319-1326.
- 39) Cherif K., Gueroult B., Rigaud M., 1997. Al<sub>2</sub>O<sub>3</sub>-ZrO<sub>2</sub> debris life cycle during wear: effects of the third body on wear and friction. *Wear* 208, 161-168.
- 40) Choi D.-H., Kim Y.-H., Ahn B.-W., Kim Y.-I., Jung S.-B., 2013. Microstructure and mechanical property of A356 based composite by friction stir processing. *Transactions of Nonferrous Metals Society of China* 23, 335-340.
- 41) Cui G.R., Ma Z.Y., Li S.X., 2008. Periodical plastic flow pattern in friction stir processed Al-Mg alloy. *Scripta Materialia* 58, 1082-1085.
- 42) Devaraju A., Kumar A., Kotiveerachari B., 2013. Influence of rotational speed and reinforcements on wear and mechanical properties of aluminum hybrid composites via friction stir processing. *Material and Design* 45, 576-585.
- 43) Dilip J.J.S., Janaki Ram G.D., 2013. Microstructure evolution in aluminum alloy AA 2014 during multi-layer friction deposition. *Materials Characterization* 86, 146-151.
- 44) Dolatkah A., Golbabaie P., Besharati Givi M.K., Molaiekiya F., 2012. Investigating effects of process parameters on microstructural and mechanical properties of Al5052/SiC metal matrix composite fabricated via friction stir processing. *Material and Design* 37, 458-464.
- 45) Elangovan K., Balasubramanian V., 2008. Influences of tool pin profile and tool shoulder diameter on the formation of friction stir processing zone in AA6061 aluminium alloy. *Material and Design* 29, 362-373.

- 46) Elangovan K., Balasubramanian V., Valliappan M., 2007. Influences of tool pin profile and axial force on the formation of friction stir processing zone in AA6061 aluminium alloy. *The International Journal of Advanced Manufacturing Technology* 38, 285-295.
- 47) El-Rayes M.M., El-Danaf E.A., 2012. The influence of multi-pass friction stir processing on the microstructural and mechanical properties of Aluminum Alloy 6082. *Journal of Materials Processing Technology* 212, 1157-1168.
- 48) Erman A., Groza J., Li X., Choi H., Cao G., 2012. Nanoparticle effects in cast Mg-1wt% SiC nano-composites. *Materials Science and Engineering: A* 558, 39-43.
- 49) Faraji, G., Dastani, O., Mousavi, S.A.A.A., 2011. Effect of Process Parameters on Microstructure and Micro-hardness of AZ91/Al<sub>2</sub>O<sub>3</sub> Surface Composite Produced by FSP. *Journal of Materials Engineering and Performance* 20, 1583-1590.
- 50) Farias A., Batalha G.F., Prados E.F., Magnabosco R., Delijaicov S., 2013. Tool wear evaluations in friction stir processing of commercial titanium Ti-6Al-4V. *Wear* 302, 1327-1333.
- 51) Farnoush H., Sadeghi A., Abdi Bastami A., Moztarzadeh F., Aghazadeh Mohandesi J., 2013. An innovative fabrication of nano-HA coatings on Ti-CaP nanocomposite layer using a combination of friction stir processing and electrophoretic deposition. *Ceramics International* 39, 1477-1483.
- 52) Farshbaf Zinati R., Razfar M.R., Nazockdast H., 2014. Numerical and experimental investigation of FSP of PA 6/MWCNT composite. *Journal of Materials Processing Technology* 214, 2300-2315.
- 53) Feng A., Xiao B., Ma Z.Y., 2008. Effect of microstructural evolution on mechanical properties of friction stir welded AA2009/SiCp composite. *Composites Science and Technology* 68, 2141-2148.
- 54) Frigaard Ø., Grong Ø., and Midling O.T., 2001. A process model for friction stir welding of age hardening aluminum alloys. *Metallurgical and Materials Transactions A* 32A, 1189-1200.
- 55) Fu R.D., Zhang J.F., Li Y.J., Kang, J., Liu, H.J., Zhang, F.C., 2013. Effect of welding heat input and post-welding natural aging on hardness of stir zone for friction stir-welded 2024-T3 aluminum alloy thin-sheet. *Materials Science and Engineering: A* 559, 319-324.
- 56) Gan Y.X., Solomon D., Reinbolt M., 2010. Friction Stir Processing of Particle Reinforced Composite Materials. *Materials* 3, 329-350.

- 57) Gandra J., Krohn H., Miranda R.M., Vilaça P., Quintino L., dos Santos J.F., 2014. Friction surfacing-A review. *Journal of Materials Processing Technology* 214, 1062-1093.
- 58) Gandra J., Miranda R., Vilaça P., Velhinho A., Teixeira J.P., 2011. Functionally graded materials produced by friction stir processing. *Journal of Materials Processing Technology* 211, 1659-1668.
- 59) Gandra J., Vigarinho P., Pereira D., Miranda R.M., Velhinho A., Vilaça P., 2013. Wear characterization of functionally graded Al-SiC composite coatings produced by Friction Surfacing. *Material and Design* 52, 373-383.
- 60) Ghasemi-Kahrizsangi A., Kashani-Bozorg S.F., 2012. Microstructure and mechanical properties of steel/TiC nano-composite surface layer produced by friction stir processing. *Surface and Coatings Technology* 209, 15-22.
- 61) Giribaskar S., Gouthama, Prasad, R. and Ramkumar J., 2008. TEM studies on recovery and recrystallisation in equal channel angular extrusion processed Al-3%Mg alloy. *Transactions of Indian Institute of Metals* 61, 173-176.
- 62) Gourdet S., Montheillet F., 2003. A model of continuous dynamic recrystallization. *Acta Materialia* 51, 2685-2699.
- 63) Guerra M., Schmidt C., McClure J.C., Murr L.E., Nunes A.C., 2002. Flow patterns during friction stir welding. *Materials Characterization* 49, 95-101.
- 64) Guo J.F., Liu J., Sun C.N., Maleksaeedi S., Bi G., Tan M.J., Wei J., 2014. Effects of nano-Al<sub>2</sub>O<sub>3</sub> particle addition on grain structure evolution and mechanical behaviour of friction-stir-processed Al. *Materials Science and Engineering: A* 602, 143-149.
- 65) Gurunath P.V., Bijwe J., 2007. Friction and wear studies on brake-pad materials based on newly developed resin. *Wear* 263, 1212-1219.
- 66) Haseeb A.S.M.A., Islam M. A., Bepari M.M.A., 2000. Tribological behaviour of quenched and tempered, and austempered ductile iron at the same hardness level. *Wear* 244, 15-19.
- 67) Heidarzadeh A., Jabbari M., Esmaily M., 2014. Prediction of grain size and mechanical properties in friction stir welded pure copper joints using a thermal model. *The International Journal of Advanced Manufacturing Technology*.
- 68) Hirth J.P., 1976. Obstacle size in dispersion hardening by the Orowan process. *Scripta Metallurgica* 10, 755-757.

- 69) Hodder, K.J., Izadi, H., McDonald, A.G., Gerlich, A.P., 2012. Fabrication of aluminum–alumina metal matrix composites via cold gas dynamic spraying at low pressure followed by friction stir processing. *Materials Science and Engineering: A* 556, 114-121.
- 70) Hofmann D.C., Vecchio K.S., 2005. Submerged friction stir processing (SFSP): An improved method for creating ultra-fine-grained bulk materials. *Materials Science and Engineering: A* 402, 234-241.
- 71) Hosseinipour S.J., 2009. An investigation into hot deformation of aluminum alloy 5083. *Material and Design* 30(2), 319-322.
- 72) Hsu C.J., Chang C.Y., Kao P.W., Ho N.J., Chang C.P., 2006. Al-Al<sub>3</sub>Ti nanocomposites produced in situ by friction stir processing. *Acta Materialia* 54, 5241-5249.
- 73) Hsu C.J., Kao P.W., Ho N.J., 2005. Ultrafine-grained Al-Al<sub>2</sub>Cu composite produced in situ by friction stir processing. *Scripta Materialia* 53, 341-345.
- 74) Huang Y., Wang T., Guo W., Wan L., Lv S., 2014. Microstructure and surface mechanical property of AZ31 Mg/SiCp surface composite fabricated by Direct Friction Stir Processing. *Material and Design* 59, 274-278.
- 75) Izadi H., Gerlich A.P., 2012. Distribution and stability of carbon nanotubes during multi-pass friction stir processing of carbon nanotube/aluminum composites. *Carbon* 50, 4744-4749.
- 76) Izadi H., Nolting A., Munro C., Bishop D.P., Plucknett K.P., Gerlich A.P., 2013. Friction stir processing of Al/SiC composites fabricated by powder metallurgy. *Journal of Materials Processing Technology* 213, 1900-1907.
- 77) Jata K.V., Semiatin S.L., 2000. Continuous dynamic recrystallization during friction stir welding of high strength aluminum alloys. *Scripta Materialia* 43, 743-749.
- 78) Jerina J., Kalin M., 2014. Initiation and evolution of the aluminium-alloy transfer on hot-work tool steel at temperatures from 20°C to 500°C. *Wear* 319, 234-244.
- 79) Johannes L.B., Yowel L.L., Sosa E., Arepalli S., Mishra R.S., 2006. Survivability of single-walled carbon nanotubes during friction stir processing. *Nanotechnology* 17, 3081-3084.
- 80) Kakitsuji A., Ramkumar J., Kinose J., Mabuchi H., Tsuda H. and Morii K., 2002. Synthesis of TiAl(Cr)/Ti<sub>2</sub>AlC Composites by Reactive Arc-Melting. *Materials Transactions* 43, 2589-2592.
- 81) Kalin M., Kogovšek J., Kovač J., Remškar M., 2014. The Formation of Tribofilms of MoS<sub>2</sub> Nanotubes on Steel and DLC-Coated Surfaces. *Tribology Letters* 55, 381-391.

- 82) Kapoor R., Kumar N., Mishra R.S., Huskamp C.S., Sankaran K.K., 2010. Influence of fraction of high angle boundaries on the mechanical behavior of an ultrafine grained Al-Mg alloy. *Materials Science and Engineering: A* 527, 5246-5254.
- 83) Karthikeyan L., Senthilkumar V.S., Padmanabhan K.A., 2010. On the role of process variables in the friction stir processing of cast aluminum A319 alloy. *Material and Design* 31, 761-771.
- 84) Ke L., Huang C., Xing L., Huang K., 2010. Al-Ni intermetallic composites produced in situ by friction stir processing. *Journal of Alloys and Compounds* 503, 494-499.
- 85) Khandkar M.Z.H., Khan J.A., Reynolds A.P., 2003. Prediction of temperature distribution and thermal history during friction stir welding: input torque based model. *Science and Technology of Welding and Joining* 8, 165-174.
- 86) Khayyamin D., Mostafapour A., Keshmiri R., 2013. The effect of process parameters on microstructural characteristics of AZ91/SiO<sub>2</sub> composite fabricated by FSP. *Materials Science and Engineering: A* 559, 217-221.
- 87) Khodabakhshi F., Simchi A., Kokabi A.H., Gerlich A.P., Nosko M., 2014. Effects of post-annealing on the microstructure and mechanical properties of friction stir processed Al-Mg-TiO<sub>2</sub> nanocomposites. *Material and Design* 63, 30-41.
- 88) Khorrami M.S., Kazeminezhad M., Kokabi A.H., 2014. The effect of SiC nanoparticles on the friction stir processing of severely deformed aluminum. *Materials Science and Engineering: A* 602, 110-118.
- 89) Kim C.S., Sohn I., Nezafati M., Ferguson J.B., Schultz B.F., Bajestani-Gohari Z., Rohatgi P.K., Cho K., 2013. Prediction models for the yield strength of particle-reinforced unimodal pure magnesium (Mg) metal matrix nanocomposites (MMNCs). *Journal of Materials Science* 48, 4191-4204.
- 90) Kim H.J., Karthikeyan S., Rigney D., 2007. The structure and composition of aluminum wear debris generated by unlubricated sliding in different environments. *Wear* 263, 849-857.
- 91) Kim Y.G., Fujii H., Tsumura T., Komazaki T., Nakata K., 2006. Three defect types in friction stir welding of aluminum die casting alloy. *Materials Science and Engineering: A* 415, 250-254.
- 92) Krishnan K.N., 2002. On the formation of onion rings in friction stir welds. *Materials Science and Engineering A* 327, 246-251.
- 93) Kumar K., Kailas S.V., 2008. The role of friction stir welding tool on material flow and weld formation. *Materials Science and Engineering: A* 485, 367-374.

- 94) Kumar K., Kailas S.V., Srivatsan T.S., 2011. The Role of Tool Design in Influencing the Mechanism for the Formation of Friction Stir Welds in Aluminum Alloy 7020. *Materials and Manufacturing Processes* 26, 915-921.
- 95) Kumar S., Panwar R.S., Pandey O.P., 2012. Wear Behavior at High Temperature of Dual-Particle Size Zircon-Sand-Reinforced Aluminum Alloy Composite. *Metallurgical and Materials Transactions A* 44, 1548-1565.
- 96) Kumar S., Panwar R.S., Pandey O.P., 2013. Effect of dual reinforced ceramic particles on high temperature tribological properties of aluminum composites. *Ceramics International* 39, 6333-6342.
- 97) Kurt, A., Uygur, I., Cete, E., 2011. Surface modification of aluminium by friction stir processing. *Journal of Materials Processing Technology* 211, 313-317.
- 98) Kwon Y.J., Saito N., Shigematsu I., 2002. Friction stir process as a new manufacturing technique of ultrafine grained aluminum alloy. *Journal of material science letters* 21, 1473-1476.
- 99) Lados D.A., Apelian D., 2004. Fatigue crack growth characteristics in cast Al-Si-Mg alloys. *Materials Science and Engineering: A* 385, 200-211.
- 100) Lakshminarayanan A.K., Ramachandran C.S., Balasubramanian V., 2014. Feasibility of surface-coated friction stir welding tools to join AISI 304 grade austenitic stainless steel. *Defence Technology*.
- 101) Lee C., Huang J., Hsieh P., 2006. Mg based nano-composites fabricated by friction stir processing. *Scripta Materialia* 54, 1415-1420.
- 102) Lee I.S., Hsu C.J., Chen C.F., Ho N.J., Kao P.W., 2011. Particle-reinforced aluminum matrix composites produced from powder mixtures via friction stir processing. *Composites Science and Technology* 71, 693-698.
- 103) Lee I.S., Kao P.W., Chang C.P., Ho N.J., 2013. Formation of Al-Mo intermetallic particle-strengthened aluminum alloys by friction stir processing. *Intermetallics* 35, 9-14.
- 104) Lee I.S., Kao P.W., Ho N.J., 2008. Microstructure and mechanical properties of Al-Fe in situ nanocomposite produced by friction stir processing. *Intermetallics* 16, 1104-1108.
- 105) Li B., Shen Y., Luo L., Hu W., 2013. Fabrication of TiCp/Ti-6Al-4V surface composite via friction stir processing (FSP): Process optimization, particle dispersion-refinement behavior and hardening mechanism. *Materials Science and Engineering: A* 574, 75-85.
- 106) Li X.Y., Tandon K.N., 2000. Microstructural characterization of mechanically mixed layer and wear debris in sliding wear of an Al alloy and an Al based composite. *Wear* 245, 148-161.

- 107) Li, Y., Murr L.E., McClure, J.C., 1999. Solid-state flow visualization in the friction stir welding of 2024 Al to 6061 Al. *Scripta Materialia* 40, 1041-1046.
- 108) Lim D.K., Shibayanagi T., Gerlich A.P., 2009. Synthesis of multi-walled CNT reinforced aluminium alloy composite via friction stir processing. *Materials Science and Engineering: A* 507, 194-199.
- 109) Liu H.J., Feng J.C., Fujii H., Nogi K., 2005. Wear characteristics of a WC–Co tool in friction stir welding of AC4A+30vol%SiCp composite. *International Journal of Machine Tools and Manufacture* 45, 1635-1639.
- 110) Liu Q., Ke L., Liu F., Huang C., Xing L., 2013. Microstructure and mechanical property of multi-walled carbon nanotubes reinforced aluminum matrix composites fabricated by friction stir processing. *Material and Design* 45, 343-348.
- 111) Liu Z.Y., Xiao B.L., Wang W.G., Ma Z.Y., 2012. Singly dispersed carbon nanotube/aluminum composites fabricated by powder metallurgy combined with friction stir processing. *Carbon* 50, 1843-1852.
- 112) Liu Z.Y., Xiao B.L., Wang W.G., Ma Z.Y., 2013. Developing high-performance aluminum matrix composites with directionally aligned carbon nanotubes by combining friction stir processing and subsequent rolling. *Carbon* 62, 35-42.
- 113) Liu Z.Y., Xiao B.L., Wang W.G., Ma Z.Y., 2014a. Analysis of carbon nanotube shortening and composite strengthening in carbon nanotube/aluminum composites fabricated by multi-pass friction stir processing. *Carbon* 69, 264-274.
- 114) Liu Z.Y., Xiao B.L., Wang W.G., Ma Z.Y., 2014b. Tensile Strength and Electrical Conductivity of Carbon Nanotube Reinforced Aluminum Matrix Composites Fabricated by Powder Metallurgy Combined with Friction Stir Processing. *Journal of Materials Science & Technology* 30, 649-655.
- 115) Lloyd D.J., 1994. Particle reinforced aluminium and magnesium matrix composites. *International Materials Reviews* 39, 1-23.
- 116) London B., Fin J., Pelton A., Fuller C., Mahoney M., 2005. Friction stir processing of Nitinol, In: Jata, K.V., Mahoney, M.W., Mishra, R.S., and Lienert, T.J. (Ed.), *Friction Stir Welding and Processing III*. TMS, Warrendale, PA, pp. 67-74.
- 117) Lorrain O., Favier V., Zahrouni H., Lawrjaniec D., 2010. Understanding the material flow path of friction stir welding process using unthreaded tools. *Journal of Materials Processing Technology* 210, 603-609.
- 118) Lu D., Jiang Y., Zhou R., 2013. Wear performance of nano- $\text{Al}_2\text{O}_3$  particles and CNTs reinforced magnesium matrix composites by friction stir processing. *Wear* 305, 286-290.

- 119) Ma W., Lu J., Wang B., 2009. Sliding friction and wear of Cu-graphite against 2024, AZ91D and Ti6Al4V at different speeds. *Wear* 266, 1072-1081.
- 120) Ma Z.Y., 2008. Friction Stir Processing Technology: A Review. *Metallurgical and Materials Transactions A* 39, 642-658.
- 121) Ma Z.Y., Sharma S.R., Mishra R.S., 2006. Effect of friction stir processing on the microstructure of cast A356 aluminum. *Materials Science and Engineering: A* 433, 269-278.
- 122) Mahmoud E.R.I., Takahashi M., Shibayanagi T., Ikeuchi K., 2009a. Effect of friction stir processing tool probe on fabrication of SiC particle reinforced composite on aluminium surface. *Science and Technology of Welding and Joining* 14, 413-425.
- 123) Mahmoud E.R.I., Takahashi M., Shibayanagi T., Ikeuchi K., 2009b. Fabrication of Surface-Hybrid-MMCs Layer on Aluminum Plate by Friction Stir Processing and Its Wear Characteristics. *Materials Transactions* 50, 1824-1831.
- 124) Mahoney M. W., Flintoff J. G., Bingel W. H. and Spurling R. A., 1998. Properties of Friction-Stir-Welded 7075 T651 Aluminum. *Metallurgical and Materials Transactions A* 29, 1955-1964.
- 125) Manigandan K., Srivatsan T.S., Quick T., 2012. Influence of silicon carbide particulates on tensile fracture behavior of an aluminum alloy. *Materials Science and Engineering: A* 534, 711-715.
- 126) Mazaheri Y., Karimzadeh F., Enayati M.H., 2011. A novel technique for development of A356/Al<sub>2</sub>O<sub>3</sub> surface nanocomposite by friction stir processing. *Journal of Materials Processing Technology* 211, 1614-1619.
- 127) McNelley T.R., Swaminathan S., Su J.Q., 2008. Recrystallization mechanisms during friction stir welding/processing of aluminum alloys. *Scripta Materialia* 58, 349-354.
- 128) Meng C., Cui H.C., Lu F.G. and Tang X.H., 2013. Evolution behavior of TiB<sub>2</sub> particles during laser welding on aluminum metal matrix composites reinforced with particles. *Transactions of Nonferrous Metals Society of China* 23, 1543-1548.
- 129) Miller W.S., Humphreys, F.J., 1991. Strengthening mechanisms in particulate metal matrix composites. *Scripta Metallurgica et Materialia* 25, 33-38.
- 130) Miranda, R.M., Santos, T.G., Gandra, J., Lopes, N., Silva, R.J.C., 2013. Reinforcement strategies for producing functionally graded materials by friction stir processing in aluminium alloys. *Journal of Materials Processing Technology* 213, 1609-1615.
- 131) Mironov S., Sato Y.S., Kokawa H., 2008. Microstructural evolution during friction stir-processing of pure iron. *Acta Materialia* 56, 2602-2614.



- 132) Mishra R.S., Ma Z.Y., 2005. Friction stir welding and processing. *Materials Science and Engineering: R: Reports* 50, 1-78.
- 133) Mishra R.S., Ma, Z.Y., Charit I., 2003. Friction stir processing: a novel technique for fabrication of surface composite. *Materials Science and Engineering A* 341, 307-310.
- 134) Mishra R.S., Mahoney M.W., McFadden S.X., Mara N.A., Mukherjee A.K., 1999. High strain rate superplasticity in a friction stir processed 7075 Al alloy. *Scripta Materialia* 42, 163-168.
- 135) Miyazawa T., Iwamoto Y., Maruko T., Fujii H., 2011. Development of Ir based tool for friction stir welding of high temperature materials. *Science and Technology of Welding and Joining* 16, 188-192.
- 136) Moghaddas M.A., Kashani-Bozorg S.F., 2013. Effects of thermal conditions on microstructure in nanocomposite of Al/Si<sub>3</sub>N<sub>4</sub> produced by friction stir processing. *Materials Science and Engineering: A* 559, 187-193.
- 137) Morisada Y., Fujii H., Mizuno T., Abe G., Nagaoka T., Fukusumi M., 2010. Modification of thermally sprayed cemented carbide layer by friction stir processing. *Surface and Coatings Technology* 204, 2459-2464.
- 138) Morisada Y., Fujii H., Nagaoka T., Fukusumi M., 2006a. MWCNTs/AZ31 surface composites fabricated by friction stir processing. *Materials Science and Engineering: A* 419, 344-348.
- 139) Morisada Y., Fujii H., Nagaoka T., Fukusumi M., 2006b. Effect of friction stir processing with SiC particles on microstructure and hardness of AZ31. *Materials Science and Engineering: A* 433, 50-54.
- 140) Morisada Y., Fujii H., Nagaoka T., Fukusumi M., 2006c. Nanocrystallized magnesium alloy – uniform dispersion of C<sub>60</sub> molecules. *Scripta Materialia* 55, 1067-1070.
- 141) Mostafapour Asl A., Khandani S.T., 2013. Role of hybrid ratio in microstructural, mechanical and sliding wear properties of the Al5083/Graphitep/Al<sub>2</sub>O<sub>3</sub>p a surface hybrid nanocomposite fabricated via friction stir processing method. *Materials Science and Engineering: A* 559, 549-557.
- 142) Najafi M., Nasiri A.M., Kokabi A.H., 2008. Microstructure and hardness of friction stir processed AZ31 with SiCP. *International Journal of Modern Physics B* 22, 2879-2885.
- 143) Nandan R., Debroy T., Bhadeshia H., 2008. Recent advances in friction-stir welding – Process, weldment structure and properties. *Progress in Materials Science* 53, 980-1023.
- 144) Nardone V.C., 1987. Assessment of models used to predict the strength of discontinuous silicon carbide reinforced aluminum alloys. *Scripta Metallurgica* 21, 1313-1318.

- 145) Nardone V.C., Prewo K.M., 1986. On the strength of discontinuous silicon carbide reinforced aluminum composites. *Scripta Metallurgica* 20, 43-438.
- 146) Nguyen Q., Gupta M., 2008. Enhancing compressive response of AZ31B magnesium alloy using alumina nanoparticulates. *Composites Science and Technology* 68, 2185-2192.
- 147) Ni D.R., Wang J.J., Zhou Z.N., Ma Z.Y., 2014. Fabrication and mechanical properties of bulk NiTiP/Al composites prepared by friction stir processing. *Journal of Alloys and Compounds* 586, 368-374.
- 148) Nieh T.G., Wadsworth J., 1991. Hall-petch relation in nanocrystalline solids. *Scripta Metallurgica et Materiala* 25, 955-958.
- 149) Padmanaban G., Balasubramanian V., 2009. Selection of FSW tool pin profile, shoulder diameter and material for joining AZ31B magnesium alloy – An experimental approach. *Material and Design* 30, 2647-2656.
- 150) Palanivel R., Koshy Mathews P., Murugan N., Dinaharan I., 2012. Effect of tool rotational speed and pin profile on microstructure and tensile strength of dissimilar friction stir welded AA5083-H111 and AA6351-T6 aluminum alloys. *Material and Design* 40, 7-16.
- 151) Pantelis D., Tissandier A., Manolatos P., Ponthiaux P., 1995. Formation of wear resistant Al-SiC surface composite by laser melt-particle injection process. *Materials Science and Technology* 11, 299-303.
- 152) Podgornik B., Vizintin J., Thorbjornsson I., Johannesson B., Thorgrimsson J.T., Martinez Celis M., Valle N., 2012. Improvement of ductile iron wear resistance through local surface reinforcement. *Wear* 274-275, 267-273.
- 153) Pogačnik A., Kalin M., 2013. How to determine the number of asperity peaks, their radii and their heights for engineering surfaces: A critical appraisal. *Wear* 300, 143-154.
- 154) Popov V., 2004. Carbon nanotubes: properties and application. *Materials Science and Engineering: R: Reports* 43, 61-102.
- 155) Prado R.A., Murr L.E., Soto K.F., McClure J.C., 2003. Self-optimization in tool wear for friction-stir welding of Al 6061+20% Al<sub>2</sub>O<sub>3</sub> MMC. *Materials Science and Engineering: A* 349, 156-165.
- 156) Prangnell P.B., Heason C.P., 2005. Grain structure formation during friction stir welding observed by the 'stop action technique'. *Acta Materialia* 53, 3179-3192.

- 157) Qian J., Li J., Xiong J., Zhang F., Lin X., 2012. In situ synthesizing Al<sub>3</sub>Ni for fabrication of intermetallic-reinforced aluminum alloy composites by friction stir processing. *Materials Science and Engineering: A* 550, 279-285.
- 158) Rai R., De A., Bhadeshia H.K.D.H., DebRoy T., 2011. Review: friction stir welding tools. *Science and Technology of Welding and Joining* 16, 325-342.
- 159) Rajesh J.J., Bijwe J., Tewari U.S., 2002. Abrasive wear performance of various polyamides. *Wear* 252, 769-776.
- 160) Ramakrishnan N., 1996. An analytical particulate study on strengthening of reinforced metal matrix composites. *Acta Materialia* 44, 69-77.
- 161) Ramkumar J., Malhotra S. K., Krishnamurthy R., Mabuchi H., Demizu K., Kakitsuji A., Tsuda H., Matsui T., Morii K., 2003. Microstructure and Dry Sliding Wear of Ti-50Al Alloy and Ti-47Al-3W/Ti<sub>2</sub>AlC Composite Produced by Reactive Arc-Melting. *Materials Transactions* 44, 1861-1865.
- 162) Rao A.G., Rao B.R.K., Deshmukh V.P., Shah A.K., Kashyap B.P., 2009. Microstructural refinement of a cast hypereutectic Al-30Si alloy by friction stir processing. *Materials Letters* 63, 2628-2630.
- 163) Ratna Sunil B., Sampath Kumar T.S., Chakkingal U., Nandakumar V., Doble M., 2014. Nano-hydroxyapatite reinforced AZ31 magnesium alloy by friction stir processing: a solid state processing for biodegradable metal matrix composites. *Journal of materials science. Materials in medicine* 25, 975-988.
- 164) Reddy P.J., Kailas S.V., Srivatsan T.S., 2011. Effect of Tool Angle on Friction Stir Welding of Aluminum Alloy 5052: Role of Sheet Thickness. *Advanced Materials Research* 410, 196-205.
- 165) Rejil C.M., Dinaharan I., Vijay S.J., Murugan N., 2012. Microstructure and sliding wear behavior of AA6360/(TiC+B<sub>4</sub>C) hybrid surface composite layer synthesized by friction stir processing on aluminum substrate. *Materials Science and Engineering: A* 552, 336-344.
- 166) Rhodes C., 2003. Fine-grain evolution in friction-stir processed 7050 aluminum. *Scripta Materialia* 48, 1451-1455.
- 167) Rigney D.A., Chen L. H., Naylor M. G. S., 1984. Wear processes in sliding systems. *Wear* 100, 195-219.
- 168) Robson J.D., Campbell L., 2010. Model for grain evolution during friction stir welding of aluminium alloys. *Science and Technology of Welding and Joining* 15, 171-176.

- 169) Rohatgi P.K., Ray S., Liu Y., 1992. Tribological properties of metal matrix-graphite particle composites. *International Materials Reviews* 37(3), 129-152.
- 170) Rohrer G.S., 2010. "Introduction to Grains, Phases, and Interfaces—an Interpretation of Microstructure," *Trans. AIME*, 1948, vol. 175, pp. 15–51, by C.S. Smith. *Metallurgical and Materials Transactions A* 41, 1063-1100.
- 171) Rosales M.J.C., Alcantara N.G., Santos J., Zettler R., 2010. The Backing Bar Role in Heat Transfer on Aluminium Alloys Friction Stir Welding. *Materials Science Forum* 636-637, 459-464.
- 172) Rosenberger M.R., Schvezov C.E., Forlerer E., 2005. Wear of different aluminum matrix composites under conditions that generate a mechanically mixed layer. *Wear* 259, 590-601.
- 173) Roy D., Basu B., Basu Mallick A., 2005. Tribological properties of Ti-aluminide reinforced Al-based in situ metal matrix composite. *Intermetallics* 13, 733-740.
- 174) Roy D., Ghosh S., Basumallick A., Basu B., 2007. Preparation of Ti-aluminide reinforced in situ aluminium matrix composites by reactive hot pressing. *Journal of Alloys and Compounds* 436, 107-111.
- 175) Sabirov I., Murashkin M.Y., Valiev R.Z., 2013. Nanostructured aluminium alloys produced by severe plastic deformation: New horizons in development. *Materials Science and Engineering: A* 560, 1-24.
- 176) Saeid T., Abdollah-zadeh A., Assadi H., Malek Ghaini F., 2008. Effect of friction stir welding speed on the microstructure and mechanical properties of a duplex stainless steel. *Materials Science and Engineering: A* 496, 262-268.
- 177) Saito Y., Utsunomiya H., Tsuji N., Sakai T., 1999. Novel ultra-high straining process for bulk materials development of the accumulative roll-bonding (ARB) process. *Acta Materialia* 47, 579-583.
- 178) Sakai G., Horita Z., Langdon T.G., 2005. Grain refinement and superplasticity in an aluminum alloy processed by high-pressure torsion. *Materials Science and Engineering: A* 393, 344-351.
- 179) Sakai T., Belyakov A., Miura H., 2008. Ultrafine Grain Formation in Ferritic Stainless Steel during Severe Plastic Deformation. *Metallurgical and Materials Transactions A* 39, 2206-2214.
- 180) Salehi M., Farnoush H., Mohandesi J.A., 2014. Fabrication and characterization of functionally graded Al–SiC nanocomposite by using a novel multistep friction stir processing. *Material and Design* 63, 419-426.

- 181) Salehi M., Saadatmand M., Aghazadeh Mohandesi J., 2012. Optimization of process parameters for producing AA6061/SiC nanocomposites by friction stir processing. *Transactions of Nonferrous Metals Society of China* 22, 1055-1063.
- 182) Sanaty-Zadeh A., Rohatgi P.K., 2012. Comparison between current models for the strength of particulate-reinforced metal matrix nanocomposites with emphasis on consideration of Hall-Petch effect. *Materials Science and Engineering: A* 531, 112-118.
- 183) Sankar M.R., Ramkumar J., Jain V.K., 2009. Experimental investigation and mechanism of material removal in nano finishing of MMCs using abrasive flow finishing (AFF) process. *Wear* 266, 688-698.
- 184) Sathiskumar R., Murugan N., Dinaharan I., Vijay S.J., 2013. Characterization of boron carbide particulate reinforced in situ copper surface composites synthesized using friction stir processing. *Materials Characterization* 84, 16-27.
- 185) Sato Y., Miyake M., Kokawa H., Omori T., Ishida K., Imano S., Park S. , Hirano S. , 2011. Development of a cobalt-based alloy FSW tool for high-softening-temperature materials, In: Mishra R.S., Mahoney M.W., Sato Y., Hovanski Y., Verma R. (Ed.), *Friction Stir Welding and Processing VI*. TMS, San Diego, California, USA, pp. 3-9.
- 186) Sato Y.S., Kokawa H., Masatoshi E., Jogan S., 1999. Microstructural Evolution of 6063 Aluminum during Friction-Stir Welding. *Metallurgical and Materials Transactions A* 30, 2429-2437.
- 187) Shafiei-Zarghani A., Kashani-Bozorg S.F., Zarei-Hanzaki A., 2009. Microstructures and mechanical properties of Al/Al<sub>2</sub>O<sub>3</sub> surface nano-composite layer produced by friction stir processing. *Materials Science and Engineering: A* 500, 84-91.
- 188) Shahraki S., Khorasani S., Abdi Behnagh R., Fotouhi Y., Bisadi H., 2013. Producing of AA5083/ZrO<sub>2</sub> Nanocomposite by Friction Stir Processing (FSP). *Metallurgical and Materials Transactions B* 44, 1546-1553.
- 189) Shamsipur A., Kashani-Bozorg S.F., Zarei-Hanzaki A., 2011. The effects of friction-stir process parameters on the fabrication of Ti/SiC nano-composite surface layer. *Surface and Coatings Technology* 206, 1372-1381.
- 190) Sharifitabar M., Sarani A., Khorshahian S., Shafiee Afarani M., 2011. Fabrication of 5052Al/Al<sub>2</sub>O<sub>3</sub> nanoceramic particle reinforced composite via friction stir processing route. *Material and Design* 32, 4164-4172.
- 191) Sharma S., 2004. Effect of friction stir processing on fatigue behavior of A356 alloy. *Scripta Materialia* 51, 237-241.

- 192) Sharma V., Prakash U., Kumar B.V.M., 2015. Surface composites by friction stir processing: A review. *Journal of Materials Processing Technology* 224, 117-134.
- 193) Singh R., Fitz-Gerald J., 1997. Surface composites: A new class of engineered materials. *Journal of Materials Research* 12, 769-773.
- 194) Soleymani S., Abdollah-zadeh A., Alidokht S.A., 2012. Microstructural and tribological properties of Al5083 based surface hybrid composite produced by friction stir processing. *Wear* 278-279, 41-47.
- 195) Su, J.Q., Nelson T.W., Sterling C.J., 2005. Friction stir processing of large-area bulk UFG aluminum alloys. *Scripta Materialia* 52, 135-140.
- 196) Suh N.P., 1973. The delamination theory of wear. *Wear* 25, 111-124.
- 197) Sun N., and Apelian D., 2011. Friction stir processing of aluminum cast alloys for high performance applications. *JOM* 63, 44-50.
- 198) Sun N., Apelian D., 2009. Microstructural Modification of A206 Aluminium via Friction Stir Processing. *Materials Science Forum* 618-619, 361-364.
- 199) Sundararajan G., Venkataraman B., 1996. The sliding wear behaviour of Al-SiC particulate composites-I. Macrobehaviour. *Acta Materialia* 44, 451-460.
- 200) Suresha S., Sridhara B.K., 2010. Wear characteristics of hybrid aluminium matrix composites reinforced with graphite and silicon carbide particulates. *Composites Science and Technology* 70, 1652-1659.
- 201) Swaminathan S., Oh-Ishi K., Zhilyaev A.P., Fuller C.B., London B., Mahoney M.W., McNelley T.R., 2009. Peak Stir Zone Temperatures during Friction Stir Processing. *Metallurgical and Materials Transactions A* 41, 631-640.
- 202) Tang F., Wu X., Ge S., Ye J., Zhu H., Hagiwara M., Schoenung J.M., 2008. Dry sliding friction and wear properties of B4C particulate-reinforced Al-5083 matrix composites. *Wear* 264 (7-8), 555-561.
- 203) Thompson B., Babu S. S., 2010. Tool degradation characterization in the friction stir welding of hard metals. *Welding Journal* 89, 256-261.
- 204) Tiwari S.N., Pathak J.P., Malhotra S.L., 1985. Aluminium Alloys as Plain Bearing Materials - An Overview. *Key Engineering Materials* 8, 139-158.
- 205) Tjong S.C., 2007. Novel Nanoparticle-Reinforced Metal Matrix Composites with Enhanced Mechanical Properties. *Advanced Engineering Materials* 9, 639-652.
- 206) Tjong S.C., Ma Z.Y., 2000. Microstructural and mechanical characteristics of in situ metal matrix composites. *Materials Science and Engineering: R: Reports* 29, 49-113.

- 207) Tongne A., Jahazi M., Feulvarch E., Desrayaud C., 2015. Banded structures in friction stir welded Al alloys. *Journal of Materials Processing Technology* 221, 269-278.
- 208) Tsai F.Y., Kao P.W., 2012. Improvement of mechanical properties of a cast Al–Si base alloy by friction stir processing. *Materials Letters* 80, 40-42.
- 209) Tutunchilar S., Besharati Givi M.K., Haghpanahi M., Asadi P., 2012. Eutectic Al–Si piston alloy surface transformed to modified hypereutectic alloy via FSP. *Materials Science and Engineering: A* 534, 557-567.
- 210) Upadhyay P., Reynolds A.P., 2012. Effects of forge axis force and backing plate thermal diffusivity on FSW of AA6056. *Materials Science and Engineering: A* 558, 394-402.
- 211) Valiev R.Z., Islamgaliev R.K.I. Alexandrov V., 2000. Bulk nanostructured materials from severe plastic deformation. *Progress in Materials Science* 45, 103-189.
- 212) Valiev R.Z., Korznikov A. V., Mulyukov R. R., 1993. Structure and properties of ultrafine-grained materials produced by severe plastic deformation. *Materials Science and Engineering: A* 168, 141-148.
- 213) Valiev R.Z., Langdon T.G., 2006. Principles of equal-channel angular pressing as a processing tool for grain refinement. *Progress in Materials Science* 51, 881-981.
- 214) Venkataraman B. Sundararajan, G., 1996. The sliding wear behaviour of Al-SiC particulate composites-II. The characterization of subsurface deformation and correlation with wear behaviour. *Acta Materialia* 44, 461-473.
- 215) Venkataraman, B., Sundararajan, G., 2000. Correlation between the characteristics of the mechanically mixed layer and wear behaviour of aluminium, Al-7075 alloy and Al-MMCs. *Wear* 245, 22-38.
- 216) Vijayavel P., Balasubramanian V., Sundaram S., 2014. Effect of shoulder diameter to pin diameter (D/d) ratio on tensile strength and ductility of friction stir processed LM25AA-5% SiCp metal matrix composites. *Material and Design* 57, 1-9.
- 217) Woo W., Choo H., Brown D.W., Feng Z., 2007. Influence of the Tool Pin and Shoulder on Microstructure and Natural Aging Kinetics in a Friction-Stir-Processed 6061–T6 Aluminum Alloy. *Metallurgical and Materials Transactions A* 38, 69-76.
- 218) Wu X.F., Zhang G.A., 2011. Effect of Sn addition on microstructure and dry sliding wear behaviors of hypereutectic aluminum–silicon alloy A390. *Journal of Materials Science* 46, 7319-7327.
- 219) Xu N., Ueji R., Fujii H., 2014. Enhanced mechanical properties of 70/30 brass joint by rapid cooling friction stir welding. *Materials Science and Engineering: A* 610, 132-138.

- 220) Xue P., Xiao B.L., Ma Z.Y., 2014. Achieving ultrafine-grained structure in a pure nickel by friction stir processing with additional cooling. *Material and Design* 56, 848-851.
- 221) You G.L., Ho N.J., Kao P.W., 2013a. In-situ formation of Al<sub>2</sub>O<sub>3</sub> nanoparticles during friction stir processing of AlSiO<sub>2</sub> composite. *Materials Characterization* 80, 1-8.
- 222) You G.L., Ho N.J., Kao P.W., 2013b. The microstructure and mechanical properties of an Al–CuO in-situ composite produced using friction stir processing. *Materials Letters* 90, 26-29.
- 223) Yu Z., Zhang W., Choo H., Feng Z., 2011. Transient Heat and Material Flow Modeling of Friction Stir Processing of Magnesium Alloy using Threaded Tool. *Metallurgical and Materials Transactions A* 43, 724-737.
- 224) Zahmatkesh B., Enayati M.H., 2010. A novel approach for development of surface nanocomposite by friction stir processing. *Materials Science and Engineering: A* 527, 6734-6740.
- 225) Zhang Q., Xiao B.L., Ma Z.Y., 2013. In situ formation of various intermetallic particles in Al–Ti–X(Cu, Mg) systems during friction stir processing. *Intermetallics* 40, 36-44.
- 226) Zhang Q., Xiao B.L., Wang Q.Z., Ma Z.Y., 2011. In situ Al<sub>3</sub>Ti and Al<sub>2</sub>O<sub>3</sub> nanoparticles reinforced Al composites produced by friction stir processing in an Al–TiO<sub>2</sub> system. *Materials Letters* 65, 2070-2072.
- 227) Zhang Q., Xiao B.L., Wang Q.Z., Ma Z.Y., 2014. Effects of Processing Parameters on the Microstructures and Mechanical Properties of In Situ (Al<sub>3</sub>Ti + Al<sub>2</sub>O<sub>3</sub>)/Al Composites Fabricated by Hot Pressing and Subsequent Friction-Stir Processing. *Metallurgical and Materials Transactions A* 45, 2776-2791.
- 228) Zhang Q., Xiao B.L., Wang W.G., Ma Z.Y., 2012. Reactive mechanism and mechanical properties of in situ composites fabricated from an Al–TiO<sub>2</sub> system by friction stir processing. *Acta Materialia* 60, 7090-7103.
- 229) Zhang Y.N., Cao X., Larose S., Wanjara P., 2012. Review of tools for friction stir welding and processing. *Canadian Metallurgical Quarterly* 51, 250-261.
- 230) Zhang Z., Chen D., 2006. Consideration of Orowan strengthening effect in particulate-reinforced metal matrix nanocomposites: A model for predicting their yield strength. *Scripta Materialia* 54, 1321-1326.
- 231) Zohoor M., Besharati Givi M.K., Salami P., 2012. Effect of processing parameters on fabrication of Al–Mg/Cu composites via friction stir processing. *Material and Design* 39, 358-365.